Computational Modelling of Knee Tissue Mechanics During Single-Leg Jump Landing

by

Harish Raghavendra Rao

A thesis
presented to the University of Waterloo
in fulfillment of the
thesis requirement for the degree of
Master of Applied Science
in
Mechanical and Mechatronics Engineering

Waterloo, Ontario, Canada, 2020

Author's Declaration

I hereby declare that I am the sole author of this thesis. This is a true copy of the thesis, including any required final revisions, as accepted by my examiners.

I understand that my thesis may be made electronically available to the public.

Abstract

The anterior cruciate ligament (ACL) plays a crucial role in stabilising the knee joint in anterior tibial translation and internal tibial rotation. Non-contact ACL injuries are a major concern in sport-related activities due to sudden dynamic manoeuvres involved. Concomitant injuries to other tissues of the knee joint such as meniscal tears are common with ACL injuries. Treatment of ACL injuries through surgical reconstructions and rehabilitation imposes a large socioeconomic burden on healthcare systems. Researchers have extensively used a combination of *in-vitro* experiments on cadaveric specimens and computational modelling to explore the biomechanical factors surrounding ACL injury in dynamic knee movements.

The primary objective of this study was to develop a subject-specific knee finite element (FE) model to simulate an injury-causing motion - single-leg jump landing and validate ACL strain based on previous *in-vitro* experiments. Medical images of a cadaver specimen were segmented to generate three-dimensional (3D) models of the anatomic structures of the knee joint. High-quality meshes of the segmented 3D models were produced. Digitization technique was used to replicate the knee ligament insertion sites of the cadaver specimen in the model accurately. The kinematic response of the model under basic knee motions was validated with published experimental data. Muscle forces and kinematic inputs from a previous study involving the motion capture of ten participants were used as the boundary conditions to simulate a jump landing motion. Explicit FE analyses were performed on the model under half, and full muscle force conditions and the ACL and meniscal strain outputs were compared with experimental results.

Results showed that the ACL strain trends in the half muscle force jump simulations of two participant profiles (P5, P6) agreed well with the *in-vitro* experimental results from the cadaver knee. However, the computational peak ACL strain values of the two profiles (5.5 % at 228 ms and 4.9 % at 177 ms) did not agree well with the experimental results (2.8 % at 151 ms and 3.5 % at 164 ms). The ACL strain trends during the full muscle force jump simulations of ten participant profiles (P1 – P10) showed better agreement with the experimental results from different cadaver knees of a previous study. In addition, in the half muscle force jump simulations of two participant profiles (P5, P6), the peak values of posterior medial meniscal strain from the FE model (0.7 % and 1.4 %) agreed well with the experimental results (0.75 % and 1.3 %) from different cadaver knees.

This study demonstrated a methodology to develop a subject-specific FE model of the knee joint that could be used to recreate *in-vitro* dynamic experimental conditions to make predictions of ACL and medial meniscal strains, providing an effective approach to overcome the limitations of experimental testing. Future work will use the established model to predict the risk of injury and design injury prevention strategies in dynamic knee loading scenarios.

Acknowledgements

I thank my supervisors, Dr Naveen Chandrashekar and Dr Stewart McLachlin, for providing me with an opportunity to pursue my master's and for their constant motivation, encouragement and support throughout this exciting journey. Thanks to Dr Cari Whyne (Sunnybrook Research Institute) for her guidance in the early stages of this project. Thanks to Xiuling Qi for performing the MRI procedure. Thanks to Dr Bojra Rodriguez-Vila (European University of Madrid) and Dr David Pierce (University of Connecticut) for helping me with the meshing process. My sincere thanks to Hashim Hassan (PhD candidate, Purdue University) for helping me fix some important issues with the simulations.

Thanks to Mayank Kalra for going out of his way to help me whenever I have asked him. Thanks to Robert Bahensky for his help with the segmentation procedure and sparking my interest in LaTeX. Thanks to Shamanth Hampali for listening to all of my bad (sometimes good) ideas, frustrations and bickering, you have been a great friend! Thanks to Daniel Loewen for being that ideal student for me to look up to, for the interesting discussions, for motivating me to write and importantly for being an amazing friend. Thanks to Jin Zhu for always motivating me. Thanks to Prasannaah Hadagali for his guidance and for the well-timed publication of his study, which helped progress my research. Thanks to Piyius Raj and Matheus Correia for spending their valuable time to help me with my research. Thanks to Anna Polak and Kaab Omer for being such wonderful friends and making me appreciate the world outside of research.

I thank my family, Raghavendra Rao, Usha Rao and Harini for their encouragement to take on this adventure. My dearest friend, Abhishek Krishnan, I thank you for persuading me to enroll in a masters degree and being a pillar of support throughout. Most importantly, I express my gratitude to my wife, Sachitha Rao. I can never imagine stepping outside the comforts of my home in India and going on this exciting journey without you.

Thanks to the special one, the news of her arrival has made my life more enjoyable!

Table of Contents

List of Figures viii

List of Tables xi

1 Introduction 1

1.1 Motivation . . . 1
1.2 Objective . . . 2
1.3 Thesis Overview . . . 2

2 Background 4

2.1 Anatomical Background . . . 4
2.1.1 Nomenclature . . . 4
2.1.2 Knee Anatomy . . . 5
2.1.3 ACL Anatomy and Function . . . 9
2.2 ACL Injury . . . 10
2.3 Experimental Research . . . 13
2.4 Computational Research . . . 17
2.4.1 Subject-Specific Models . . . 17
2.4.2 Computational Models of Jump Landing . . . 22
2.4.3 Modelling Ligament Behaviour . . . 23
2.5 Summary of Previous Research . . . 26
2.6 Hypothesis . . . 28

3 Methodology **29**

3.1 Development of Subject-Specific Finite Element Model 29

3.1.1 Definition of Tissue Geometries Using Medical Imaging 29

3.1.2 Digitization of Ligament Insertion Sites 34

3.1.3 Tibial Slope 36

3.1.4 Meshing of the Segmented Geometries 36

3.1.5 Model Definition in Abaqus CAE 40

3.2 Finite Element Analysis 49

3.2.1 Verification of Kinematics 50

3.2.2 Boundary Conditions for Single-Leg Jump Landing 52

3.2.3 Single-Leg Jump Landing Simulations 56

4 Results **61**

4.1 Mesh Output and Quality 61

4.1.1 Hexahedral Element Quality 62

4.2 Kinematic Verification Studies 62

4.3 Single-Leg Jump Landing Simulations 65

4.3.1 Moment Arms 65

4.3.2 Verification of Model Inputs 66

4.3.3 Half Muscle Force Jump 67

4.3.4 Full Muscle Force Jump 69

4.3.5 Energy Balance 74

5 Discussion **75**

5.1 Finite Element Model Development 75

5.2 Kinematic Verification Studies 77

5.3 Single-Leg Jump Landing 78

5.3.1 Half Muscle Force Jump 78

5.3.2 Full Muscle Force Jump 81

6 Conclusions **86**

6.1 Summary 86

6.2 Limitations 87

6.3 Future Directions 88

References **89**

APPENDICES **101**

A Single-Leg Jump Landing Results of P2 – P10 Profiles **102**

A.1 BCs and Results from Single-Leg Jump Landings of P2 – P10 Profiles . . 102

List of Figures

2.1 Anatomical planes and directions 5
2.2 Human knee joint anatomy 6
2.3 Knee musculature, adapted from Moore and Dalley (2013) 8
2.4 ACL anatomy, adapted from Petersen and Zantop (2007) 10
2.5 Lower limb manoeuvers responsible for non-contact ACL injury 12
2.6 Schematic of the dynamic knee simulator (DKS) at the University of Waterloo 16
2.7 A tetrahedral (left) and a hexahedral (right) element 20
2.8 Stress-strain relationship of male and female ACL under uniaxial tension . 24
2.9 DVRT placed on the ACL to record displacement in the experiments . . . 27
2.10 Previous and current research on single-leg jump landing 27

3.1 Overview of the procedure to develop and validate a subject-specific FE model 29
3.2 Cadaver specimen, PK1 30
3.3 MRI sequences obtained for the current study 31
3.4 Segmentation process of bones and soft tissues in 3D Slicer 32
3.5 Smoothing of femoral cartilage geometry in SolidWorks 32
3.6 Segmented models of bones and soft tissues after smoothing in SolidWorks 33
3.7 MircoScribe digitizer and digitization procedure 34
3.8 Bony landmarks on the femur (left) and tibia (right) 35
3.9 Procedure followed to digitize the ligament insertion sites in the current study 35
3.10 Medial and lateral tibial slopes measured on the CT scan 36
3.11 Hexahedral mesh output of the knee soft tissues 37
3.12 Thin elements in the lateral tibial cartilage mesh 38
3.13 Multi-block meshing procedure in IA-FEMesh 38

3.14 Deletion of excessively distorted boundary elements 39
3.15 Hexahedral meshes of all cartilages after post-processing in HyperMesh . . 39
3.16 Tetrahedral meshes of the bones in the knee joint 40
3.17 8-noded hexahedral element and its hourglassing modes 41
3.18 4-noded tetrahedral element 42
3.19 Definition of TIE constraint between the patella and patellar cartilage . . . 43
3.20 Contact definition between various surface pairs in the FE model 43
3.21 Axial connector definition in Abaqus CAE 45
3.22 AM bundle strain versus anterior force on the tibia (Lachman test) 45
3.23 Force versus displacement curves of ACL 46
3.24 Force versus displacement curves of ligaments by Blankevoort et al. (1991) 47
3.25 Secondary ligaments between patella, femur and the tibia 48
3.26 Secondary ligaments in tibia 49
3.27 Rigid bodies at the ends of menisci 49
3.28 Knee co-ordinate system 50
3.29 Boundary conditions for flexion (left) and pure abduction (right) simulations 51
3.30 Boundary conditions for Lachman (left) and anterior draw (right) simulations 52
3.31 Single leg jump landing simulation timeline 54
3.32 Hip and ankle kinematics of P1 participant profile 54
3.33 Location of application of muscle forces in the FE model 55
3.34 Measurement of moment arms by tendon excursion technique 56
3.35 Muscle forces (left) and hip moment (right) of participant profile P1 56
3.36 ACL strain with different material properties assigned to cartilages 58
3.37 Meniscal strain measurement 59

4.1 Summary of hexahedral element quality of the knee soft tissue meshes . . . 62
4.2 ACL strain with increasing flexion angle (active range of motion) 63
4.3 Internal tibial rotation with flexion 63
4.4 AM bundle strain during Lachman (top) and anterior drawer (bottom) simulations 64
4.5 ACL strain during pure abduction 65

4.6 Knee valgus rotation during pure abduction . . . 65
4.7 Verification of model kinematics of P1 profile with OpenSim output . . . 66
4.8 Jump landing stages (top) and verification of model kinetics (bottom) . . . 67
4.9 Relative ACL strains during half muscle force jump landing . . . 68
4.10 Comparison of peak and time to peak ACL strain in half muscle force jump landing . . . 69
4.11 Posterior medial meniscal strains during half muscle force jump landing . . . 70
4.12 Relative ACL strains during full muscle force jump landing of P1 profile . . . 70
4.13 Computational ACL strains . . . 71
4.14 Comparison of peak ACL strains in P1 − P7 participant profiles . . . 72
4.15 Computational posterior medial meniscal strains . . . 73
4.16 Model energies during jump landing simulation of P1 participant profile . . . 74

5.1 ACL lengthening during flexion . . . 78
5.2 Relative ACL strains of P5 (left) and P6 (right) jump landing profiles . . . 80
5.3 Comparison of peak relative ACL strains (Polak (2019) and current study) 81
5.4 Comparison of peak relative ACL strains (Bakker et al. (2016) and current study) . . . 82
5.5 Comparison of mean peak ACL strain to other experimental studies . . . 83
5.6 Comparison of mean peak ACL strain to other computational studies . . . 84
5.7 ACL strains during full muscle force jump landings of P3 and P6 participant profiles . . . 84

A.1 P2 participant profile results . . . 103
A.2 P3 participant profile results . . . 104
A.3 P4 participant profile results . . . 105
A.4 P5 participant profile results . . . 106
A.5 P6 participant profile results . . . 107
A.6 P7 participant profile results . . . 108
A.7 P8 participant profile results . . . 109
A.8 P9 participant profile results . . . 110
A.9 P10 participant profile results . . . 111

List of Tables

2.1 Knee musculature (Moore and Dalley, 2013) 9
2.2 *In-vitro* dynamic studies on jump landing from literature 15
2.3 Classification of automatic segmentation methods 19
2.4 A literature review on automatic segmentation methods to extract knee geometries 19
2.5 A literature review on computational knee models simulating jump landing 23
2.6 A literature review on 1D non-linear spring models for ACL 26

3.1 Tissue donor information 30
3.2 Details of the MRI scans acquired for the current study 31
3.3 Summary of the material properties assigned to various anatomical structures 44
3.4 Material properties assigned to the major knee ligaments 47
3.5 Summary of kinematics verification studies 52
3.6 Participant information for jump landing trials, adapted from Bakker (2015) 53
3.7 Experimental data available for comparison of computational results 59

4.1 Details of the mesh of knee tissues in the FE model 61
4.2 Experimental and computational muscle moment arms of the specimen . . 66
4.3 Comparison of experimental and computational ACL strains 69
4.4 Peak and time to peak ACL strain of P1 − P10 participant profiles 72
4.5 Peak posterior medial meniscal strain of P1 − P10 participant profiles . . . 73

Chapter 1

Introduction

1.1 Motivation

Anterior cruciate ligament (ACL) is one of the primary stabilizers of the knee joint during activities of daily life such as walking, running, stair-climbing and jumping. Activities wherein the ACL experiences traumatic forces exceeding its mechanical threshold lead to its injury (Chandrashekar, 2005). Nearly 250,000 ACL injuries occur every year in North America alone (Griffin et al., 2006). Surprisingly, close to 75 % of these injuries are non-contact in nature, occurring due to sudden dynamic movements such as jump-landing, in sport-related activities placing young athletes at high risk (Boden et al., 2010; Renstrom et al., 2008). Surgical reconstruction of the ACL is often recommended to young athletes, and annually an estimated 100,000 reconstruction procedures are performed which costs around $ 7.6 billion, in the United States (Mather et al., 2013). Meniscal tears often accompany ACL injuries, a combination which increases the risk of osteoarthritis, a degenerative disease of the articular cartilage (Salem et al., 2018).

ACL injury rates continue to rise even with significant efforts directed towards understanding ACL injury mechanics (Mall et al., 2014). Currently, there is a lack of consensus and validation of various factors that lead to an ACL injury (Bakker et al., 2016). *In-vivo* measurement of ACL deformation during a potential injury-prone activity with sensors mounted on the ACL is dangerous and unethical (Kiapour, 2013). *In-vitro* experiments on cadaveric specimens, simulating dynamic loading conditions of high-risk injury scenarios like jump-landing, have been able to shed light on the underlying knee tissue mechanics. Hybrid approaches involving *in-vivo* and *in-vitro* experiments have been successfully attempted to replicate the physiological loading conditions during jump landing (Bakker et al., 2016).

The current study considers the *in-vivo* and *in-vitro* experimental contributions of Bakker et al. (2016) and the *in-vitro* and *in-silico* (computational) contributions of Polak (2019) in evaluating ACL strain during single-leg jump landings. Bakker et al. (2016)

undertook motion capture (*in-vivo*) study on single-leg jump landing of ten participants and experimentally tested (*in-vitro*) this motion on five cadaveric specimens to evaluate ACL strain. Moreover, Polak (2019) performed *in-vitro* experimental jump landings on three cadaveric specimens and computationally simulated the activity using a finite element (FE) model. Both experimental studies were successful in quantifying ACL strain in the physiological conditions of jump landing. However, these experiments are strenuous, time-consuming and have limited sample sizes. It is also expensive to acquire and prepare cadaveric test specimens. In contrast, computational modelling using the finite element method presents as a viable alternative.

While Polak (2019) addressed the experimental limitations by simulating jump landing on a computational model, this model did not include the anatomy of the experimentally tested cadaveric specimens. Subject-specific FE models include accurate anatomical features of a particular subject and can predict the associated joint tissue mechanics and injury risk. However, the accuracy of predictions depends on robust development and validation of the model. This study proposes a subject-specific computational modelling approach to evaluate ACL strain during jump landing and validating the model using existing experimental results.

1.2 Objective

The primary objective of this research was to develop a subject-specific knee FE model to simulate a jump landing motion and validate ACL strain output based on the results of previous *in-vitro* single-leg jump landing experiments. The specific objectives were:

1. Develop a subject-specific knee FE model using imaging data of a cadaver specimen, tissue-specific meshing approaches, and published data for tissue material properties
2. Verify the joint kinematics and ACL strains generated with the subject-specific FE model against joint laxity tests from published experimental data
3. Apply the subject-specific FE model to simulate single-leg jump landings of ten participant profiles from the *in-vitro* experimental study by Bakker et al. (2016) to determine the ACL and medial meniscal strains and verify them against the experimental results

1.3 Thesis Overview

This thesis is organized into the following six chapters. Synopsis of each chapter is as follows. Chapter 1 (Introduction) sets the premise for the research conducted. Chapter 2 (Background) introduces the anatomy of the lower limb, ACL injury mechanics, and

relevant background research related to medical image segmentation, mesh generation, dynamic FE models. A brief history of the single-leg jump landing experiments conducted on the Dynamic Knee Simulator at the University of Waterloo is also discussed. Chapter 3 (Methodology) is divided into two main sections. The first section details the steps taken to generate a subject-specific model, including cadaver imaging and anatomy segmentation, mesh generation and setup of the FE model. The second section details the kinematic verification studies on ACL mechanics, including participant data and boundary conditions of single-leg jump landing simulation. Chapter 4 (Results) presents all the results of the study, including mesh quality, the ACL strain during the half and full muscle force jumps, and lastly energy balance of the jump landing simulation. Chapter 5 (Discussion) examines the results of the current work in comparison to the available studies in the literature. Chapter 6 (Conclusions) presents the main conclusions of this research, along with a discussion of the study limitations and future research directions.

Chapter 2

Background

2.1 Anatomical Background

Application of the principles of engineering to understand the mechanics of injury requires background knowledge of the human body anatomy. This necessitates defining the standard terms and definitions adopted to describe the positions of different parts of the body relative to each other. The following section provides an overview of anatomical nomenclature and knee-specific anatomy.

2.1.1 Nomenclature

Three anatomical planes namely, *sagittal* (dividing the body into left and right), *coronal/frontal* (dividing the body into front and back) and *axial* (dividing the body into head and torso) are defined to identify cross-sections and motions (Figure 2.1). In addition, the directional pairs define position of a structure relative to another: *anterior-posterior* (A-P) (towards the front or back of the body), *superior-inferior* (S-I) (towards the head or feet), *medial-lateral* (M-L) (towards or away from the mid-line of the body), *proximal-distal* (closer to or away from the torso) and *superficial-deep* (towards or away from the skin) (Figure 2.1).

All the motions of the human body can be categorized as occurring in one or more of the anatomical planes. The basic motions are *flexion-extension* (sagittal plane motion), *adduction-abduction* (coronal/frontal plane motion) and *internal* and *external rotations* (axial plane motion).

A *joint* is a place where the ends of two bones meet in the body. Joints are classified based on the nature of the union of the bones involved in the joint. A joint can be *synovial*, *fibrous* or *cartilaginous* (Moore and Dalley, 2013). In a synovial joint, the entire joint is covered in a capsule, the ends of the bones have a layer of articular cartilage, and the

joint capsule is lubricated with synovial fluid. Synovial joints have an extensive range of motion compared to the other types of joints, and the ligaments present in the joint restrain them. Examples of the synovial joints include the shoulder, knee, hip, elbow, wrist and the atlantoaxial (neck) joints.

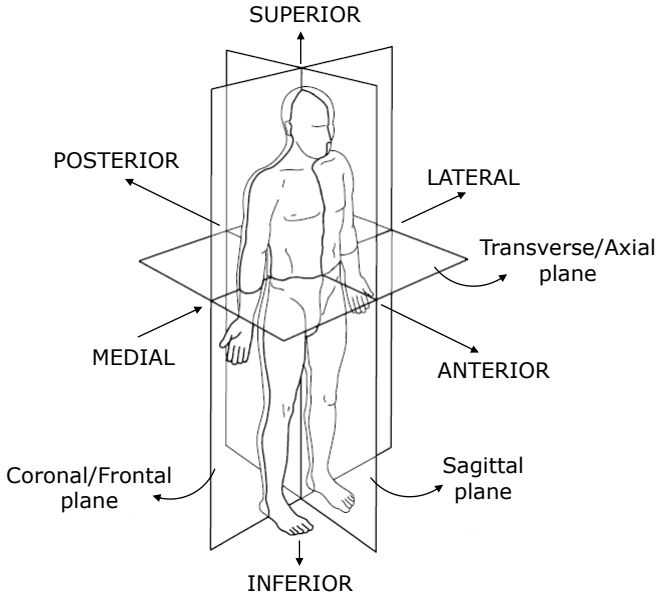

Figure 2.1: Anatomical planes and directions
(adapted from Inman et al. (1981))

The fibrous and cartilaginous joints are characterized by the presence of fibrous or cartilaginous tissue to connect bones and have no or limited range of motion. Examples of fibrous joints include the joints in the skull bones, and the joints between the intervertebral discs constitute the cartilaginous joints.

2.1.2 Knee Anatomy

The knee joint is a synovial joint, allowing motion mainly in the sagittal plane, but also allows for small rotations in the axial and coronal planes. It is the union of the *femur*, *tibia* and *patella* bones, their ends enclosed in a joint capsule. Another bone, which laterally attaches to the tibia and not involved in the actual joint is the *fibula*. Articular cartilage layers the ends of each of the bones in the joint, which creates a lubricated, low friction environment for load transmission between bones (Fox et al., 2009) (Figure 2.2).

The knee joint is composed of *patellofemoral* and the *tibiofemoral* joints based on the two distinct articulations between patella-femur and tibia-femur bones. The tibiofemoral joint is responsible for the transmission of axial loads such as the body weight, and the

patellofemoral joint is responsible for increasing the effect of muscle (quadriceps) forces, with the patella acting as a lever thereby providing a mechanical advantage. The distal end of the patella is connected to the tibial tuberosity by the *patellar tendon* (or *patellar ligament*).

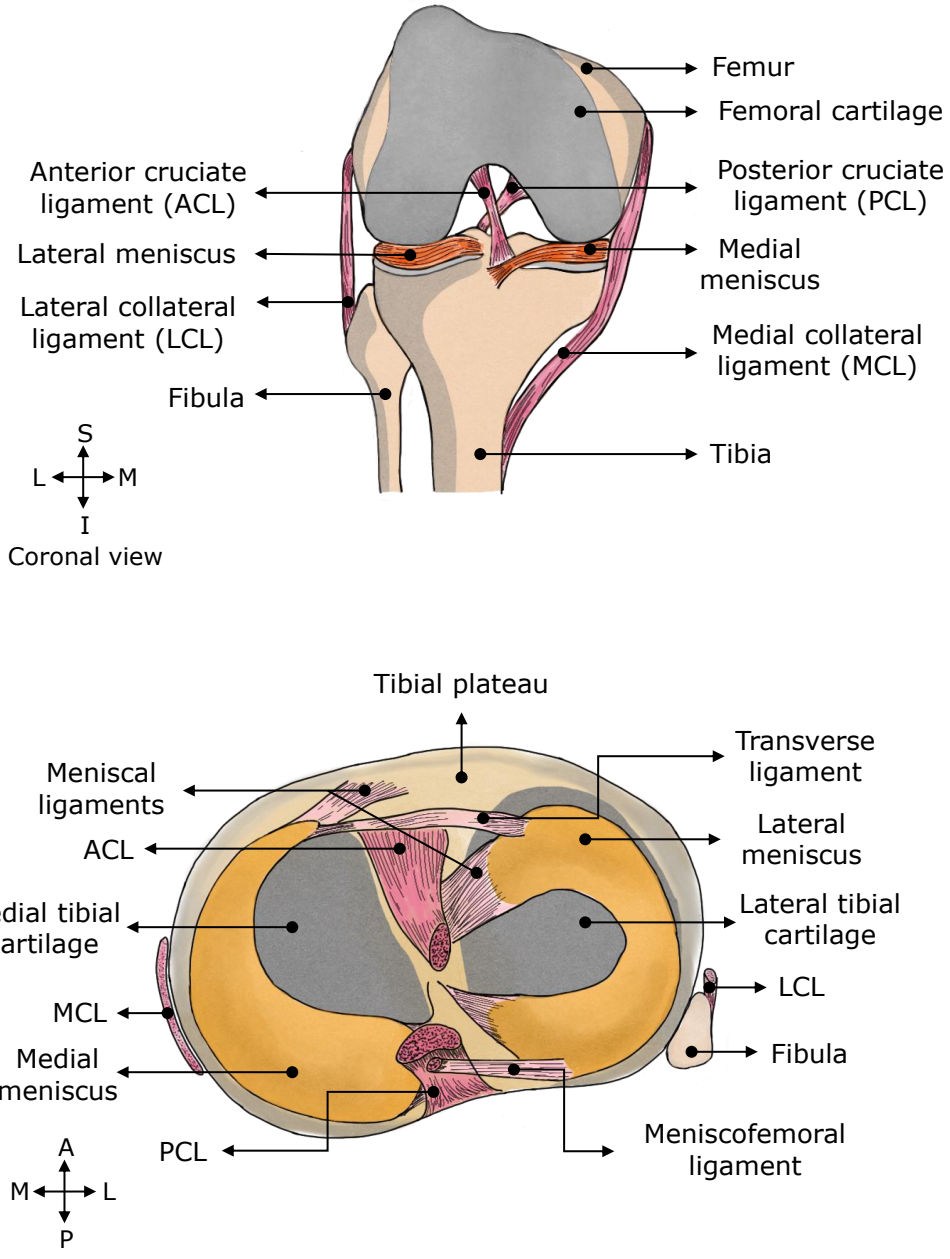

Figure 2.2: Human knee joint anatomy
(adapted from Moore and Dalley (2013)). Anterior view of a flexed right-knee (top) and superior view of the tibial plateau (bottom)

Knee Ligaments

Ligaments in the knee joint are responsible for its complex kinematic responses during day-to-day activities (Trad et al., 2018). The major ligaments in the knee joint are the anterior and posterior cruciate ligaments (ACL and PCL) and the medial and lateral collateral ligaments (MCL and LCL). The cruciate ligaments are contained within the knee joint, whereas the collaterals enclose the joint on the medial and lateral sides.

The cruciate ligaments run between the intercondylar space of the femur and the tibial plateau, crossing each other like the letter 'X'. The ACL and PCL are named for their attachment sites on the tibial plateau. The ACL attaches anteriorly on the tibial plateau, runs laterally and attaches onto the lateral femoral condyle in the intercondylar space. The PCL, on the other hand, has a posterior attachment on the tibial plateau, runs medially and attaches onto the medial femoral condyle in the intercondylar space (Zantop et al., 2006). The primary function of the ACL is resisting anterior tibial translation (ATT) and internal tibial rotation, whereas the PCL is the primary restraint against posterior tibial translation (PTT) and external tibial rotation.

The MCL inserts on the medial epicondyle of the femur and has a broader attachment on the tibia distally. The MCL has two distinct fibres, superficial MCL and deep MCL. The deep MCL attaches to the medial meniscus distally. LCL is narrower than the MCL and connects the lateral epicondyle of the femur to the fibula. The LCL runs posteriorly and inferiorly from the femoral attachment to the proximal head of the fibula. MCL and LCL are the primary stabilizers against valgus (abduction) and varus (adduction) moments on the knee joint.

Besides the ligaments and the articular cartilage, the knee joint also houses two crescent-shaped structures called *menisci* between the medial (medial meniscus) and the lateral (lateral meniscus) aspects of the tibial plateau and the femoral condyles. They wedge the gap formed by the convex ends of the femur condyle and the flat tibial plateau. These are cartilaginous tissues which aid in shock absorption, distribution of the load from the femoral condyles to the tibial plateau and lubrication of the joint (Fox et al., 2012) (Figure 2.2). The menisci are firmly attached to the tibial plateau via the meniscal ligaments, and the transverse ligament connects the anterior portions of the two menisci.

In addition to the ligaments described above, other ligaments also exist in the knee joint such as: *medial and lateral patellofemoral ligaments*, *medial and lateral patellotibial ligaments*, *meniscofemoral ligaments* and *capsular ligaments* that act as the static stabilizers of the knee joint (Rhee et al., 2012).

Knee Musculature

The forces and moments required for the motion of the knee joint are caused by three major muscle groups: *quadriceps femoris*, *hamstrings* and the *gastrocnemius* (Figure 2.3).

Quadriceps femoris (or Quadriceps), a group of four muscles, is the primary extensor of the knee joint. Besides, it also flexes the hip and is an important muscle involved in the normal gaits such as walking, running and squatting. The hamstrings are a group of three muscular bands responsible for knee flexion and hip extension. The gastrocnemius is composed of two muscles which stretch from the knee to the heel and causes knee flexion and plantar-flexion (flexing of the foot so it faces inferior) of the ankle. A brief description of each component of the muscle group is given in Table 2.1

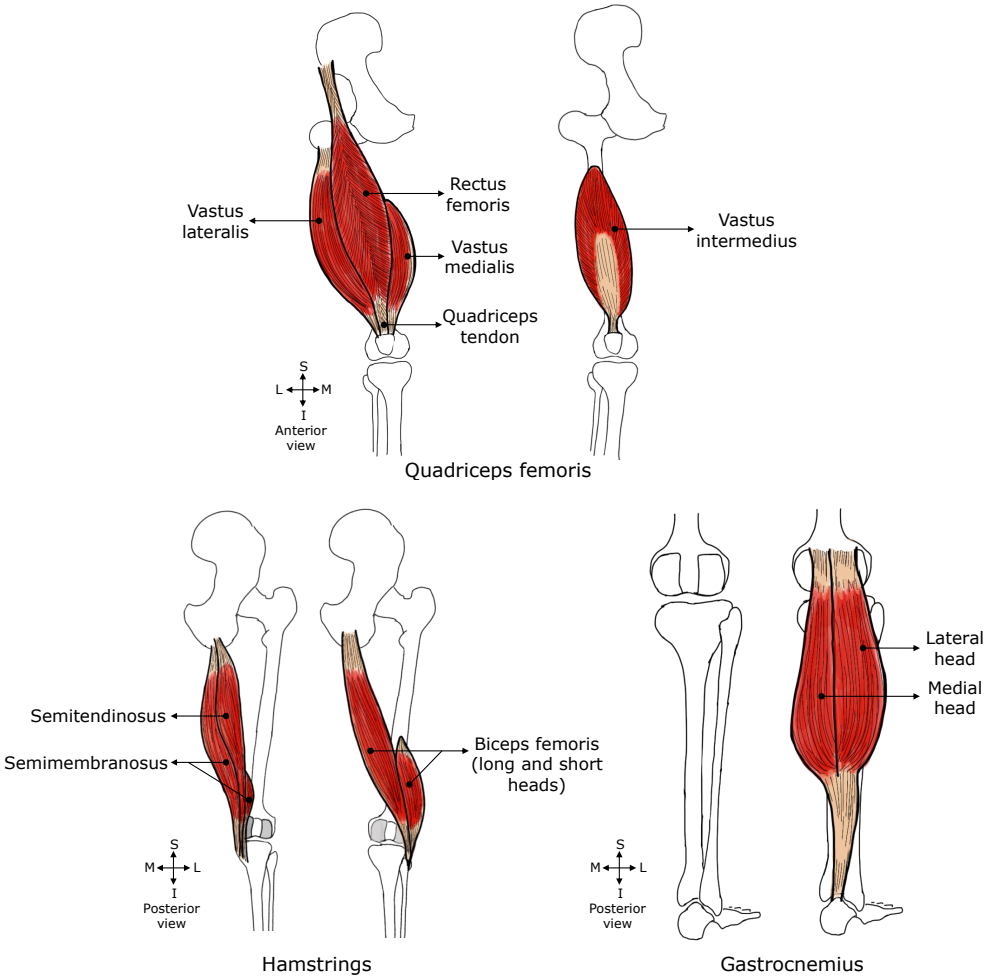

Figure 2.3: Knee musculature, adapted from Moore and Dalley (2013)
Quadriceps (top), Hamstrings (bottom left) and Gastrocnemius (bottom right)

Additionally, popliteus muscle attaches to the lateral aspect of the femur via the popliteus tendon and the runs medial and inferior to attach onto the medial aspect of the tibia. It is responsible for unlocking the knee joint by rotating the femur or the tibia during flexion. Apart from the major muscle groups listed, there are several minor muscle groups, which are also responsible for the motion of the lower limb, in the axial and coronal planes.

Table 2.1: Knee musculature (Moore and Dalley, 2013)

Muscle group	Contribution	Components	Attachment location	
			Proximal	Distal
Quadriceps femoris	Knee extension; hip flexion	*Rectus femoris*	Illiac spine in the pelvis	Quadriceps tendon
		Vastus lateralis	The base of greater trochanter	Lateral quadriceps tendon
		Vastus intermedius	Anterior, lateral femoral surface	Quadriceps tendon
		Vastus medialis	Anterior, medial femoral surface	Medial quadriceps tendon
Hamstrings	Knee flexion; hip extension	*Biceps femoris* (*short head*)	Lateral supracondylar line of femur	Lateral fibular head
		Biceps femoris (*long head*)	Ischial tuberosity on the pelvis	Lateral fibular head
		Semi-membranosus	Ischial tuberosity on the pelvis	Medial tibial surface
		Semi-tendinosus	Ischial tuberosity on the pelvis	Medial tibial surface
Gastroc-nemius	Knee flexion; ankle plantar-flexion	*Medial gastrocnemius*	Medial aspect of femoral condyle	Calcaneus (heel) via Achilles tendon
		Lateral gastrocnemius	Lateral aspect of femoral condyle	Calcaneus (heel) via Achilles tendon

2.1.3 ACL Anatomy and Function

Similar to other ligaments, the ACL is a fibrous connective tissue made up of collagen fibres arranged in a matrix containing ground substance containing proteins and water. Based on its microscopic constituents, it is distinguished into three regions: proximal (containing round and ovoid cells), middle (containing dense collagen fibres) and distal (containing ovoid cells and few collagen fibres) (Duthon et al., 2006). The collagen fibres are responsible for the tensile properties of the ACL. The ACL has a mean length of 32 mm, and its width ranges from 7 mm to 12 mm (Amis and Dawkins, 1991) and attaches to the lateral intercondylar fossa of the femoral condyle superiorly and runs to the lateral aspect of the anterior tibia inferiorly (Figure 2.4). The primary function of the ACL is to resist anterior tibial translation and internal tibial rotation.

ACL receives its nerve supply from the tibial nerve and triggers muscle firing in the

knee joint. These nerves are sensitive to excessive stretching and postural changes. ACL has blood supply from the middle genicular artery and is more vascularized in the proximal part than the distal part, which results in poor healing of the ligament after an injury.

Anatomically the ACL consists of three separate bundles: anteromedial (AM), intermediate (IM) and posterolateral (PL) bundles, yet most of the computational models represent the ACL by the AM and PL bundles since it is difficult to distinguish the IM bundle among them (Duthon et al., 2006) (Figure 2.4). The PL bundle attaches to the tibia slightly posteriorly and laterally and also attaches inferiorly on the intercondylar fossa of the femoral condyle compared to the AM bundle.

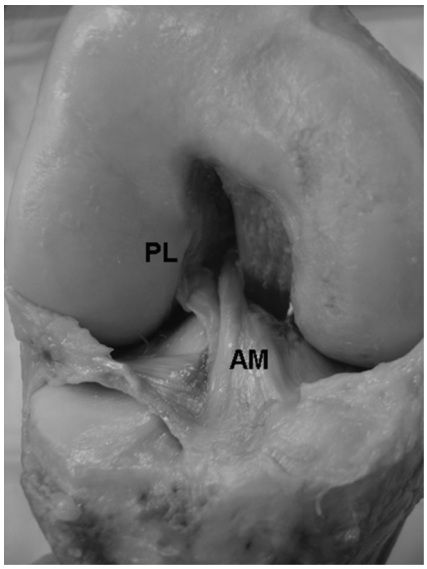

Figure 2.4: ACL anatomy, adapted from Petersen and Zantop (2007)
AM: Anteromedial bundle, PL: Posterolateral bundle

When the knee is extended, both bundles are in tension, and the PL bundle resists ATT strongly than the AM bundle. As the leg flexes, the PL bundle becomes slacker, due to the nature of its position and alignment. AM bundle resists most of the anterior load when the knee is flexed (Sakane et al., 1997).

2.2 ACL Injury

ACL injuries severely impair the normal function of the knee joint. Excessive ATT, large internal and external rotations of the lower limb are the primary causes for the injury. Close to 75 % of ACL injuries do not involve direct physical contact with the knee (Boden et al., 2010). These occur due to sudden change in the direction of motion, frequent in sport manoeuvres involving cutting, planting, pivoting and jump landing (De Vita, 2005).

ACL injuries often lead to meniscal injuries due to increased loads on the menisci in the ACL deficient condition. In an ACL deficient knee, medial meniscus becomes the knee's primary anterior-posterior stabilizer (Smith and Barrett, 2001). Medial and lateral meniscal tears accompany more than 25 % and 31 % of ACL injuries, respectively (Potter et al., 2012). However, medial meniscus tears occur more frequently. In the analysis of 575 meniscal tear patterns, Smith and Barrett (2001) found 99.4 % of medial meniscus tears occurred on the posterior periphery of the structure. Moreover, ACL injuries also influence osteoarthritis (OA), a degenerative disease in the cartilage, which leads to rubbing of bones with each other, causing extreme pain and discomfort (Potter et al., 2012). Canes and knee braces, in the early stages of OA and joint replacement surgeries, in the later stages, remain the only options to manage OA.

In younger athletes, aged 14-19 years, the occurrence of ACL injury is particularly high (Renstrom et al., 2008). There is evidence that females are at higher risk of ACL injuries than males. Four times greater incidence of ACL injury was found in young female basketball players compared to their male counterparts (Renstrom et al., 2008).

Factors affecting ACL injury are classified as either *intrinsic*, such as the anatomical features of the knee or *extrinsic*, such as the kinematic and muscular loads due to voluntary motion. Due to the multi-factorial dependence of ACL injury risk, some researchers focus on a population study to record the injury pattern while others resort to experimental approaches such as *in-vivo*, *in-vitro* and computational studies to evaluate injury mechanics.

Intrinsic Factors

Factors such as the ACL size, tibial slopes, femoral notch width, knee joint laxity are all found to be the predictors of ACL injury (Shultz et al., 2012). Individuals with a smaller cross-sectional area and volume of ACL experience higher stress and absorb lesser energies under a given load and are predicted to be at a higher risk of injury, which is especially true in females since they have significantly smaller ACLs than males (Chandrashekar et al., 2005). Another widely researched metric is the tibial slope, which is the inclination of medial and lateral tibial plateaus from the line perpendicular to the longitudinal tibial axis (Giffin et al., 2004). Higher tibial slopes are correlated with an increase in the anterior forces onto the tibia under axial compressive loads, thereby increasing ATT (Hashemi et al., 2008; McLean et al., 2011). The female population is found to have higher medial and lateral mean tibial slopes (5.9° and 7.0°) than men (3.7° and 5.4°) and is determined to be at a greater risk of injury under compressive loads (Hashemi et al., 2008).

In addition, the femoral notch width is also considered as a predictor of ACL injury risk. Although no standardized method to measure the notch width exists currently, a study by Ireland et al. (2001) found that, in the cohort of 294 young subjects (108 with ACL injury and 186 with no injury) who played sports, smaller femoral notch width led to a higher risk of ACL injury.

Further, knee laxity such as anterior knee laxity and internal rotation laxity is found to be associated with risky landing scenarios, especially in females which in turn increases the risk of ACL injury (Shultz et al., 2012).

The *in-vitro* jump landing study of Bakker et al. (2016), a basis for the current study, found that most of the variance in ACL strain during jump landing between the cadaveric specimens were dictated by the difference in the intrinsic factors of the cadavers, thus stressing the influence of anatomical factors on ACL strain.

Extrinsic Factors

Extrinsic factors involve kinematics of the lower limb, such as the trunk, hip and knee flexion angles, and kinetics such as muscle forces and moments acting on the joint during injury prone lower limb motions (Figure 2.5). In these activities, ligament-loading patterns are observed using *in-vivo*, *in-vitro* or *in-silico* (computational) approaches.

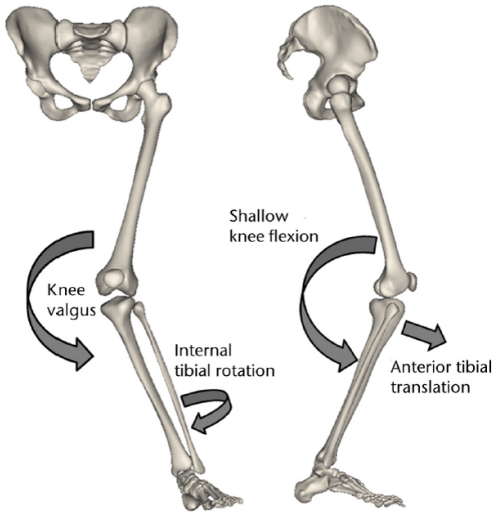

Figure 2.5: Lower limb manoeuvers responsible for non-contact ACL injury (adapted from Kiapour and Murray (2014))

Single-leg jump landing is one of the widely discussed non-contact sport manoeuvres, which results in an ACL injury. Ground Reaction Force (GRF), which is the reaction force from the ground to the force applied by the foot during landing, is a critical factor which causes ACL injury. High GRFs generated at the time of foot contact with the ground are likely to generate injury-causing forces in the ACL (Serpell et al., 2012). This is the reason for the extensive investigation of single-leg jump landing motion in literature. Here, the mechanics of the sagittal plane play a key role in determining the injury risk. Landing techniques with increase in the trunk flexion (leaning forward) and knee flexion angles are

found to lower the peak GRF and lower the anterior shear force on the tibia, leading to reduction in ACL loads (Podraza and White, 2010; Shimokochi et al., 2013).

The quadriceps force is one of the primary contributors of sagittal plane mechanics and is considered detrimental to ACL injury since this force increases the ATT (Myers et al., 2012). Withrow et al. (2006) examined the relationship between quadriceps force and knee flexion during *in-vitro* jump landing simulations and concluded that ACL strain was proportional to the quadriceps force and knee flexion angle. However, some studies predict otherwise. Hashemi et al. (2007) claimed that the only situation where quadriceps force could injure the ACL is when the GRF is absent, which is unrealistic. According to the authors, in realistic conditions, where the GRF is present, an increase in quadriceps forces leads to an increase in joint compressive forces and prevents the anterior translation of the tibia, thus protecting the ACL. Favourably, in the *in-vitro* jump landing simulations of Bakker et al. (2016), no correlation was found between increasing quadriceps forces and ACL strain. The study also suggested that the quadriceps force has limited effect on ACL strain in combination with higher flexion angles.

In addition, the role of hamstring muscle on ACL loading during jump landing has also been examined. Shimokochi et al. (2009) found that the increase in the use of hamstrings along with the quadriceps (muscle co-contraction) reduces knee extension moments and thereby protects the ACL. Besides, the authors argued that landing strategies with effective use of plantar-flexion moments at the ankle joint could absorb the high GRFs and reduce the loads on ACL.

Further, knee kinematics in the coronal plane were also found to influence ACL loading. In the study by Hewett et al. (2005), evidence of altered mechanics of the lower limb was found in the ACL injured population. Out of the 205 female athletes recruited for the study, nine ACL injuries were recorded in 13 months. Motion capture was conducted at the start of the study to observe the variance in landing strategies among the athletes. Increase in coronal plane variables such as knee valgus and abduction moments was correlated to increased risk of ACL injury.

Due to the viscoelastic nature of the ACL, strain rate influences are apparent in injury scenarios. In the *in-vivo* jump landing simulations of Hashemi et al. (2007), up to 250 %/s strain rate was observed when the ACL was injured whereas the strain rates were only 60 %/s to 80 %/s during safe landing. In another *in-vitro* study by Oh et al. (2012), internal tibial torques were shown to be injurious to ACL during pivot landing. The strain rates in ACL during internal tibial torque were 42 % higher than the strain rate during external tibial torques.

2.3 Experimental Research

Experimental approaches such as *in-vivo*, motion capture and videotape analysis methods and *in-vitro* mechanical testing are employed by researchers to evaluate the intrinsic and

extrinsic injury risk factors listed previously.

Although *in-vivo* studies involving direct ACL strain measurements have inherent complications due to the inaccessibility of the ACL and risk of injury to the subjects involved, the research group at the University of Vermont studied the behaviour of ACL under normal muscle functions and rehabilitation conditions such as squatting, flexion-extension, and anterior tibial loads. Hall Effect Strain Transducer (HEST) and Differential Variable Reluctance Transducer (DVRT) were used to measure anteromedial ACL strain (Beynnon et al., 1997; Beynnon et al., 1992a; Beynnon et al., 1992b).

ACL strain was also measured non-invasively in an *in-vivo* experiment by (Taylor et al., 2011) during a jump landing scenario. Motion capture data of eight male subjects performing a single-leg jump was obtained. Fluoroscopy and MRI imaging techniques were used to find the relative positions of the femur and tibia throughout the trial, and the strain was measured using the images. Peak strain (relative to the length in the MRI) was reported as (12 ± 7) % occurring at (55 ± 14) millisecond (ms), before ground contact at the lowest flexion angle.

While ACL strain was not measured, Myers et al. (2012) conducted *in-vivo* landing studies on ten female subjects and measured important kinematics using biplane fluoroscopy. They found that ATT was the highest at (5.6 ± 1.9) mm at ground contact. They also stated that a healthy knee is well equipped to perform such demanding tasks.

Videotape analysis is another type of study where the kinematics of ACL injury is studied using a taped recording of the events leading to the injury. In the study of Podraza and White (2010), video tapings of ten male recreational athletes were analyzed for segment kinematics during jump landing and concluded that flexed knee during landing is favourable. Koga et al. (2010), with the analysis of ten ACL injury video tapings, stated that the injury occurred 40 ms after the initial ground contact, caused by internal rotation of the tibia coupled with valgus rotation.

In-vitro studies are commonly cadaveric studies wherein the input data for the experiment is derived from a motion capture study or capturing muscle activity using electromyography (EMG). Motion capture involves recording kinematic data of any activity using body markers, angle goniometers and force plates. EMG sensors are used to record muscle-firing patterns during an activity. Kinematic variables and muscle forces are then derived using multibody dynamics software. Further, these studies usually have a mechanical device to simulate activities on cadaver specimen. The research groups at the University of Michigan, Ohio State University, Texas Tech University and the University of Waterloo developed knee simulators to study the effects on ACL strain during impact like activities such as jump landing. Table 2.2 shows a summary of the jump landing experimental studies performed on these simulators. The important outcomes of these studies were discussed in Section 2.2.

Table 2.2: *In-vitro* dynamic studies on jump landing from literature

Study	Year	Simulator at University	Peak ACL Strain (mean ± SD)	Key findings
Withrow et al.	2006	Michigan	2.9[1]	Increase in quadriceps force increased ACL strain
Hashemi et al.	2007	Texas Tech	10.4[1]	Quadriceps forces did not affect ACL strain
McLean et al.	2011	Michigan	3.35 ± 1.71	Anterior tibial acceleration and posterior tibial slope correlated with ACL strain
Kiapour et al.	2013	Ohio State	6.7 ± 1.8	Peak ACL strain coincided with peak GRF

Variations in the peak ACL strains of the experimental studies listed in Table 2.2 stems from the fact that the mechanism of loading (or the boundary conditions of) the cadaver specimen to mimic the jump landing motion were different. In the Michigan simulator, a 150 N weight was dropped on a dissected cadaver specimen with pre-tensioned quadriceps, hamstrings and calf muscles, while the knee was maintained at 25° flexion angle, to simulate a jump landing. In the Ohio simulator, the cadaver knee specimen had the foot and the ankle joint intact with the femur cut midway and mounted in an inverted position with the foot facing up. A 700 N load was dropped on the foot from heights of 30cm and 60cm to simulate a jump and ACL strain was recorded. In the Texas Tech simulator, impact loads between 1100 N and 1400 N were applied to recreate the impact during jump landing while the knee was maintained at different flexion angles between 10° and 40°. Only quadriceps and hamstring muscle forces were accounted for using electric actuators, while the effect of other muscles was neglected. In all these simulators, a DVRT was used to record ACL strain during the activity.

The common characteristic of the knee simulators described is that impact loads are applied instantaneously to create the effect of GRF in a jump landing scenario. However, these are not considered to adequately represent physiological conditions during a jump landing event (Bakker et al., 2016). The simulator at the University of Waterloo developed by Cassidy et al. (2013) (Figure 2.6) addresses a few critical limitations in the other knee simulators such as application of dynamic changes in the hip and ankle kinematics and application of dynamic muscle forces in the sagittal plane (Bakker et al., 2016). Dynamic muscle forces (force versus time) of quadriceps, hamstrings and gastrocnemius (Calf) are applied through metal cables via electromechanical actuators. In addition, hip extension moments are applied through a hip actuator placed under the hip attachment. Cassidy et al. (2013) developed a workflow to measure ACL strain, which involved *in-vivo* motion

[1]calculated mean strain from the reported values

capture, generation of muscle forces from a musculoskeletal model using the motion capture data and measurement of ACL strain *in-vitro*. Only one cadaver knee specimen was tested, and a relative peak strain of 4.3 % was recorded, which occurred after 90 ms of ground contact.

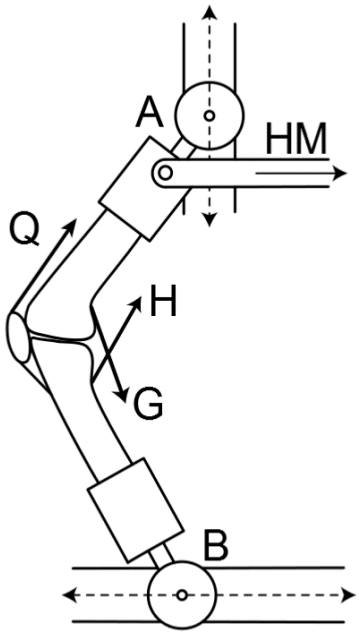

Figure 2.6: Schematic of the dynamic knee simulator (DKS) at the University of Waterloo (adapted from Bakker (2015)). A, B: Hip and ankle actuators. Q, H, G: Quadriceps, Hamstring and Gastrocnemius muscle forces applied through steel cables. HM: Hip moment actuator

On the DKS, Hangalur et al. (2016) tested the efficacy of a prophylactic knee brace in reducing ACL strains during jump landing. On the cadaver specimen acquired for the study, an unbraced jump was also performed, and an average strain of 20 % was recorded, at less than 50 ms after ground contact. Following a similar approach, an extensive study on ACL behaviour was carried out by (Bakker et al., 2016). The authors reported an 8.9 % average relative ACL strain from the *in-vitro* jump landing simulations of seven different participant profiles on five cadaver specimens. Hip flexion angle and trunk flexion angle at maximum GRF were identified as the significant influencers for ACL strain, apart from the intrinsic factors. Using regression models, they also concluded that landing with lower hip and trunk flexion angles (erect postures) increases ACL strain. Also, it was noted that ACL strain increased with GRF and the bodyweight of the subjects involved. Following the same approach, additional *in-vitro* jump landing experiments were carried out by Polak (2019) based on two participant profiles from Bakker et al. (2016) study. Peak ACL strain of (4.4 $\pm$ 1.8) % was reported, occurring between 54 ms and 89 ms after ground contact, from the two cadaver specimens tested in the study.

2.4 Computational Research

Computational modelling can be an effective alternative to experimental testing for simulation of dynamic loading conditions. Experimental testing of dynamic loading conditions is challenging and ultimately produces limited data from traditionally small sample sizes. There have been numerous computational models developed which have evaluated several extrinsic factors affecting ACL injury. These include mathematical models (Abdel-Rahman and Hefzy, 1993; Wismans et al., 1980), musculoskeletal dynamics models (Bakker et al., 2016; Kia et al., 2016; Marra et al., 2015) and FE models (Kiapour et al., 2013; Polak, 2019). In a mathematical model, the behaviour of various components is governed by mathematical equations whereas, in a musculoskeletal model, motion (marker data) data are given as inputs and forces in the muscles, ligaments, and other tissues are determined by analysis of inverse dynamics. FE modelling is a well-known numerical method used to find approximate solutions to a problem with defined boundary conditions; however, these complex models often depend on experimental research for the input boundary conditions and material properties. In addition, experimental data is also necessary for model calibration, verification and validation. In order to ensure that the model predicts reasonable outcomes, verification and validation studies are conducted on a new model or an existing model used for a new loading condition. Verification studies ensure that the model output represents exactly the underlying mathematical implementation and validation studies ensure that the model outputs are in accordance with the real-world outcomes under the same loading conditions (Henninger et al., 2010). Calibration involves modifying the input conditions of the model such as material properties to achieve a desired outcome, for example, to replicate an experimental result.

In a few studies, computational models were obtained by averaging the geometries of acquired cadaver specimens (Garg and Walker, 1990) or using population-based FE models (Beillas et al., 2007, 2004). Garg and Walker (1990) developed a 3D model of the knee joint to evaluate the effects of tibial surface geometry and component placement on knee range of motion after total knee replacement surgeries. Beillas et al. (2007, 2004) simulated the tibiofemoral joint response during a one-legged hop on a generic 50^{th} percentile male FE model.

2.4.1 Subject-Specific Models

The accuracy of geometrical features of biological tissues in a computational model plays a significant role in obtaining an appropriate model response. Therefore, most of the computational models in the literature were developed by imaging the subject or the specimen involved in the study. Such models are called *subject-specific* models since they possess accurate anatomical features of a particular subject. Many subject-specific computational knee models exist in the literature evaluating knee mechanics in healthy (Baldwin et al., 2012; Harris et al., 2016) and pathological conditions (Ali et al., 2017; Halonen et al., 2016).

Recently, the right lower limb component of the Global Human Body Models Consortium (GHBMC) model (Schwartz et al., 2015) which is a full human body FE model of a 50^{th} percentile male, was used by Polak (2019) to compute ACL strain during a single-leg jump landing activity with the boundary conditions derived from Bakker (2015). In this computational study, jump landing profiles of two different participants from Bakker (2015) study were simulated and peak ACL strains of 4.2 % and 13.9 % occurring at 60 ms after ground contact were reported.

The first step in the generation of subject-specific FE model is identifying the 3D geometry of the anatomy of interest, typically obtained using medical imaging of the subject/specimen. Computed tomography (CT) and Magnetic resonance imaging (MRI) are the standard 3D medical imaging methods used to scan desired anatomical regions. CT scans are primarily used to visualize bone geometries due to the excellent contrast of bone tissue on X-ray. MRI scans offer excellent visibility of soft tissues, with different MRI pulse sequences used to identify different tissue contrasts.

Segmentation

Three-dimensional (3D) models from a medical image are obtained through a process called *segmentation*. It involves applying a label field to image voxels (pixels in 3D) with similar characteristics (greyscale intensity or texture) to divide an image volume into several connected regions of interest. The segmentation process, when repeated on all the images (or slices) in a scan, results in a 3D model. Medical image analysis software such as *Scan IP* (Synopsys, CA, USA), *Mimics* (Materialise NV, Leuven, Belgium), *Amira* (ThermoFisher Scientific, MA, USA) and *3D Slicer* (`www.slicer.org`) are commonly used for segmentation. In the current study, 3D Slicer was chosen for image segmentation since it freely provides all the essential tools for both manual and automatic image segmentation.

Automatic segmentation methods are broadly classified as *thresholding*, *region growing*, *clustering* and *registration-based* methods (Aprovitola and Gallo, 2016; Hao, 2006). A brief description of these methods is provided in Table 2.3. Thresholding is driven by a greyscale intensity value in an image, based on which segments are classified into two groups, one above and the other below the threshold value (Hao, 2006). In region growing, a seed is placed in the region of interest in an image and the region growing algorithm expands the seed by identifying neighbouring areas of the same intensity. Similar to region growing, clustering uses a distance function to group similar pixels or image patches into one subset (Hao, 2006).

Registration-based methods use the concept of *image registration*, which is a transformation applied to all the points in an image/model to align with another image of the same anatomical part. It can be further classified into *deformable registration* and *atlas-based* approaches. Deformable registration requires a model which has a similar shape to the target model. On deformable models, algorithms, such as active contour, active shape and level set, are applied to generate segmentations of the new image (Aprovitola and

Gallo, 2016; Hao, 2006). In atlas-based methods, a previously segmented model of the same anatomical region is registered using non-rigid transformations to create segmented models of a new image. Further, local refinements are carried out using deformable model algorithms.

Table 2.3: Classification of automatic segmentation methods

Segmentation method	Medical image complexity	Level of previous knowledge required	Example usage
Thresholding	Simple	Low	Bone
Region growing	Simple	Low	Bone
Clustering	Simple	Low	Bone/Grey and white matter (Brain)
Deformable models	Complex	High	Any anatomical region
Atlas-based	Complex	High	Any anatomical region

Use of various combinations of previously described segmentation methods to develop knee 3D models is found in the literature. A brief review of those studies is provided in Table 2.4.

Table 2.4: A literature review on automatic segmentation methods to extract knee geometries

Study	Year	Segmented regions	Segmentation methods
Kapur et al.	1998	Femur and tibia bones femoral and tibial cartilages	Region growing (for bones), Feature detection and Bayesian classification (for cartilage)
Fripp et al.	2007	All knee cartilages and bones	Active shape models
Baldwin et al.	2010	All knee cartilages and patella bone	Integrated segmentation, mesh morphing
Swanson et al.	2010	Lateral meniscus	Semi-automated with threshold detection
Wang et al.	2013	Femur, tibia and respective cartilage	Patch-based segmentation without registration
Dam et al.	2015	Bones, menisci and cartilage	Multi-atlas registration, statistical approaches
Ahn et al.	2016	Femoral, tibial and and patellar cartilage	Level set, active contour model minimizing energies
Liukkonen et al.	2017	Femoral and tibial cartilage	Semi-automatic method based on radial intensity

Automatic segmentation of knee MRI is difficult because of the many different joint tissues which have similar intensity ranges, such as delineating the bone-cartilage interface poses an additional difficulty (Kapur et al., 1998; Sun et al., 2006). Custom algorithms are then required to achieve the desired segmentation results and are quite complicated to implement without appropriate programming knowledge.

Mesh Generation

Accurate representation of tissue geometries is crucial to obtain meaningful responses from an FE simulation. In an FE model, geometries take the form of meshes. A 3D finite element mesh can be broadly categorized as tetrahedral and hexahedral mesh (Grosland et al., 2009). Both kinds of elements have been used to model knee mechanics in the past (Kiapour et al., 2013; Liukkonen et al., 2017). A tetrahedral mesh consists of a cluster of tetrahedrons sharing their endpoints (nodes) and edges to represent a geometry, whereas hexahedrons or cubes are used instead in a hexahedral mesh (Figure 2.7). For a given mesh density, 4-10 times more tetrahedral elements are required to achieve similar results, which increases the computational cost (Shivanna et al., 2010). Besides, lower-order tetrahedral elements (4-noded) tend to be stiff and higher-order elements (10-noded) tend to turn inside out under high deformations, which has made hexahedral meshing a more reliable and effective approach.

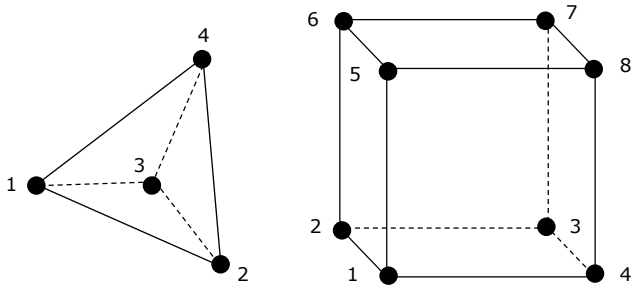

Figure 2.7: A tetrahedral (left) and a hexahedral (right) element

Most of the commercial mesh generating software is equipped to create accurate tetrahedral meshes of any irregular geometry. Likewise, the procedure to generate hexahedral meshes for simple geometries can be relatively straightforward to implement. However, obtaining hexahedral meshes of irregular geometries such as soft tissues can be a laborious and time-consuming task (Grosland et al., 2009). Researchers have often resorted to multi-block meshing technique to generate hexahedral meshes of irregular geometries. In the multi-block approach, an initial bounding box (or a 'block') is created around the structure and then sub-divided into several smaller blocks. These smaller blocks may be re-positioned to represent the geometry roughly. Mesh generation is achieved by using the closest-point algorithm to morph the vertices of the blocks on to the input geometry (Grosland et al., 2009).

While meshing irregular biological tissues, it is essential to maintain the quality of the mesh at acceptable standards adopted in the literature. Yang (2018) stated the minimum values of the following mesh quality metrics to be maintained in hexahedral meshes of biological tissues. The first among them is the *Jacobian*, which represents the volume ratio of an element in the mesh to an ideally shaped element (for example, a cube in a hexahedral mesh). Elements having Jacobian values close to unity are desirable, but elements with Jacobian greater than 0.6 are considered of acceptable quality in biological tissues. Generally, acceptable values of the *internal angle* between two faces inside a hexahedral element have to be maintained between 45° and 135° (an ideal element has an angle of 90°). Another metric, which quantifies the deviation from an ideally shaped element, is *warpage*. Warpage angle is the measure of the out-of-plane inclination of a node with respect to three other nodes on a surface in a hexahedral element. Elements with warpage angles of less than 15° are considered adequate. Finally, the *aspect ratio*, which is the ratio of the longest edge to the shortest edge in an element has to be less than three for an optimum element.

Multi-block meshing can be used to obtain high-quality hexahedral meshes, and the mesh density can be varied by controlling the number of sub-divided blocks. Applications such as ANSYS ICEM CFD (ANSYS, Canonsburg, PA, USA), IA-FEMesh (MIMIX, The University of Iowa, IA, USA), TrueGrid (XYZ Scientific Applications Inc., Pleasant Hill, CA, USA) offer multi-block meshing capabilities and are often used for mesh generation of soft tissues. ICEM CFD and TrueGrid are proprietary and have been used to create hexahedral meshes of the femur (Schonning et al., 2009), normal and scoliosis-affected vertebral geometries (Hadagali et al., 2018), and also to mesh the human brain (Mao et al., 2013).

IA-FEMesh is an open-source application, which offers similar features as the other applications. Shivanna et al. (2010) demonstrated the capabilities of IA-FEMesh by meshing many tissue geometries (brain, phalanx, femur and femoral cartilage) and implant devices (wrist implants, total knee replacement) and Kiapour et al. (2013) built a full lower limb FE model in IA-FEMesh.

Another study by Rodriguez-Vila et al. (2017) developed a fully automatic methodology to generate hexahedral meshes of the knee soft tissues implemented in MATLAB (The MathWorks Inc., Natick, Massachusetts, USA). The software (MATLAB program) reads the geometry of the femoral cartilage, tibial cartilages and the menisci in stereolithography (STL) format and generates an initial low-resolution mesh using a custom sweeping algorithm followed by smoothing using a Laplacian filter in the next step. Further, the smoothed mesh is projected onto the original geometry to generate an initial coarse mesh. The coarse mesh is then subdivided into more elements, and the element quality is verified. If the element quality fails to meet specific quality criteria, the smoothing process is repeated, which then moves the nodes in the elements within the geometry bounds, until the quality criteria are satisfied.

2.4.2 Computational Models of Jump Landing

Computational models have been previously developed to understand ACL injury mechanics during jump landing events. Shin et al. (2007) developed a subject-specific multibody dynamics model to simulate a jump landing. They evaluated the effect of deceleration forces on ACL strain during run-to-stop single-leg landing. The inputs to the model were from the *in-vitro* experiments of Withrow et al. (2006), where an impact force is applied on top of the femur bone attachment. Quadriceps, hamstrings and gastrocnemius muscle force pretensions were applied at the start to maintain the knee angle at 25°. After the impact force was applied, muscle forces naturally developed in the bundles. Except for verifying the model inputs against the experiment, no other validation study was carried out. The relative ACL strain in the simulation (2.1 %) compared well with the experimental results (2.5 %) and the time to peak ACL strain was within 25 ms of each other. Also, the study proceeded to test another hypothesis that during landing, posterior forces on the tibia exist due to deceleration forces, which protects the ACL. Consequently, the study found that ACL strain decreases with the increase in posterior forces on the tibia.

To test the hypothesis that the quadriceps force is not a contributor to ACL injury, Domire et al. (2011) simulated a jump using a mathematical model of the quadriceps muscle. The authors questioned if the quadriceps force values ($\sim$ 4500 N) during jump landing from earlier experimental studies could be as high as reported and reviewed it using a simple simulation model. They concluded that even at the highest levels of pre-activation of quadriceps forces, the peak values ($\sim$ 2000 N) would not reach half of what had been previously reported and thus stated that the peak quadriceps force alone cannot be a primary contributor to an ACL injury.

Kiapour et al. (2013) also simulated a jump landing on a subject-specific, validated FE model. The model was validated by comparing tibiofemoral kinematics under quasi-static and dynamic loading to a wide range of cadaveric studies. They also simulated a bipedal landing from the *in-vitro* experiments on the Ohio State University simulator. In the experiment, the GRF during landing was simulated by dropping half bodyweight (350 N) on the underside of the foot from 30 cm height while the quadriceps and hamstring forces were maintained at 1200 N and 800 N and the same conditions were replicated in the FE model. They found an increase in ATT, knee valgus, internal tibial rotation, and ACL and MCL strains after the impact. Peak ACL strain was found to be 5.2 %. In addition, the simulation was repeated with 134 N of anterior tibial force and found that the parameters mentioned above increased with the peak ACL strain at 7.1 %.

A common theme among these models was that the experiments on which the models were based on did not have dynamically varying muscle forces but were pre-set values. Therefore, they did not adequately represent the physiological loading conditions during jump landing (Bakker et al., 2016). The above limitation was addressed in the study by Polak (2019), where dynamic muscle forces obtained from Bakker et al. (2016) were used to simulate jump landings on a computational FE model of a 50^{th} percentile male. It was

found that the peak relative ACL strains were 4.2 % and 13.9 % occurring at 60 ms after ground contact, in the simulation of two different jump landing profiles. Table 2.5 shows a summary of computational knee models simulating jump landing activity.

Table 2.5: A literature review on computational knee models simulating jump landing

Study	Year	Type of model	Model validation method	Peak ACL strain (%)
Shin et al.	2007	Subject-specific multibody dynamics model	None	2.1
Domire et al.	2011	Mathematical model to estimate quadriceps forces	None	NA
Kiapour et al.	2013	Subject-specific FE model	Against experimentally measured tibiofemoral kinematics	5.2
Polak	2019	FE model of a 50^{th} percentile male	Simulated on a validated GHBMC lower limb model	9.1

Due to the disparity in the anatomical features of each individual, ACL injury mechanics can vary significantly between subjects. In this regard, subject-specific models can be powerful tools in predicting an individual's risk of ACL injury in specific activities. However, simulation of jump landing activity on a validated subject-specific FE model, with dynamic physiological loading conditions, is a critical gap in the current literature. Addressing this gap can prove to be an inexpensive alternative to recreating dynamic knee loading scenarios on cadaveric specimens and can also provide invaluable data to understand subject-specific injury mechanics due to the intrinsic anatomical factors.

2.4.3 Modelling Ligament Behaviour

The choice of material properties for the knee ligaments influences the overall joint kinematics, especially in dynamic simulations such as jump landing. Modelling ligament characteristics is complicated, given the distinctive behaviour of ligaments under loading (Galbusera et al., 2014). Although experimental tests can extract ligament properties, this requires complex experimental setups and robust instrumentation. Due to these reasons, most studies use the material properties of ligaments from previously published data.

Mechanical Properties

Mechanical behaviour of the ACL is characterized by performing uniaxial tensile tests, most commonly in the bone-ligament-bone configuration. The force versus displacement or

stress-strain relationship of the ACL is non-linear, like any other ligament, and shows three distinct regions: the non-linear toe region, the linear region and the failure region (Figure 2.8). Before the application of the load, the ligament fibres are slack and not aligned in any particular direction, and they gradually start to align in the loading direction, which corresponds to the initial toe region. Upon increasing the load, the fibres, now fully aligned in the loading direction, exhibit linear behaviour (linear region). Failure occurs when the collagen fibres rupture and the ACL tears. Tensile properties of ACL has been characterized by previous studies (Butler et al., 1986; Chandrashekar et al., 2006; Noyes and Grood, 1976; Hollis et al., 1991). Figure 2.8 shows the ACL behaviour reported by a more recent study, Chandrashekar (2005) where uniaxial tensile tests on the ACL of ten male and ten female cadaver subjects were performed at a strain rate of 100 %/s, along the longitudinal axis.

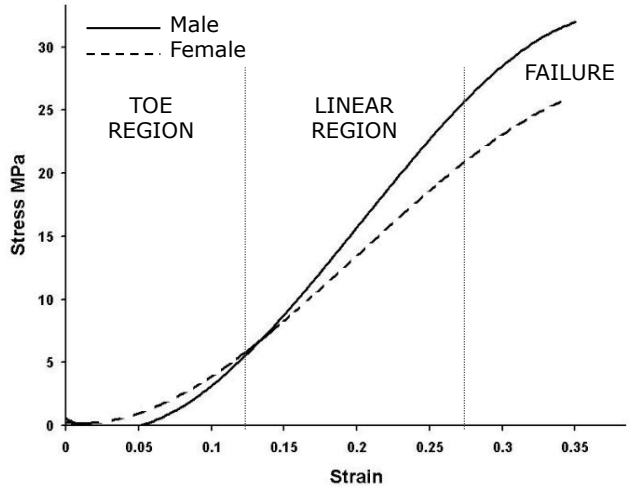

Figure 2.8: Stress-strain relationship of male and female ACL under uniaxial tension (adapted from Chandrashekar (2005))

Modelling Knee Ligaments

Previously, in computational models, ligaments have been represented as one, two and three-dimensional (or continuum) models. Synonymous with the name, each model has the respective number of degrees of freedom.

1D models deform only in one direction, along the axis of the element. They are modelled as individual bundles at approximately the same attachment location of the actual ligament (Galbusera et al., 2014). From the early experimental work on ligament behaviour by Butler et al. (1986) and Trent et al. (1976), Blankevoort et al. (1991) developed a mathematical model to describe the force versus displacement behaviour of the major ligaments in the knee joint (ACL, PCL, MCL and LCL) and the capsular ligament. The mathematical model is expressed as:

$$f = \begin{cases} \frac{1}{4}k\frac{\varepsilon^2}{\varepsilon_l}, & 0 \leq \varepsilon \leq 2\varepsilon_l \\ k(\varepsilon - \varepsilon_l), & \varepsilon > 2\varepsilon_l \\ 0, & \varepsilon < 0 \end{cases}$$

f is the ligament force, ε is the strain in the ligament and k is the stiffness parameter. The above equation is analogous to the equation of a linear spring, $f = kx$ (where k is the spring stiffness and x is the spring displacement). A quadratic equation in strain is used to describe the initial toe region (or non-linear region) and a linear equation in strain to represent the linear region of the ligament behaviour (Figure 2.8). The linear strain limit, ε_l, controls the transition from initial non-linear or toe region to the linear region. The fact that a ligament does not resist compressive or shear loads is taken care in the mathematical model by setting force to be zero for compressive strains. By varying the stiffness parameter, k and the linear strain limit, ε_l, force versus displacement behaviour of all the ligaments can be generated. This requires the zero-load length L_0 of the ligament which can be obtained from the equation (Blankevoort et al., 1991):

$$L_0 = \frac{L_r}{(\varepsilon_r + 1)}$$

L_r is the length of the ligament bundle at the reference position, which usually is at extension and can be measured from the MRI scans or through digitization of anatomic co-ordinates. ε_r is the strain in the ligament bundle at the reference length L_r, which is also prescribed for each ligament bundle in Blankevoort et al. (1991). Several authors have used different versions of this mathematical model, but the underlying concept remained the same (Galbusera et al., 2014). However, there is no general agreement on the pre-strain values of ACL (at extension) among these studies. It ranges from no pre-strain (Abdel-Rahman and Hefzy, 1998) to 16 % pre-strain (Amiri and Wilson, 2012) (Table 2.6). These values were chosen based on either experimental studies from other literature in some cases or based on their own *in-vitro* and optimization studies. Despite this variability, Beidokhti et al. (2017) evaluated 1D and 3D continuum models of ACL and concluded that 1D models produce quick and satisfactory results if the kinematic output from the simulation is the main objective. Table 2.6 shows a brief review of studies that modelled ligaments as 1D elements.

While 1D representations of a ligament are convenient, 2D and 3D continuum models enable detailed and realistic representations of the ligament behaviour. With continuum models, wrapping of the ligament bundles with bones, contact with other ligaments and with the bones can be simulated (Galbusera et al., 2014). Some studies have considered ligaments to be simple hyperelastic models such as neo-Hookean (Mootanah et al., 2014; Beidokhti et al., 2017) while others have implemented custom hyperelastic material models such as Veronda–Westmann (Song et al., 2004) to describe their behaviour (Galbusera

et al., 2014). Further, continuum models also allow modelling of true anisotropic nature of the ligaments using complex constitutive models such as Holzapfel-Grasser-Ogden (HGO), implemented by both and Kiapour et al. (2013) and Westermann et al. (2013).

Table 2.6: A literature review on 1D non-linear spring models for ACL

Study	Year	ACL bundles	Stiffness	Pre-strain (%)
Abdel-Rahman and Hefzy	1998	AM	83.15 N/mm^2 (toe region) 22.48 N/mm (linear region)	0
		PL	83.15 N/mm^2 (toe region) 26.27 N/mm (linear region)	5.1
Zielinska and Haut Donahue	2006	AM		6
		PL	Stiffness parameter: 5000 N	10
Shin et al.	2007	AM	108 N/mm	2
		PL		2
Amiri and Wilson	2012	AM		16
		IM	Stiffness parameter: 5000 N	10
		PL		10
Harris et al.	2016	AM	(50−106) N/mm	−1.5 to 10
		PL	(51−108) N/mm	−1.5 to 10

2.5 Summary of Previous Research

Cassidy et al. (2013) developed a workflow to measure ACL strain during single-leg jump landing, which involved *in-vivo* motion capture, generation of muscle forces from a musculoskeletal model using the motion capture data and measurement of ACL strain *in-vitro*. In the study of Bakker et al. (2016), the same approach was followed to measure the ACL strain of recreational athletes during jump landing wherein 3D kinematics (body marker data) and GRFs (using a force plate), were obtained from 10 different participants. GRF data was input into a musculoskeletal model in *OpenSim* (Stanford University) to obtain muscle forces and hip and ankle kinematics. Further, *in-vitro* jump landing simulations were carried out on five cadaver specimens (3 male, 2 female, average age of 47.2 years) on the University of Waterloo Dynamic Knee Simulator (DKS) and anteromedial ACL strain was recorded using a DVRT.

Based on the workflow established by Cassidy et al. (2013) and Bakker et al. (2016), additional *in-vitro* jump landing experiments were carried out by Polak (2019) on three cadaver specimens (1 male, 2 female, average age of 47.6 years). In the same study, ACL strain was calculated by simulating jump landing activity on the 50$^{\text{th}}$ percentile male, a

lower extremity FE model of GHBMC. A DVRT was mounted on the anteromedial bundle of the ACL to measure the relative strain during the experiment (Figure 2.9).

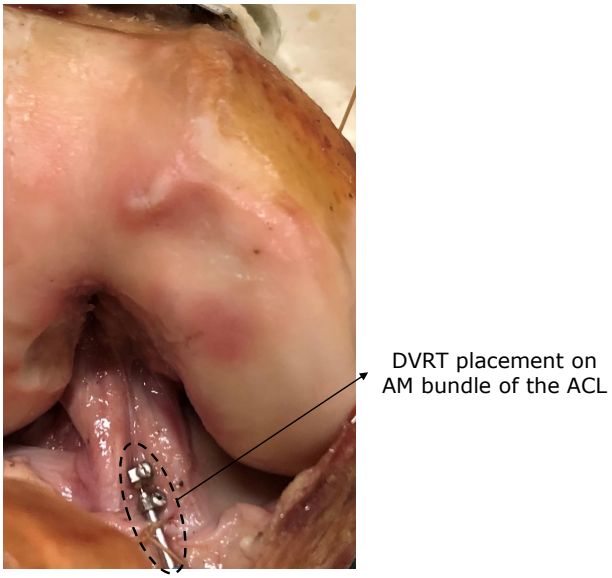

Figure 2.9: DVRT placed on the ACL to record displacement in the experiments (adapted from Polak (2019))

The FE model developed for the current study is the subject-specific model of one of the cadaver specimens of the *in-vitro* study of Polak (2019). Figure 2.10 shows a brief background of single-leg jump landing studies.

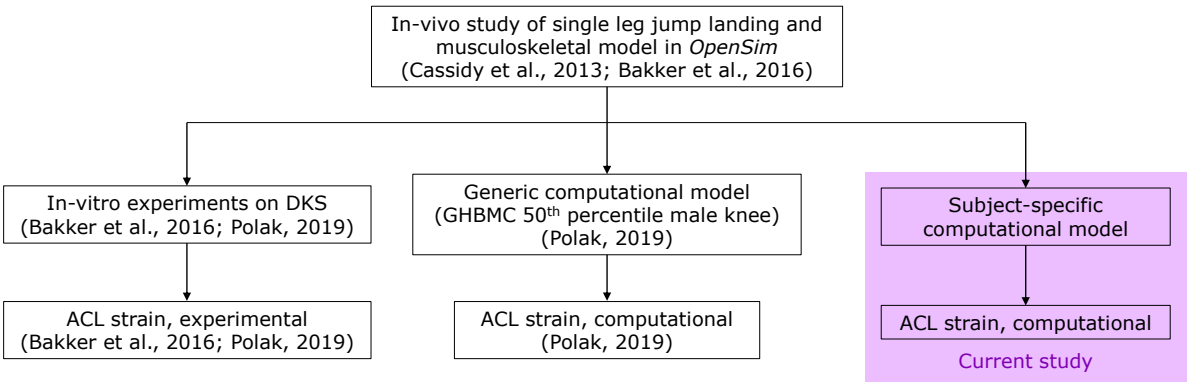

Figure 2.10: Previous and current research on single-leg jump landing (conducted at the University of Waterloo)

2.6 Hypothesis

The current study complements the previous work carried out by Bakker et al. (2016) and Polak (2019) by including a subject-specific FE model, of a cadaver specimen from the experimental work of Polak (2019)'s study. Based on this approach, it is hypothesized that:

1. The ACL strain trends in jump landing simulations of seven participant profiles (P1 to P7) will be similar to the experimental results of Bakker et al. (2016)
2. Peak ACL strains of the jump landing simulations would occur at approximately the same time as the experimental peak strains of Bakker et al. (2016)
3. Posterior medial meniscus strain trends during half muscle force jump simulations will correlate with the experimental results of Polak (2019)

Chapter 3

Methodology

The FE model developed for the current study is the subject-specific model based on one of the cadaver specimens of the *in-vitro* study of Polak (2019). Figure 3.1 shows an overview of the steps performed to generate the knee joint FE model.

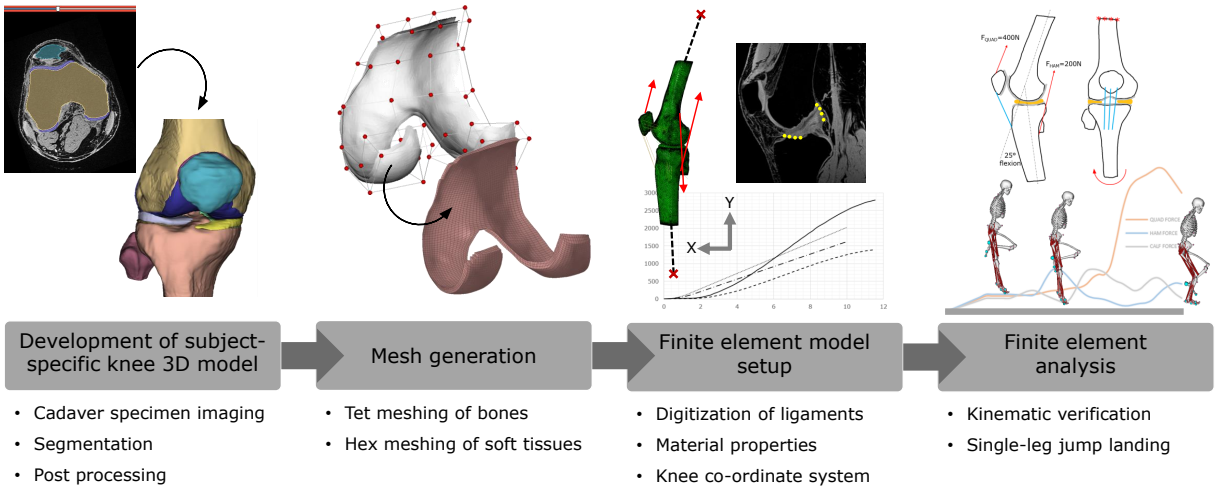

Figure 3.1: Overview of the procedure to develop and validate a subject-specific FE model

3.1 Development of Subject-Specific Finite Element Model

3.1.1 Definition of Tissue Geometries Using Medical Imaging

A fresh frozen cadaver knee specimen from the *in-vitro* study of Polak (2019) was chosen for the development of a subject-specific FE model (labelled as Knee 1 in Polak (2019)).

The specimen contained the entire knee joint, all of its musculature and the soft tissues, sectioned eight inches above and below the joint. The specimen information is provided in Table 3.1. The anthropometrics of this individual (height and body mass) were close to a 50^{th} percentile U.S. male (Gayzik et al., 2011).

Table 3.1: Tissue donor information

Extremity	Sex	Age (years)	Height (cm)	Body mass (kg)
Right	Male	49	178	77

The specimen was frozen in an extended position and then a cast was built around it to preserve the shape of the knee joint in extension (Figure 3.2A). The cast was then carefully cut open and separated from the specimen and stored. A day before the scanning, the specimen was defrosted overnight (Figure 3.2B). The defrosted specimen was secured in the previously built cast for the imaging procedure.

Figure 3.2: Cadaver specimen, PK1
Cast in extension when frozen (A) and the same in a defrosted state (B)

Cadaver Imaging

3D CT (Toshiba Aquilion CT scanner, Zoetermeer, Netherlands) and MRI (Seimens MAGNETOM Prisma 3.0T, Erlangen, Germany) scan of the cadaver specimen were obtained at Sunnybrook Medical Center, Toronto, ON, Canada. On the MRI machine, the knee specimen was placed in a knee coil (Tx/Rx Knee 15 Flare Coil) to improve image quality.

MRI was obtained in three commonly acquired sequences, T1, T2 and Proton Density (PD), for knee tissue segmentation (Aprovitola and Gallo, 2016). Sagittal plane images of the scans are shown in Figure 3.3, and the details of the scans are available in Table 3.2.

Table 3.2: Details of the MRI scans acquired for the current study

Sequence	Features	Resolution	Number of slices	Slice thickness (mm)
T1	Bone appears dark, good overall tissue visibility	512 × 512	224	0.5
T2	Bone appears grey, good muscle visibility	512 × 512	204	0.5
PD	Good cartilage-bone interface, meniscus and ligament visibility	512 × 512	204	0.5

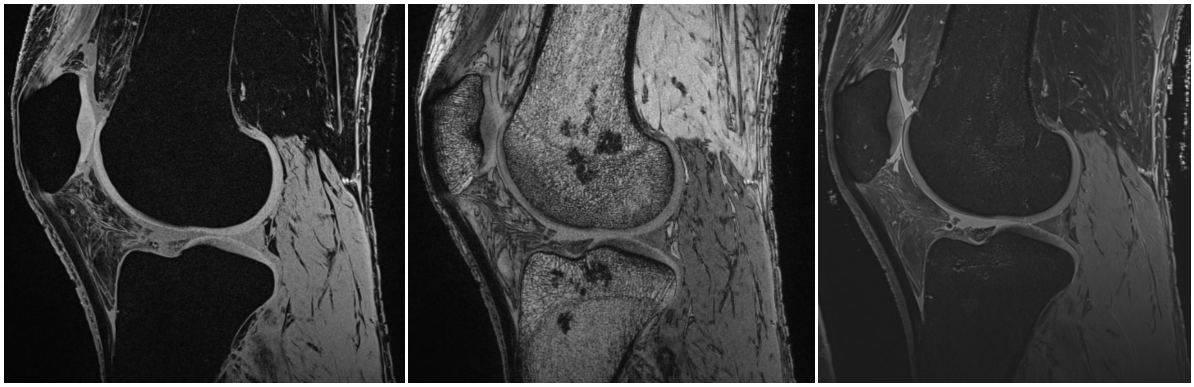

Figure 3.3: MRI sequences obtained for the current study

Segmentation

3D Slicer software (version 4) was used to generate the 3D model of the knee joint through a process called segmentation. Two segmentation methods, *automatic* and *manual* segmentation were used to segment the CT and MRI scans. An automatic segmentation method called *thresholding*, an intensity-based segmentation method was used to generate models of the bones from the CT scans quickly (Fripp et al., 2007). The image intensity range of the bones was input in the *thresholding effect* tool in the *segment editor* module of 3D Slicer to define segmentation boundaries.

Manual segmentation involved assigning a specific colour to the region of interest using various tools (paint, erase, scissors, level tracing) available in the *segment editor* module

of 3D Slicer. A segmented model of the knee joint, SPL 2015 Sep, was used as a reference during segmentation. This dataset was crucial in understanding the locations of soft tissues and bone-cartilage interfaces in the scans. Figure 3.4 shows the process of segmentation of the MRI scans in 3D Slicer.

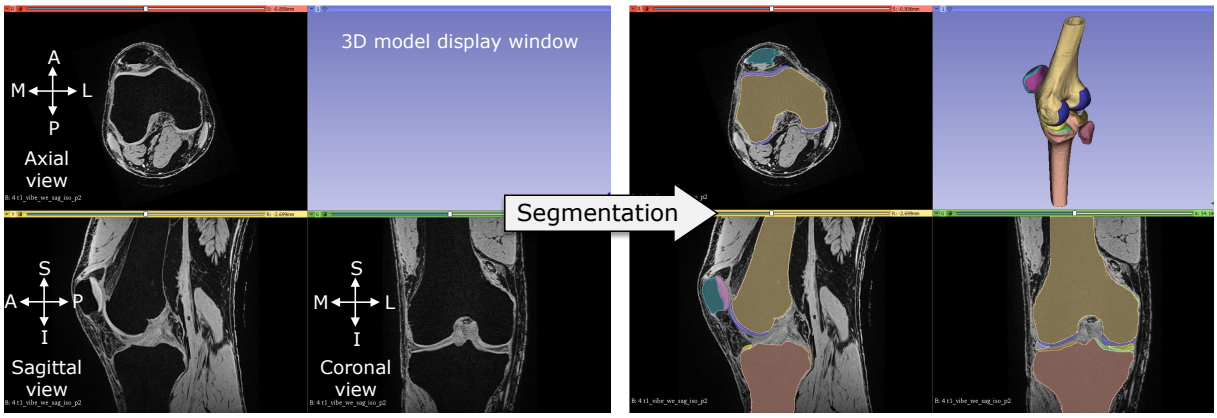

Figure 3.4: Segmentation process of bones and soft tissues in 3D Slicer
MRI scans in 3D Slicer software in axial, sagittal and coronal planes (left). Segmented scans after manual and automatic segmentation procedures, along with the completed model (right)

The geometry obtained from 3D Slicer was coarse and had jagged edges called as staircase artefacts, common with segmentation. Therefore, before meshing, smoothing of the surfaces and trimming of the boundaries of the geometries was performed in SolidWorks 2018 (Dassault Systèmes, Waltham, MA, USA) using the *Surface Wizard* and *Curve Wizard* functions. During smoothing, care was taken not to distort the original geometrical shape or contours of tissues but to remove only the surface irregularities (Figure 3.5). Figure 3.6 shows the segmented models of all the soft tissues in the knee joint after adequate smoothing in SolidWorks.

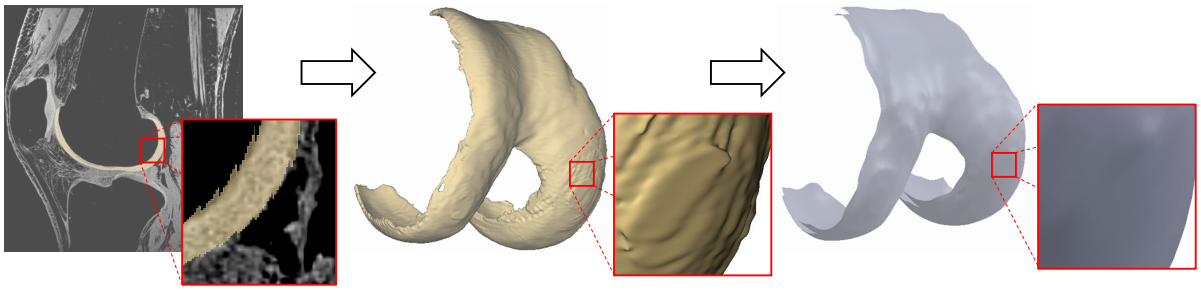

Figure 3.5: Smoothing of femoral cartilage geometry in SolidWorks

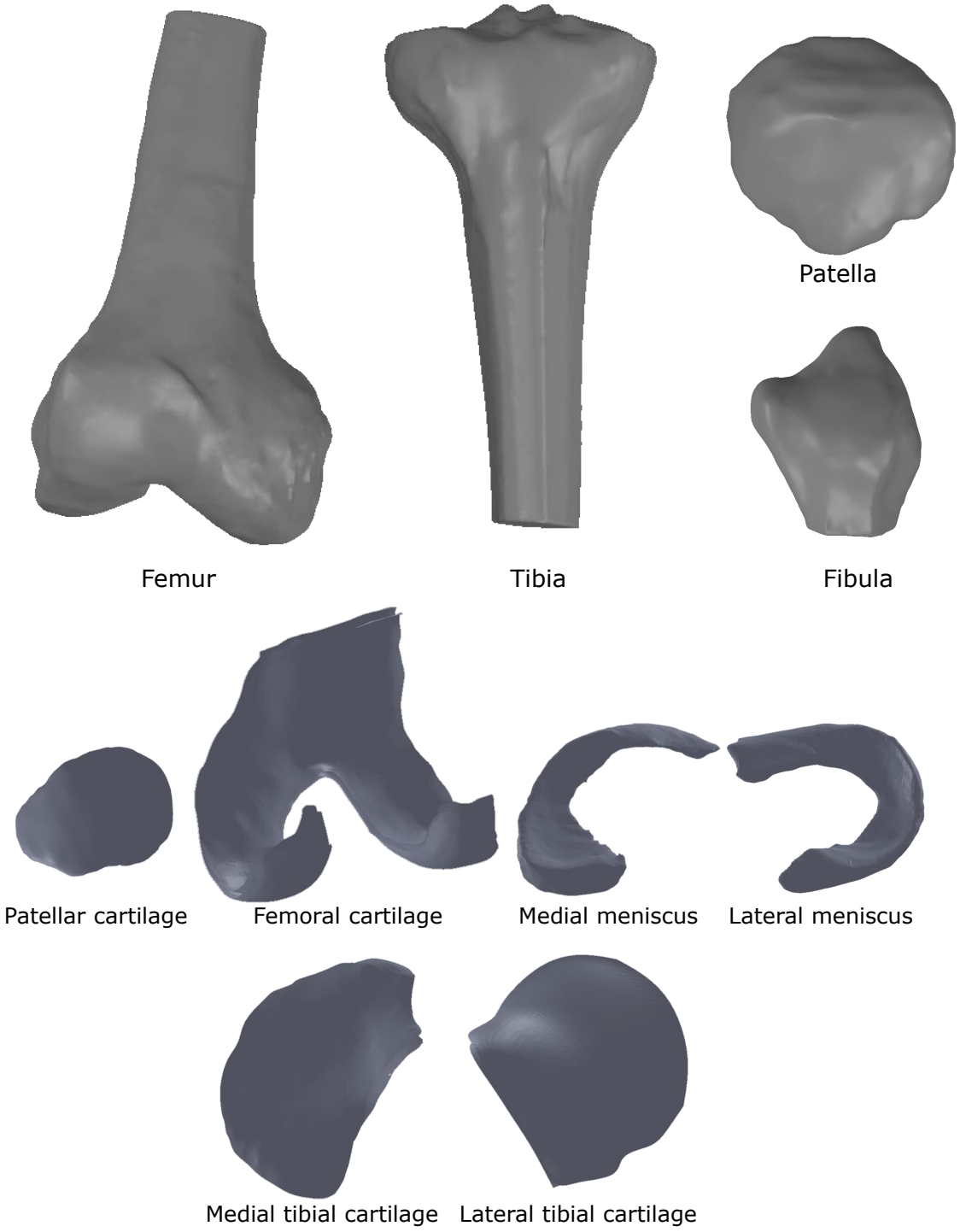

Figure 3.6: Segmented models of bones and soft tissues after smoothing in SolidWorks

3.1.2 Digitization of Ligament Insertion Sites

The ligaments were positioned accurately in the FE model by recording the ligament attachment sites on the cadaver specimen, using a spatial coordinate measuring device, *MicroScribe-G2X*^{TM} (Immersion Corporation, USA), with a reported accuracy of 0.23 mm (Figure 3.7).

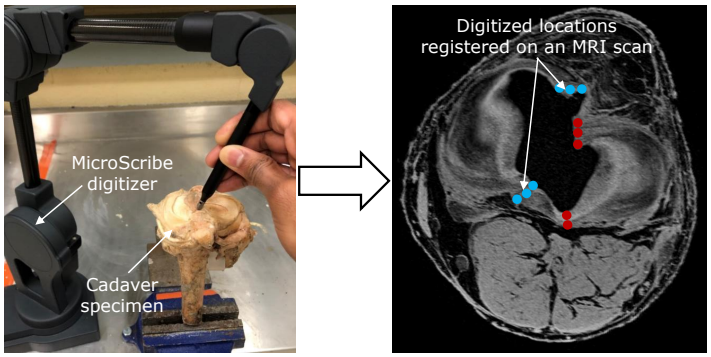

Figure 3.7: MircoScribe digitizer and digitization procedure

The attachment sites of the ligament were digitized both on the femur and tibia bones. To access the joint space during digitization, the femur and the tibia bones were separated by cutting the cruciate and the collateral ligaments approximately at their mid-lengths. The bones were then mounted on a platform using the threaded rods, which were already screwed in at the end of the bones, required for the jump landing experiment on the DKS.

To map the attachment sites of the ligaments onto the segmented model of the knee joint, the location of the bony landmarks of the femur and the tibia were recorded first. The list of bony landmarks was obtained from Subburaj et al. (2009) (Figure 3.8). Next, the attachment sites of the ACL, PCL, and MCL on the tibia and the femur were recorded. LCL has an attachment site on the fibula, which was also digitized. In addition, the meniscal attachment sites on the tibial plateau were also digitized.

The position data of the attachment sites from the digitizer coordinate system was rigidly registered (or aligned) onto the 3D model (generated via segmentation) using the *Transform* tool available in 3D Slicer. First, the locations of the bony landmarks to their respective locations in the model were aligned, which in turn translated the attachment sites to their respective locations on the model. The transformed coordinate data of the ligaments, now in the knee joint co-ordinate system was obtained and transferred to Abaqus CAE 2018 (Dassault Systèmes, Johnston, RI, USA), a commercial finite element package which includes a pre-processor, solver and post-processor for an FE simulation. Here, the digitized ligament locations were used to construct non-linear spring elements, as described in the following section. An anatomy textbook (Moore and Dalley, 2013) was also referred to verify the locations of the bony landmarks and the ligament attachment sites. Figure 3.9 shows the digitization setup and steps described above.

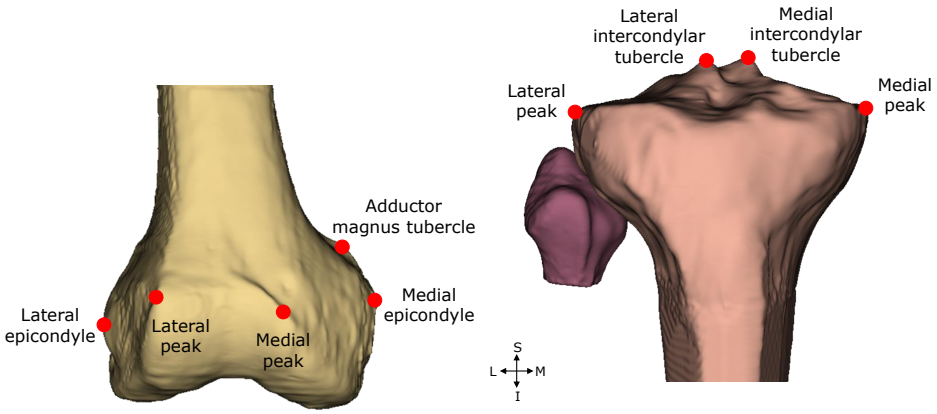

Figure 3.8: Bony landmarks on the femur (left) and tibia (right) (adapted from Subburaj et al. (2009))

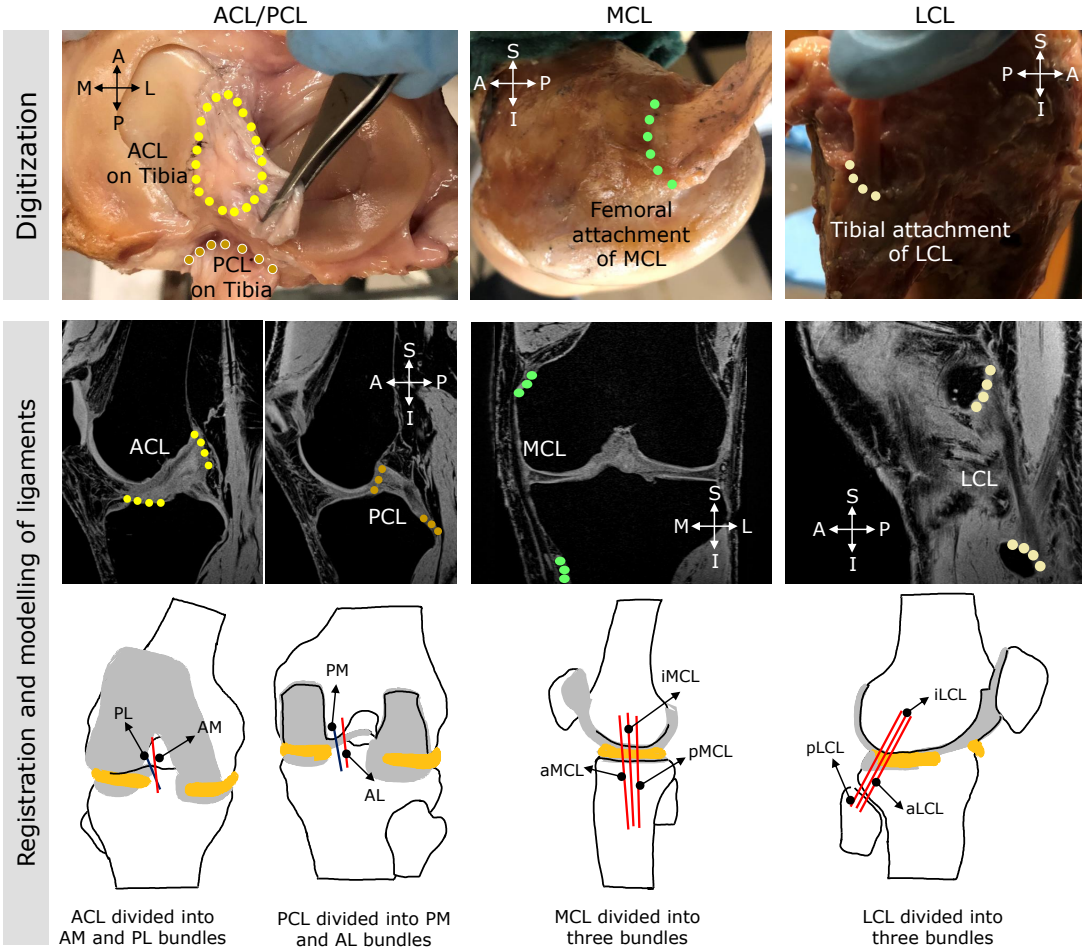

Figure 3.9: Procedure followed to digitize the ligament insertion sites in the current study

3.1.3 Tibial Slope

Higher posterior tibial slopes have been shown to increase the risk of ACL injury due to increase in ATT (Giffin et al., 2004; McLean et al., 2011). Therefore medial and lateral tibial slopes were measured from the CT scans following the procedure described in Hashemi et al. (2008) and described in Figure 3.10. Medial and lateral tibial slopes were found to be 8.5° and 9.0° respectively.

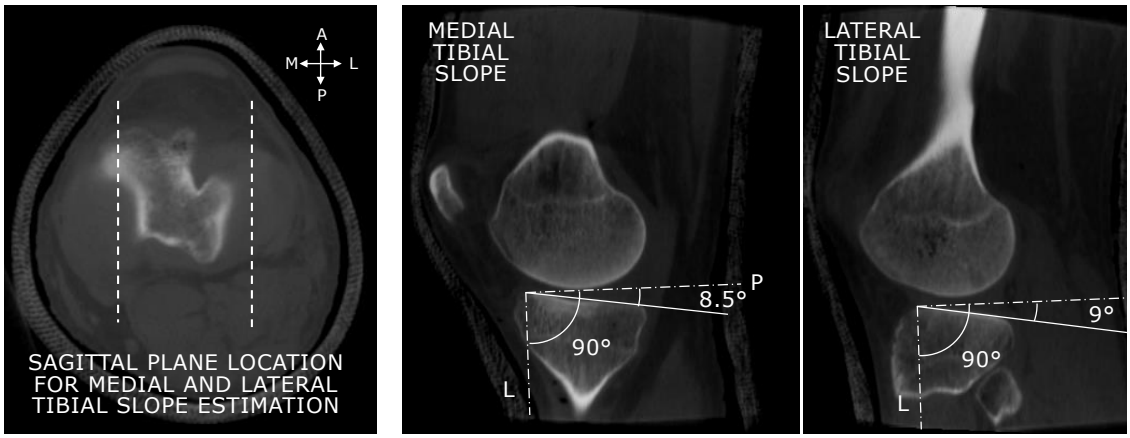

Figure 3.10: Medial and lateral tibial slopes measured on the CT scan
L is the longitudinal tibial axis and P is perpendicular to L. Solid lines coincide with the tibial plateau for slope measurement

3.1.4 Meshing of the Segmented Geometries

Two element types were used to mesh the segmented models. Meshing strategy depended on the definition of each tissue component in the FE model. Bones have higher stiffness compared to other soft tissues and therefore were assigned tetrahedral elements, whereas the other soft tissues were meshed with hexahedral elements.

The extracted geometries of cartilage and menisci were meshed with 8-node hexahedral elements. Meshes of the menisci were automatically generated from a piece of software designed to mesh knee soft tissues, whereas the meshes of the cartilage were generated manually using a multi-block meshing procedure in IA-FEMesh. The bones of the knee joint were meshed with tetrahedral elements in HyperMesh (Altair Engineering, Inc., Troy MI, USA).

Hexahedral Meshing of the Menisci

The MATLAB software library developed by Rodriguez-Vila et al. (2017) was used to mesh the menisci and tibiofemoral cartilages of the knee joint. Hence, the smoothed models of

the soft tissues from the previous step, namely, femoral, tibial cartilages and the menisci were input to the software in STL format to generate hexahedral elements with 8 nodes (Figure 3.11).

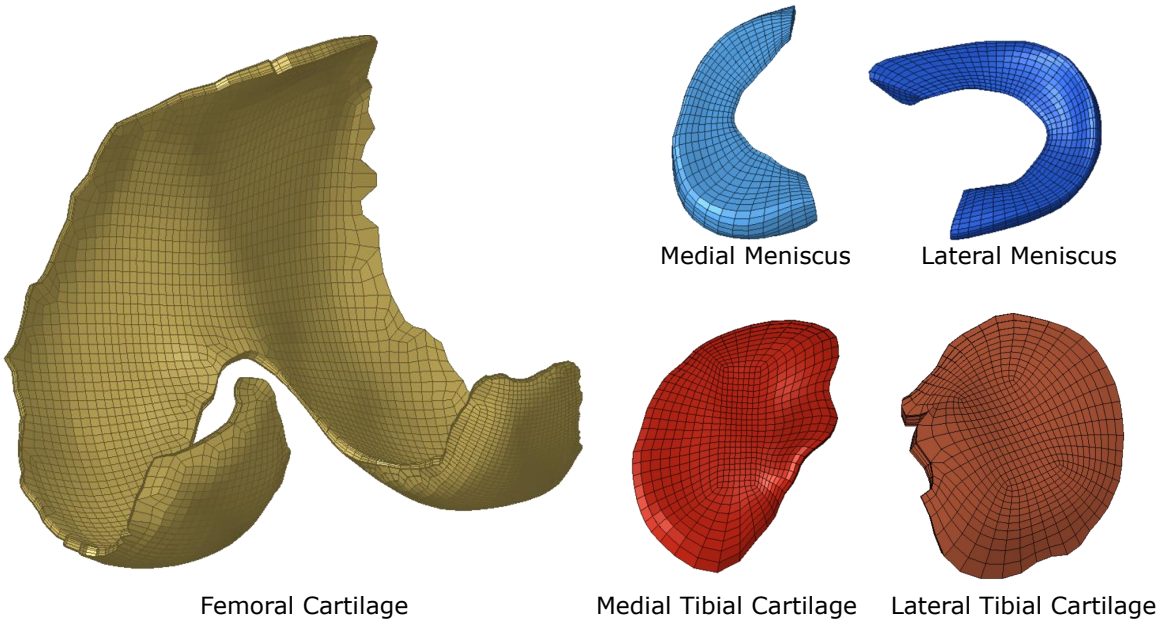

Figure 3.11: Hexahedral mesh output of the knee soft tissues (obtained using the software by Rodriguez-Vila et al. (2017))

Hexahedral Meshing of the Cartilage

The software by Rodriguez-Vila et al. (2017) was also capable of generating cartilage meshes quickly, similar to the menisci (Figure 3.11). Although using the software requires minimal manual effort, (mesh generation time for all structures is around 3 minutes) to generate good quality hexahedral meshes, the cartilage meshes obtained from this procedure were not used in the knee FE model and instead meshed manually using multi-block meshing approach in IA-FEMesh. The reason for choosing this alternate approach was that the software divides the cartilage thickness into six unequal layers to facilitate assigning depth-dependant cartilage material properties. Unequal division of cartilage generates two thin rows of elements (thickness 0.1mm), as shown in Figure 3.12. In dynamic simulations such as jump landing, thin elements would easily distort, creating problems in the model solution and output. Although it may be possible to tweak certain parameters in the MATLAB program to obtain a desirable mesh, it would have been time-consuming because the software is split into 24 individual MATLAB functions. Tweaking of parameters to get the desired number of mesh layers or mesh thickness would then involve carefully investigating how one change affects the other functions in the software. Hence, the multi-block meshing procedure was employed to generate cartilage meshes only. Moreover, patellar cartilage

had to be meshed manually since the software was not programmed for this structure, further justifying the selected approach.

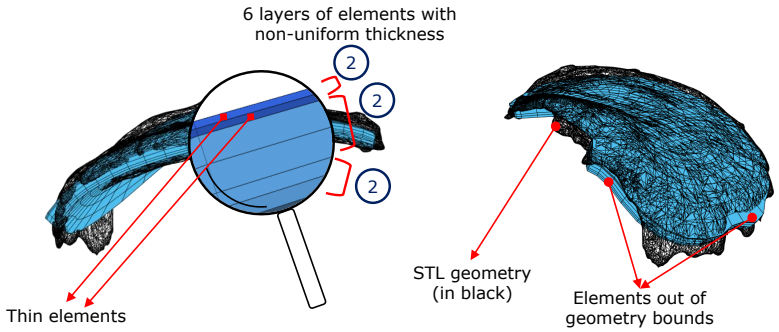

Figure 3.12: Thin elements in the lateral tibial cartilage mesh (obtained using the software by Rodriguez-Vila et al. (2017))

Figure 3.13 details the steps followed to create hexahedral meshes of the cartilage geometry, with femoral cartilage as an example. The process of multi-block meshing involved the creation of an initial bounding box around the STL file of the geometry (Step 1) and then subdividing the bounding box into smaller blocks. The vertices of the smaller blocks were adjusted to conform to the geometry of the object being meshed. More such subdivisions were created to capture the intricacies of the object and until the blocks satisfactorily represent the object (Step 2). Next, the number of divisions or the number of elements needed in the resulting mesh were chosen. Based on the user input, the application divides the blocks and generates a hexahedral mesh (Step 3). The mesh output can be directly exported as a .inp file to be read in Abaqus. The same process was followed to mesh the other cartilaginous structures.

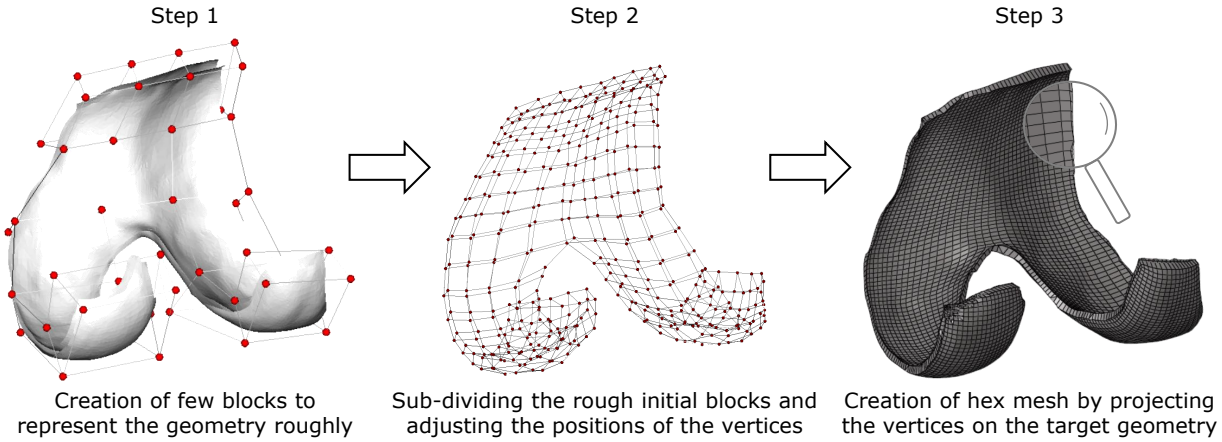

Figure 3.13: Multi-block meshing procedure in IA-FEMesh (shown for femoral cartilage)

The hexahedral meshes from IA-FEMesh were imported into HyperMesh 2017 (Altair Engineering, Inc., Troy, MI, USA) for further post-processing. In HyperMesh, the mesh output from IA-FEMesh was re-evaluated, and it also allowed the deletion of a few severely distorted elements on the periphery (one to two layers of distorted elements) of the cartilage structures, as shown in Figure 3.14. Mesh output of all the cartilages after post-processing in HyperMesh is shown in Figure 3.15.

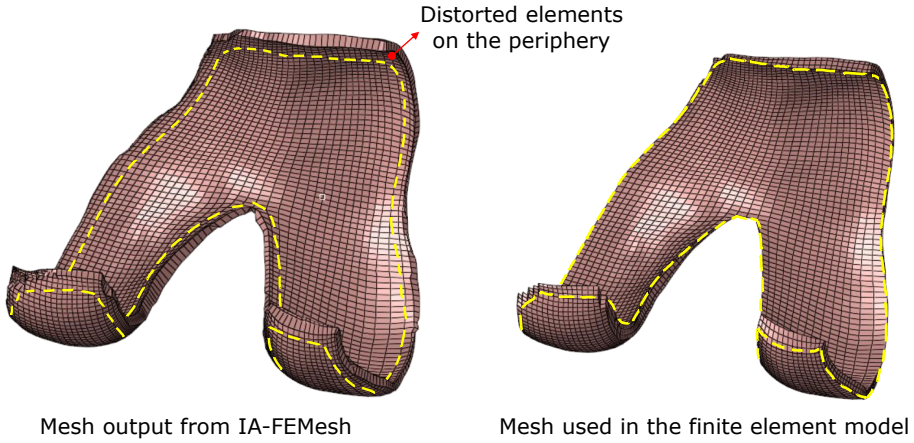

Figure 3.14: Deletion of excessively distorted boundary elements (shown for femoral cartilage)

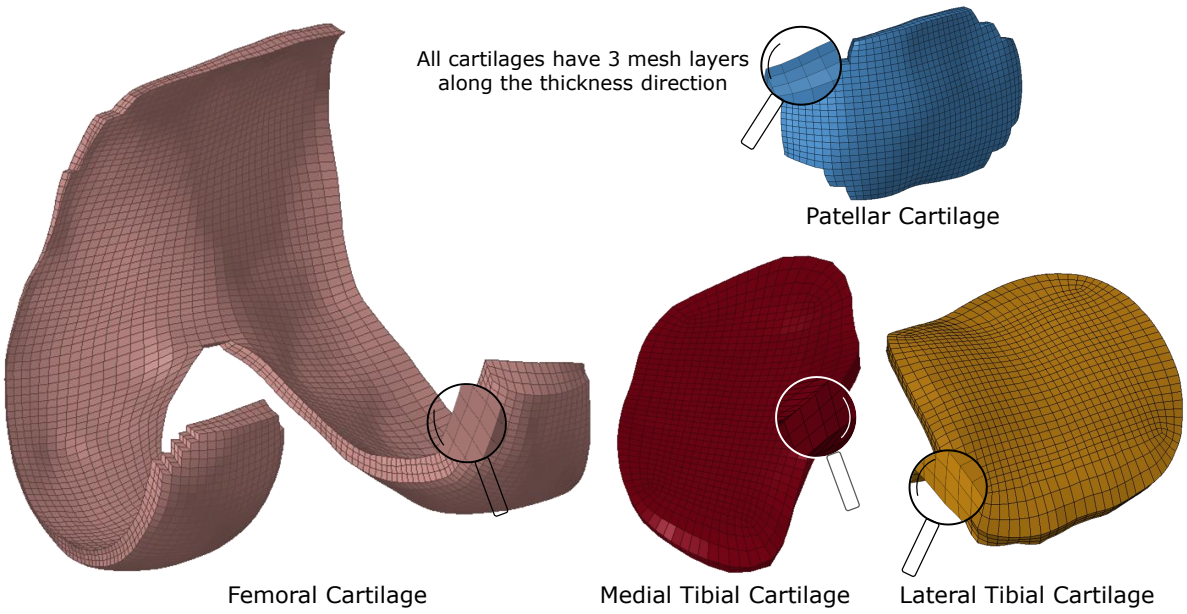

Figure 3.15: Hexahedral meshes of all cartilages after post-processing in HyperMesh

Tetrahedral Meshing of the Bones

The bones in the knee joint (femur, tibia, patella and fibula) were defined as rigid bodies in the FE model since the stiffness of bones is very high (Table 3.3) compared to the other soft tissues in the human body. Defining the bones as rigid bodies is a general practice in studies focussed on soft tissue behaviour. It also has a significant impact on the computational time since the elements in a rigid body do not undergo any deformation but only exhibit rigid body motions[1]. Therefore, bones were meshed with first-order tetrahedral elements in HyperMesh (Figure 3.16).

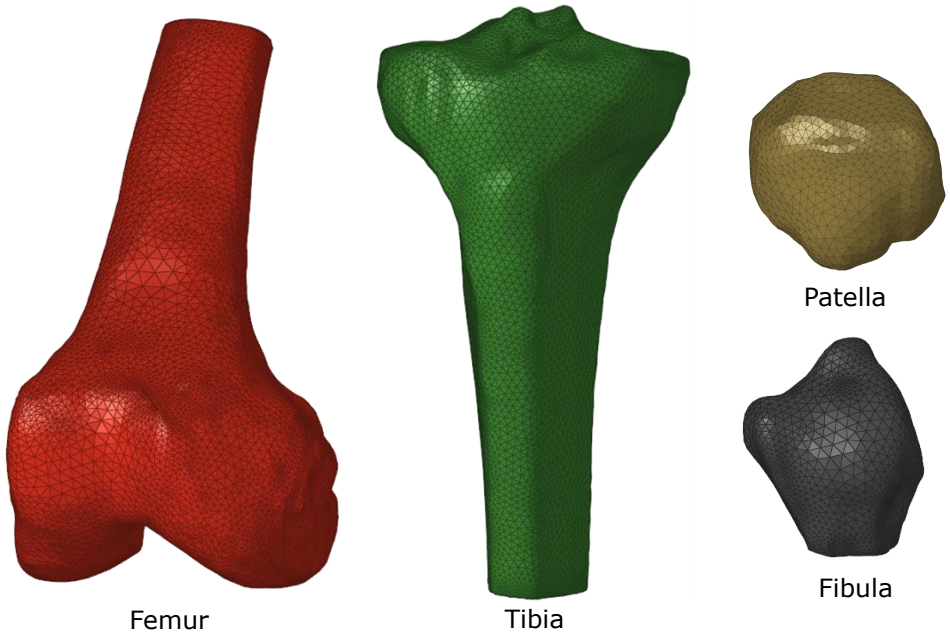

Figure 3.16: Tetrahedral meshes of the bones in the knee joint

3.1.5 Model Definition in Abaqus CAE

The individual hexahedral meshes of the soft tissues and the tetrahedral meshes of the bones were imported and assembled in Abaqus CAE, and suitable element type was chosen for each structure. Appropriate material properties were also assigned to both soft and hard tissues. Also, several constraints and contact definitions were assigned to enable proper interactions between the tissues. Ligament attachment locations were derived from the digitization exercise, and their properties were assigned based on a mathematical model. Following sections explain the setup of the FE model in detail.

[1] Abaqus 6.14 online documentation, section 2.4.1

Element Type

All the soft tissues of the knee joint were meshed with 8-node hexahedral elements[2], and hence C3D8R element type (C-Continuum, 3D-3 Dimensional, 8-number of nodes in the element, R-Reduced integration) were assigned (Figure 3.17). C3D8R elements are computationally more efficient than the fully integrated (C3D8) elements. The disadvantage with such elements is that they suffer excessive distortions due to the single integration point available in the element for stress/strain calculations[3]. At the integration point, at times, strains can become zero leading to mesh distortion in the shape of an hourglass (Figure 3.17).

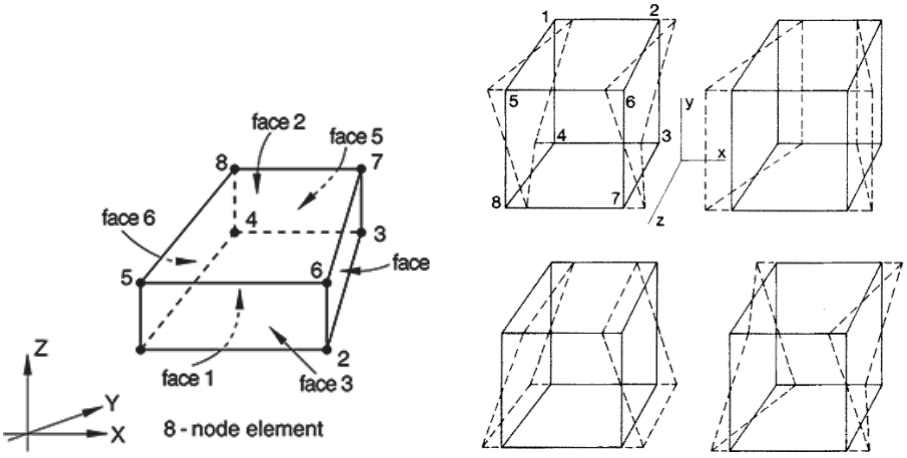

Figure 3.17: 8-noded hexahedral element and its hourglassing modes
Hexahedral element in Abaqus (left) and hourglassing in the single-integration point hexahedral element (right, Belytschko et al. (1984))

Generally, a few measures are taken to avoid hourglassing such as increasing the mesh density, using fully integrated elements (C3D8) or introducing an artificial energy into the mesh elements to reduce distortion. Due to the irregular geometries of the soft tissues, increasing the mesh density due to inherent difficulties in mesh generation and using fully integrated elements leading to an increase in the computational time significantly were not feasible solutions. Hence, the introduction of artificial energy into the elements called hourglass stiffness was an ideal choice. In Abaqus, *enhanced hourglass* was chosen, wherein an artificial stiffness was introduced in an element to reduce excessive distortions due to hourglassing.

Further, as the bones of the knee joint were meshed with 4-node tetrahedral elements and defined as rigid bodies in the FE model, C3D4[2] element type (C-Continuum, 3D-3

[2] Abaqus 6.14 online documentation, section 28.1.4
[3] Abaqus 6.14 online documentation, section 28.1.1

Dimensional, 4-number of nodes in the element) was chosen for them from the Abaqus CAE element library (Figure 3.18).

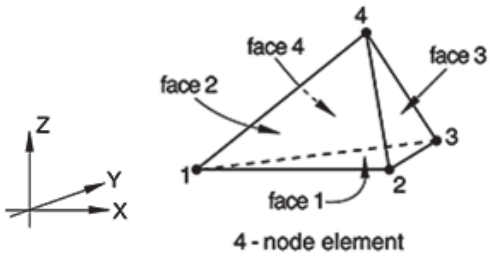

Figure 3.18: 4-noded tetrahedral element

Constraints

In Abaqus, constraints define rigid bodies and kinematic interactions between surfaces. Rigid body definitions require the creation of a *reference point*, at which all the boundary conditions of the rigid body are applied. The reference point can be the centre of mass of the body or any point in space.

The reference points of the femur and tibia rigid bodies were placed at the hip and the ankle locations instead of their centre of mass which made the application of the hip and ankle boundary conditions easier while simulating jump landing. The reference points of the patella and fibula were defined at their centre of mass locations.

A TIE constraint defined between two surfaces in Abaqus enforces zero relative motion between them. Rigid attachment of the cartilaginous structure with the bone was achieved by defining a TIE constraint between the external bony surface and the inner mesh layer of the associated cartilage (Figure 3.19). TIE constraint was defined between the femur and femoral cartilage, tibia and tibial cartilages, and patella and patellar cartilage. Since the fibula also has no relative motion with respect to the tibia, a TIE constraint was also defined between the external bony surfaces of the fibula and the tibia.

Interactions

While the relationship between bones and cartilage were defined as TIEs, the interaction of the soft tissues with each other was governed by *contact* definitions. *General contact* algorithm was used to define contact between various surface pairs in the model (Figure 3.20). The contact was defined as *frictionless* which simulates the lubricated knee joint capsule due to the presence of synovial fluid.

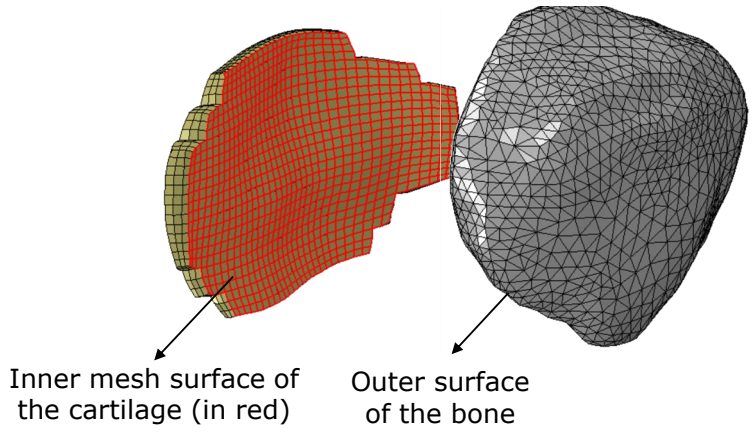

Figure 3.19: Definition of TIE constraint between the patella and patellar cartilage

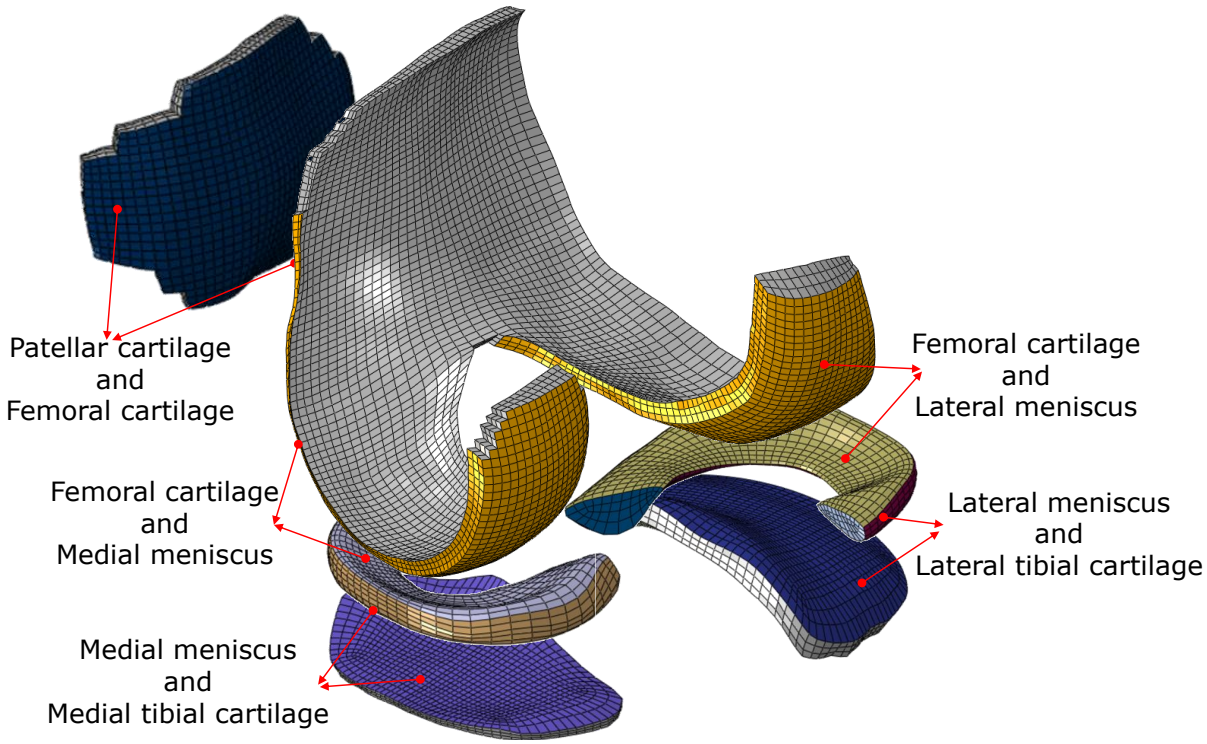

Figure 3.20: Contact definition between various surface pairs in the FE model

Material Properties

Isotropic, linear elastic material properties were assigned to bones, cartilage and menisci. The material properties were based on published data and are provided in Table 3.3.

Table 3.3: Summary of the material properties assigned to various anatomical structures

Anatomical structure	Definition in Abaqus	Young's modulus (MPa)	Poisson's ratio	Reference Study
Femur Tibia Patella Fibula	Rigid	8000	0.3	Haut Donahue et al. (2002)
Femoral cartilage Lateral tibial cartilage Medial tibial cartilage	Deformable	20	0.45	Akizuki et al. (1986)
Lateral meniscus Medial meniscus	Deformable	59	0.49	LeRoux and Setton (2002)

Akizuki et al. (1986) evaluated the tensile properties of healthy and osteoarthritic cartilage by subjecting low and high weight-bearing areas (LWA and HWA) in the femur up to 15 % strain. The authors found that the cartilage in the LWA was stiffer than the HWA and the tensile modulus was always within 30 MPa for both the areas. LeRoux and Setton (2002) conducted tensile tests to determine the transversely isotropic behaviour of the menisci. Following this experimental research, an FE study by Pena et al. (2005) evaluated average material properties for the menisci ($E = 59$ MPa and $\nu = 0.49$) to understand the effect of meniscal tears on the articular cartilage. The material properties for the bony geometries were not as critical as the other soft tissues since they were defined as rigid bodies in the FE model. Bones were also assumed as linearly isotropic material with the properties based on another FE modelling study by Haut Donahue et al. (2002).

Modelling of Ligaments

The ligaments in the knee joint were defined as spring elements exhibiting a non-linear force versus displacement relationship. In Abaqus, they were modelled as non-linear axial connector elements (CONN3D2). The axial connectors can be a spring (linear or non-linear), or a damper or a combination of both defined between two nodes a and b in an FE model (Figure 3.21). Ligaments were modelled by inputting force versus displacement curves to the connector element definition in Abaqus. In addition, the pre-strain in each ligament bundle was specified by inputting their respective zero-load lengths (L_0).

Blankevoort et al. (1991) developed a mathematical model to describe the force versus displacement behaviour of all the major ligaments in the knee joint (ACL, PCL, MCL and LCL) including the capsular ligament which was discussed in detail (Section 2.4.3). All the ligaments were modelled based on Blankevoort et al. (1991) study, except the ACL.

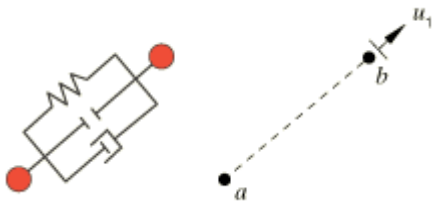

Figure 3.21: Axial connector definition in Abaqus CAE
(Abaqus 6.14 online documentation, section 31.1.5)

The response of the ACL in the validation studies was stiffer than expected with material properties from Blankevoort et al. (1991). Figure 3.22 shows the response of AM bundle of the ACL with increasing anterior force on the tibia (Lachman test, discussed in Section 3.2.1) compared with the *in-vivo* experimental strains of Beynnon et al. (1992a). In the simulation of the Lachman test, the strain in the AM bundle was approximately half of what was observed in the experiments.

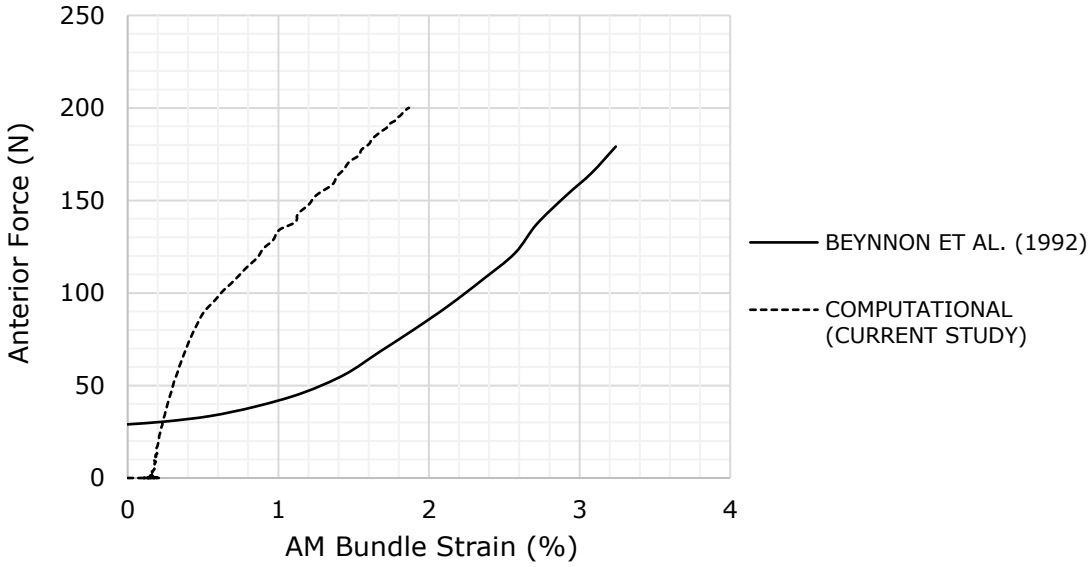

Figure 3.22: AM bundle strain versus anterior force on the tibia (Lachman test)
(with material properties from Blankevoort et al. (1991))

This stiffer response was attributed to the small toe region of the ACL curve from the mathematical model. Therefore, the material properties of ACL were obtained from another experimental study by Chandrashekar (2005). Figure 3.23 shows the force versus displacement curve of the male ACL from Chandrashekar (2005) and the one used for the AM and PL bundles in the current FE model, compared to the mathematical model where the smaller toe region can be observed.

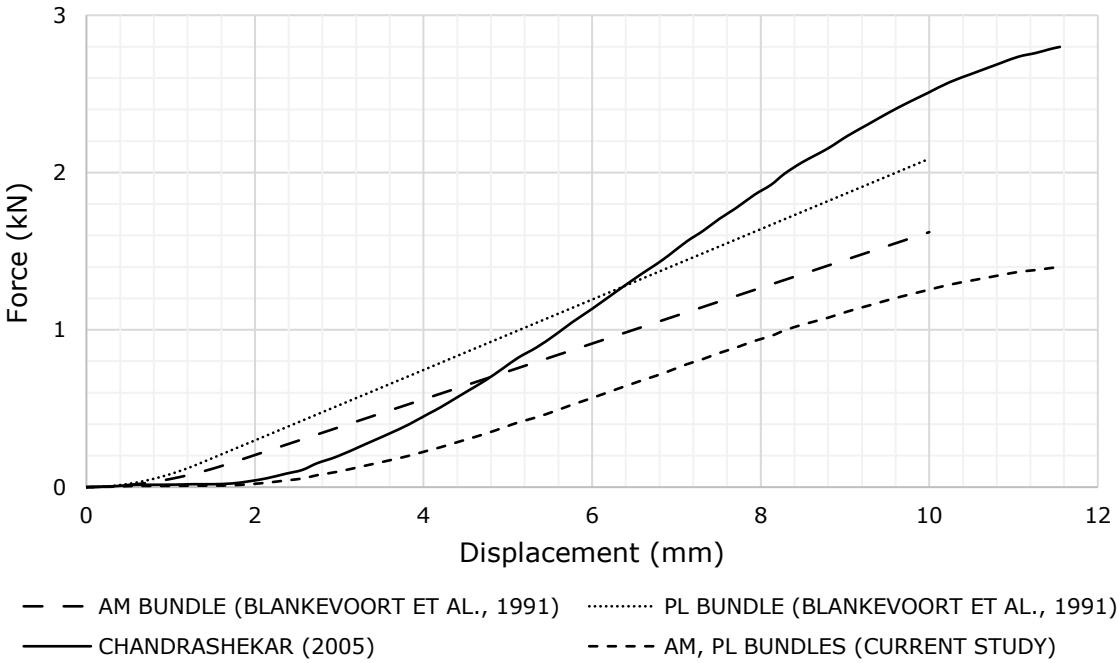

Figure 3.23: Force versus displacement curves of ACL

The force versus displacement curve from Chandrashekar (2005) was the behaviour of the ACL in its entirety; it represented the combined behaviour of the two prominent bundles in ACL: the AM and the PL bundles. In order to use this experimental curve in the current FE model, the force data was divided in half and then applied to both the bundles, imitating two parallel, non-linear springs. Pre-strain of both the bundles was maintained as reported in the Blankevoort et al. (1991) study.

MCL has two distinct regions: the superficial and the deep fibres (Section 2.1.2). Only the superficial MCL was modelled in the current study as the single-leg jump landing simulation on the DKS replicates sagittal plane mechanics only. The role of the ACL dominates that of the MCL in the sagittal plane mechanics (Bates et al., 2015).

Table 3.4 shows the values of stiffness parameter, k and reference strain, ε_r of the ligaments from Blankevoort et al. (1991). Zero-load length (L_0) of each ligament bundle was input as the *Reference length U1* in the connector element definition in Abaqus. The negative values of reference strain in Table 3.4 indicate that the particular ligament fibre is slack in extension. The force versus displacement curves, obtained from the mathematical model, is shown in Figure 3.24. Guess (2012) added a small damper (damping co-efficient of 0.5 Ns/mm) in parallel to the ligament spring elements to remove the high-frequency vibrations in the output of simulations involving walking and double-leg squats. Similarly, a damping co-efficient of 0.1 Ns/mm (equivalent to 0.1 % of ligament stiffness) was applied in parallel to the non-linear springs.

Table 3.4: Material properties assigned to the major knee ligaments

Ligament	Ligament bundle	Stifness parameter, k	Strain at extension, ε_r	Reference study
ACL	Anteriomedial Posterolateral	NA	0.06 0.10	Chandrashekar (2005); Blankevoort et al. (1991)
PCL	Posteromedial Anterolateral	9000 9000	−0.15 −0.03	Blankevoort and Huiskes (1996)
Superficial MCL	Anterior Middle Posterior	2750 2750 2750	0.04 0.04 0.03	Blankevoort et al. (1991)
LCL	Anterior Middle Posterior	2000 2000 2000	−0.25 −0.05 0.08	Blankevoort et al. (1991)

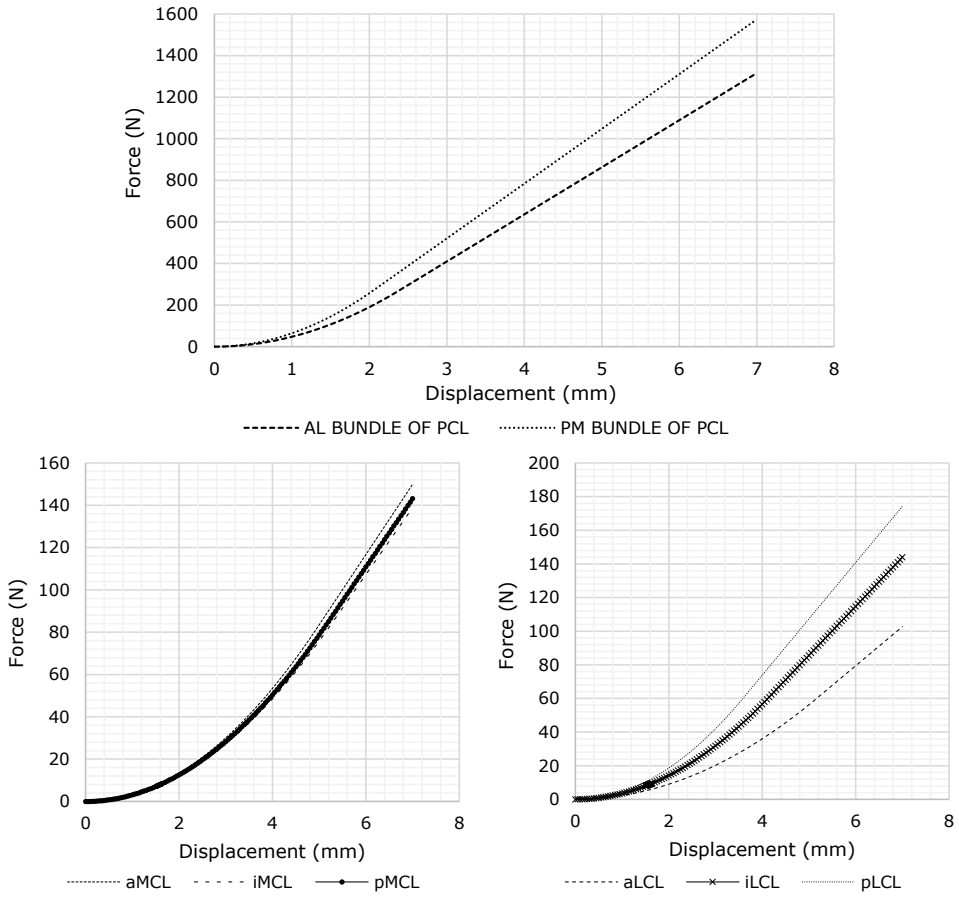

Figure 3.24: Force versus displacement curves of ligaments by Blankevoort et al. (1991) PCL (top) and MCL (bottom left) and LCL (bottom right)

In addition to the major ligaments of the knee joint described previously, certain other ligamentous structures required for the appropriate kinematic response of the FE model were also included. These were the patellar tendon, medial and lateral patella-femoral ligaments (MPFL and LPFL) and meniscal horn attachments. The patellar tendon (or patellar ligament), which exists between the patella and the tibial tuberosity was defined as a set of three tension-only linear springs with a combined stiffness 545 N/mm (Schatzmann et al., 1998). MPFL and LPFL attach on the medial and lateral side of the patella to the respective sides on the femur. These ligaments were required to stabilize the patella under the application of high quadriceps forces during a jump landing simulation. They were also defined as linear springs with a stiffness of 16 N/mm for MPFL and 12 N/mm for LPFL (Atkinson et al., 2000).

Furthermore, meniscal horns were defined to secure the ends of the menisci to the tibial plateau. The horns were defined at the anterior and posterior ends of both lateral and medial menisci as linear springs with a stiffness of 180 N/mm each (Hauch et al., 2010). Figures 3.25 and 3.26 show all the additional stabilising ligaments defined in the FE model.

To avoid instabilities due to stretching of just one node where the horns attach to the ends of the menisci, a small rigid body was attached to its ends, using TIE constraints. The meniscal horns attach to the rigid body instead of pulling on the nodes at the ends of the menisci (Figure 3.27).

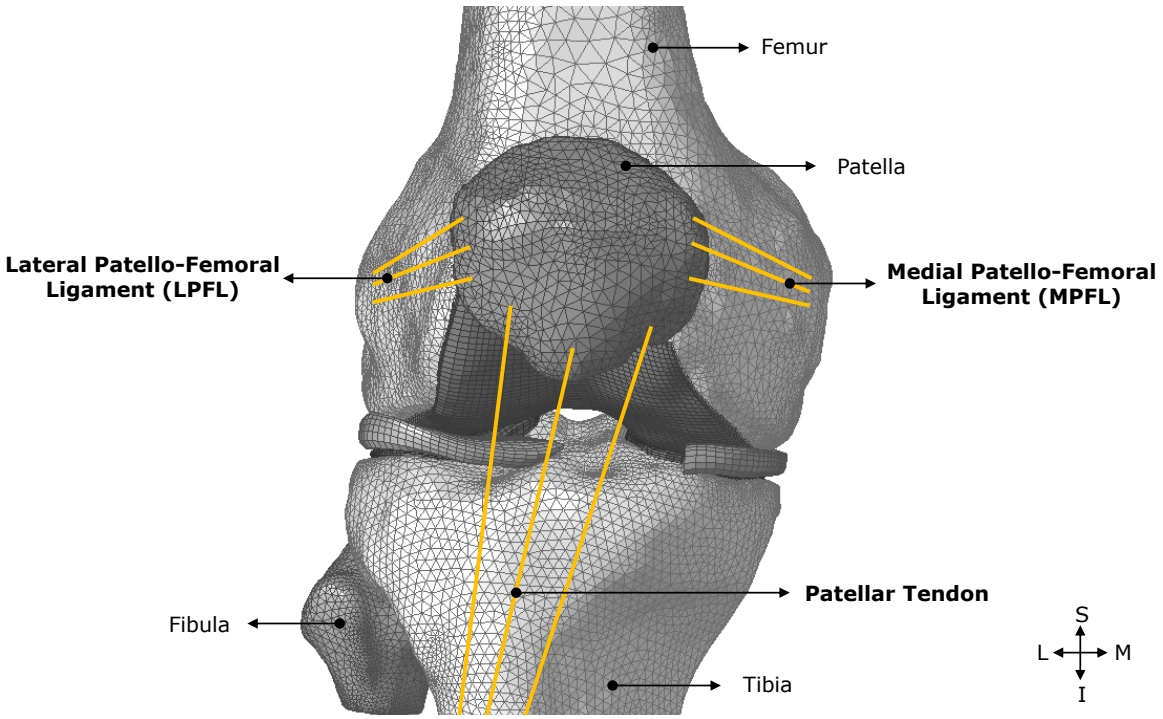

Figure 3.25: Secondary ligaments between patella, femur and the tibia

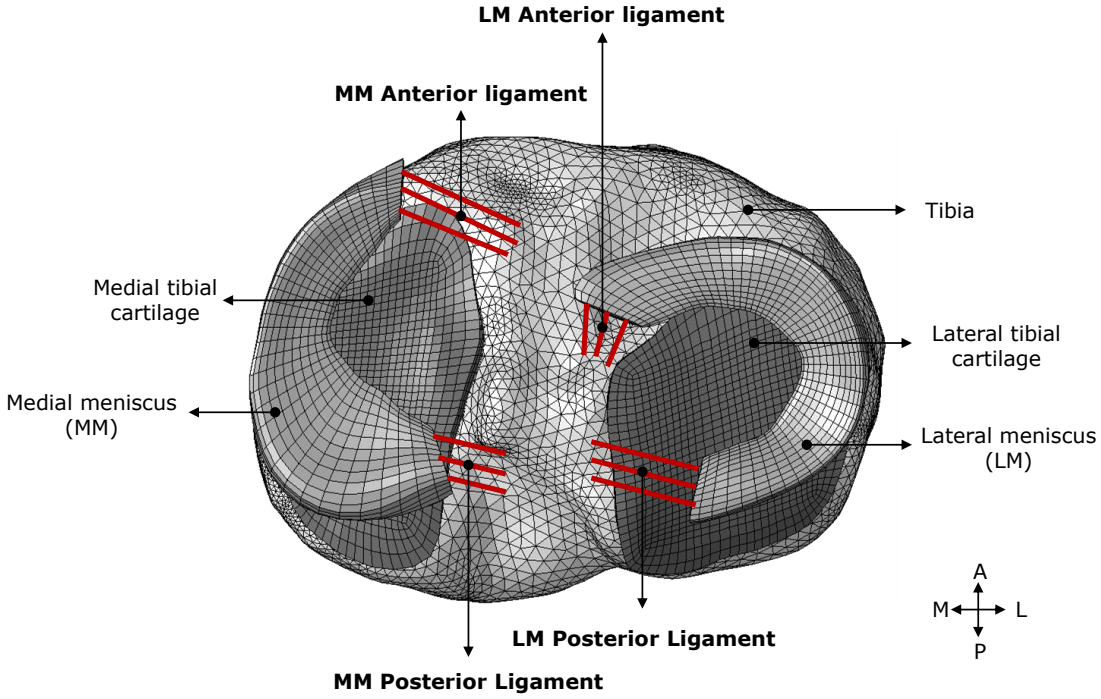

Figure 3.26: Secondary ligaments in tibia

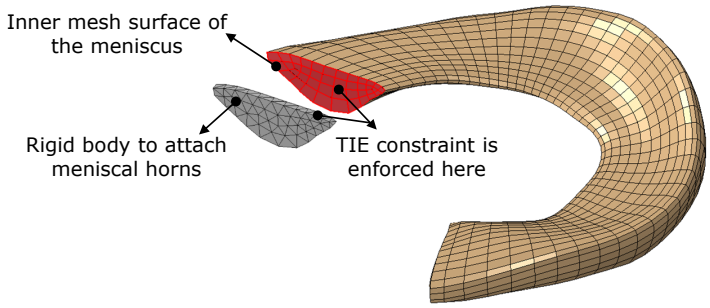

Figure 3.27: Rigid bodies at the ends of menisci

3.2 Finite Element Analysis

Following the assembly of the meshed anatomical structures in Abaqus, a global coordinate system was established in the model, similar to the experimental test setup in the DKS. Next, to verify if the kinematic responses predicted by the model were valid and reasonable, few kinematic verification simulations were carried out, and the results were compared to published data.

Coordinate System

According to the *in-vivo* study by Asano et al. (2005), the transepicondylar axis, which connects the medial sulcus and the lateral peak of the femoral condyle was chosen as the flexion-extension axis of the knee model. Similar to the DKS nomenclature, the transepicondylar axis was made the z axis in the FE model, which defines the sagittal plane.

In the DKS, the *origin* is the point where the hip and ankle guide rails coincide. The x and y axes are the translational directions of the ankle and hip, respectively (Figure 3.28).

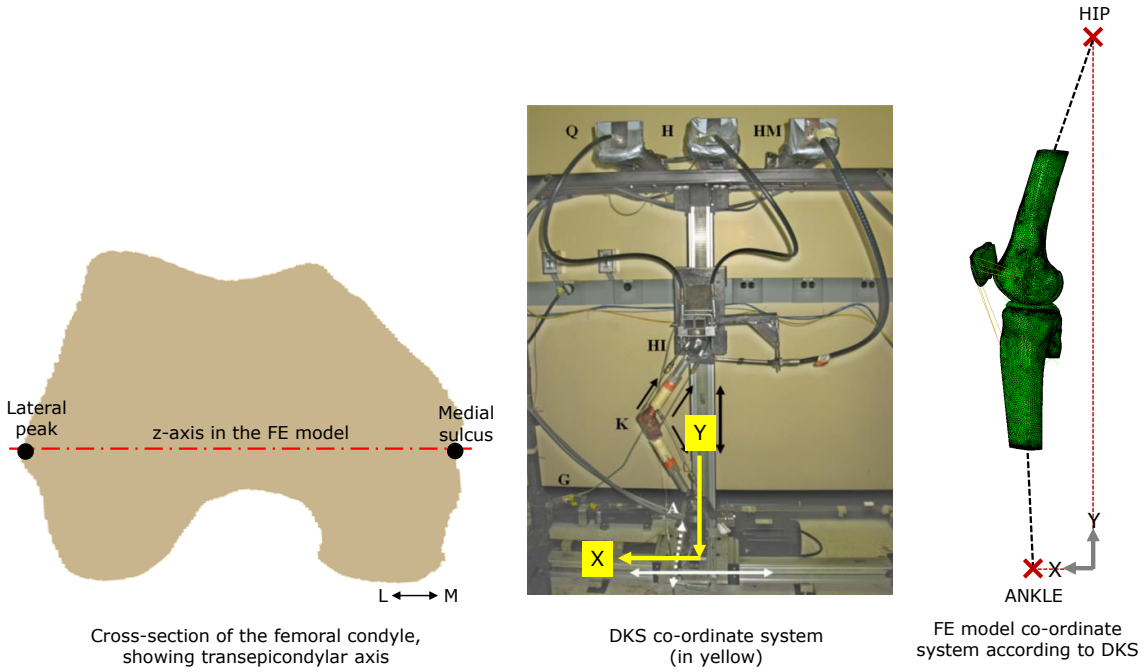

Figure 3.28: Knee co-ordinate system
Flexion-extension axis (left), DKS co-ordinate system (centre, adapted from Cassidy et al. (2013)) and FE model (right)

3.2.1 Verification of Kinematics

To verify the FE model's capability to accurately replicate kinematics of the knee joint, few basic motions of the knee joint were simulated: flexion, Lachman test, anterior drawer test (in the sagittal plane), abduction (in the frontal plane) and internal rotations of the tibia during flexion (in the axial plane). The results were then compared to *in-vivo* and *in-vitro* experimental data from published studies.

Flexion was achieved by applying a hamstring force ($\sim$ 600 N) to the posterior tibia by fixing the femur in place (Figure 3.29). ACL strain during flexion was recorded and compared to the *in-vivo* experimental strain in the AM bundle from Beynnon et al. (1992a).

In addition, kinematics of the knee in the axial plane was verified by recording the internal rotation of the tibia along the tibial axis (screw-home mechanism) during flexion and comparing it to the *in-vitro* experimental measurements of Kiapour et al. (2013).

The motion of the knee joint in the frontal plane was verified by simulating pure abduction at 25° knee flexion. An initial hip displacement was applied to achieve the initial 25° flexion during which the motion of the tibia was restricted. Up to 50 N·m of abduction moment was applied at the knee joint along with 400 N quadriceps force and 200 N hamstring force (Figure 3.29). Knee valgus (in degrees) was measured and compared to the *in-vitro* experimental results from Kiapour et al. (2013).

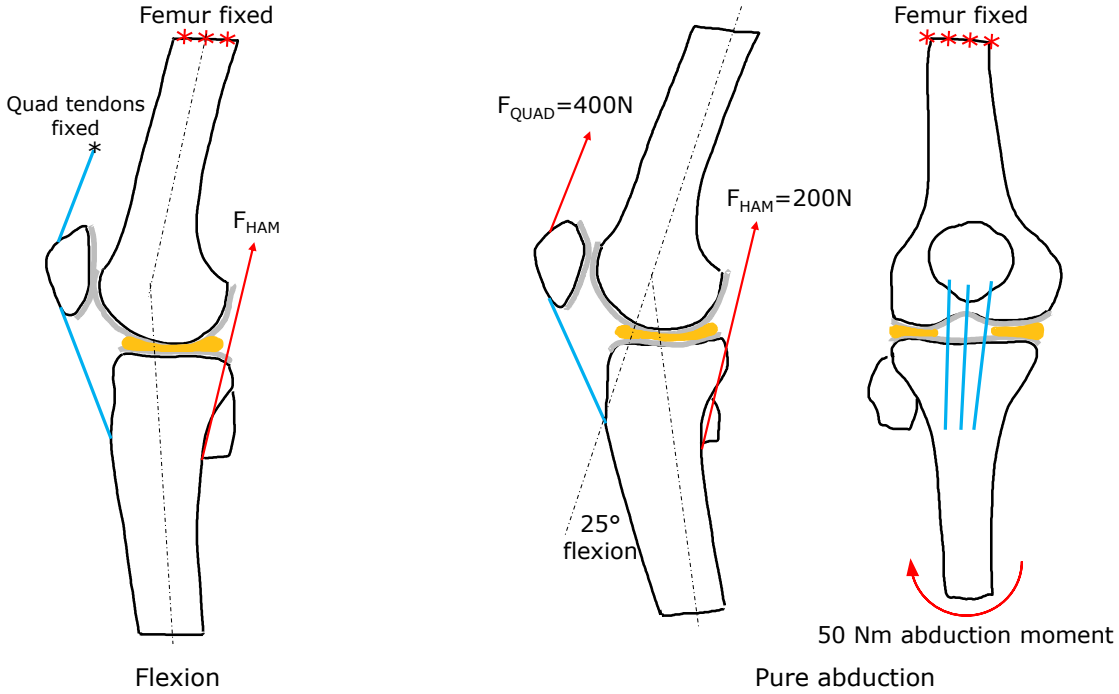

Figure 3.29: Boundary conditions for flexion (left) and pure abduction (right) simulations

ACL strain in the sagittal plane motion was verified with an *in-vivo* study by Beynnon et al. (1992a), where the anteromedial ACL strain was measured under varying anterior-posterior load on the tibia at 30° and 90° flexion angles, simulating Lachman and anterior drawer tests, which are the physiological tests performed on a patient to determine ACL tear. The knee was flexed to 30° and 90° by passively flexing the knee, by displacing the hip node. Anterior shear loads of up to 200 N were applied to the tibia at 30° of flexion to simulate Lachman test and at 90° of flexion to simulate anterior draw test (Figure 3.30). Strains in the anteromedial ACL bundle were compared to the *in-vivo* experimental results from Beynnon et al. (1992a).

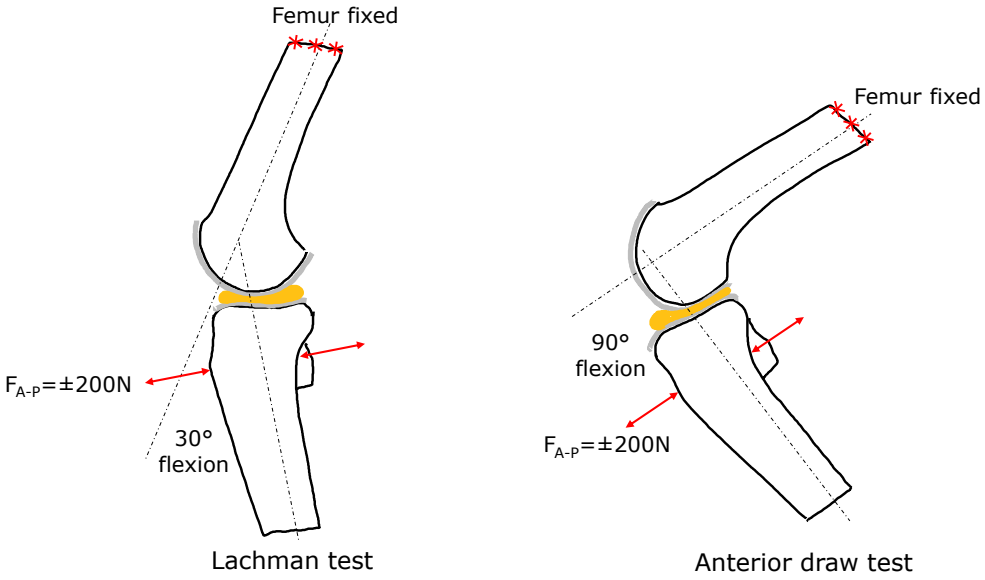

Figure 3.30: Boundary conditions for Lachman (left) and anterior draw (right) simulations

A summary of all the basic knee motions simulated is provided in Table 3.5. All simulations were solved in Abaqus/Explicit solver with double precision.

Table 3.5: Summary of kinematics verification studies

Knee motion	Boundary condition	Comparison metric	Reference study
Flexion	Hamstring force applied to tibia, femur is fixed	ACL strain, internal rotation of the tibia	Beynnon et al. (1992b) Kiapour et al. (2013)
Pure abduction at 25° flexion	50 N·m abduction moment on tibia, femur is fixed	ACL strain, Knee valgus	Kiapour et al. (2013)
Lachman test at 30° flexion	200 N A-P force applied to tibia, femur is fixed	ACL strain	Beynnon et al. (1992b)
Anterior draw at 30° flexion	200 N A-P force applied to tibia, femur is fixed	ACL strain	Beynnon et al. (1992b)

3.2.2 Boundary Conditions for Single-Leg Jump Landing

The current study replicated the *in-vitro* jump landing simulation on the DKS at the University of Waterloo. A detailed description of its construction and the *in-vitro* experiments performed on it can be found in Bakker et al. (2016); Cassidy et al. (2013); Hangalur et al. (2016) and Polak (2019).

Bakker (2015) performed a motion capture study collecting the GRFs and kinematics of ten participants during single-leg jump landing (Table 3.6). Dynamic muscle forces, hip flexion moments and kinematics of hip and ankle were generated from the motion capture data using inverse dynamics in OpenSim. Further, *in-vitro* jump landing simulations were carried out on five cadaver specimens, and ACL strain was recorded. The current study replicates the ten jump landing profiles from Bakker (2015) study in the knee FE model.

Table 3.6: Participant information for jump landing trials, adapted from Bakker (2015)

			Limb length (mm)	
Participant	Sex	Body mass (kg)	Femur	Tibia
P1	F	59.0	399	368
P2	F	61.0	422	404
P3	M	72.0	429	396
P4	M	79.0	422	391
P5	F	57.5	411	381
P6	F	67.5	411	381
P7	F	66.0	437	404
P8	M	72.5	442	427
P9	M	74.0	422	391
P10	M	65.0	404	381
Average (SD)		67 (7)		

The duration of the FE simulation in Abaqus was 400 ms, which incorporates the first 100 ms of muscle pre-loads initialization. During the pre-loads, hip and ankle had no kinematic input. The next 300 ms was split into 100 ms of pre-ground and 200 ms of post-ground contact in accordance with the *in-vitro* simulations of Bakker et al. (2016) and Polak (2019), as represented in Figure 3.31. Kinematic and kinetic boundary conditions applied to the knee model to simulate the jump landing is described in the following section.

Kinematic Boundary Conditions

Kinematic boundary conditions for jump landing on the DKS are applied at the hip and the ankle as velocities (instead of displacement), which was replicated in the knee FE model as well. The ankle was unrestricted in rotation and free to translate in the x and the z axis but was restricted in the y axis. The hip was free to translate in the y axis but was restricted in the x and the z axis. The rotation of hip was allowed about the z axis but was restricted about the other two axes. Figure 3.32 shows the hip and ankle displacement curves of participant profile P1 for a single leg jump landing simulation. These displacement curves were applied to the reference points of the femur and tibia, which were placed at the hip and ankle locations, respectively (Figure 3.34).

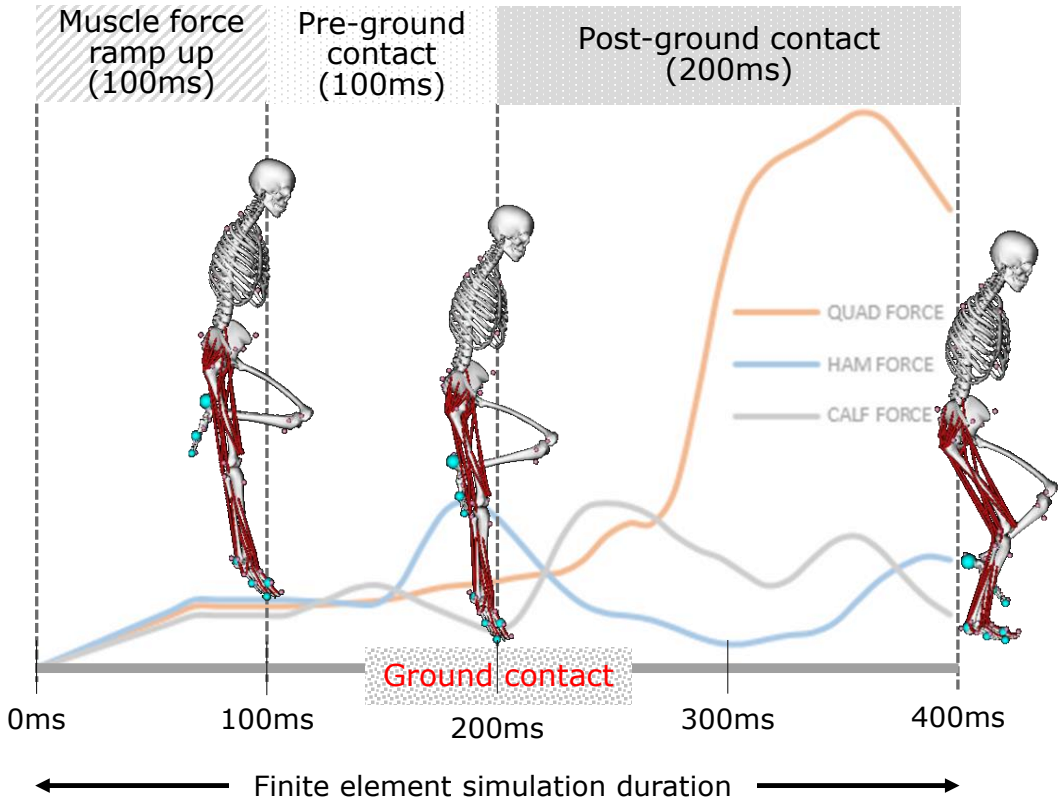

Figure 3.31: Single leg jump landing simulation timeline (with P5 muscle force profile in the background)

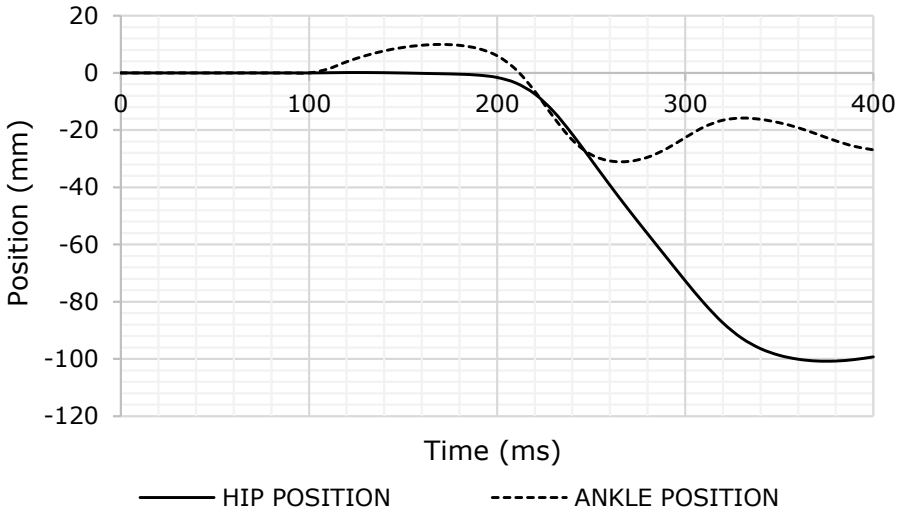

Figure 3.32: Hip and ankle kinematics of P1 participant profile

Kinetic Boundary Conditions

The single-leg jump landing simulation involved the application of three dynamic muscle forces, quadriceps, hamstrings and gastrocnemius (or calf) and a hip flexion/extension moment (Bakker et al., 2016). To apply the appropriate magnitude of muscle force profiles of each participant, muscle moment arms were needed. For each muscle group, the moment arm was measured by tendon excursion technique (Delp et al., 1994). Under the application of any one muscle force, the displacement of the point of application of the load (equivalent to the change in the length of the muscle cable, in the experiments) was plotted versus the knee flexion angle. The slope of the resulting curve gives the moment arm of that muscle force. To measure the quadriceps and hamstring moment arms, the femur was constrained in all DOF and suitable values of quadriceps or hamstring force to cause knee extension/flexion was applied. The quadriceps and hamstring forces were applied on three nodes on the patella and on the posterior tibia, parallel to the long axis of the femur, respectively. The gastrocnemius moment arm was measured by constraining the tibia in all DOF and applying gastrocnemius force on the femur. It was applied on three nodes on the posterior femur and the line of action parallel to the long axis of the tibia (Figures 3.33 and 3.34). The points of application of all the muscle forces were maintained at the same locations as the muscle cable attachments to the cadaver specimen (Figure 3.33).

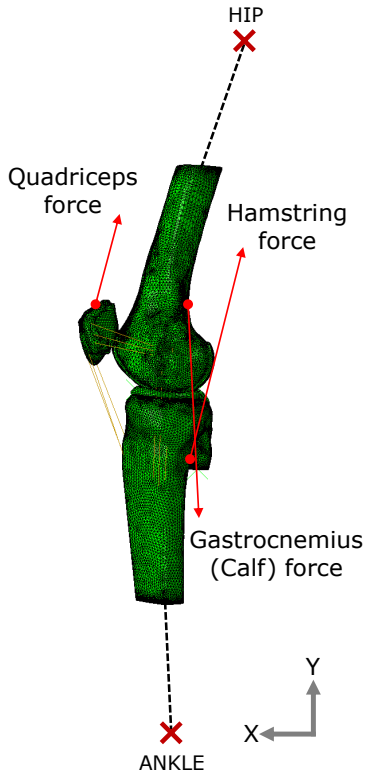

Figure 3.33: Location of application of muscle forces in the FE model

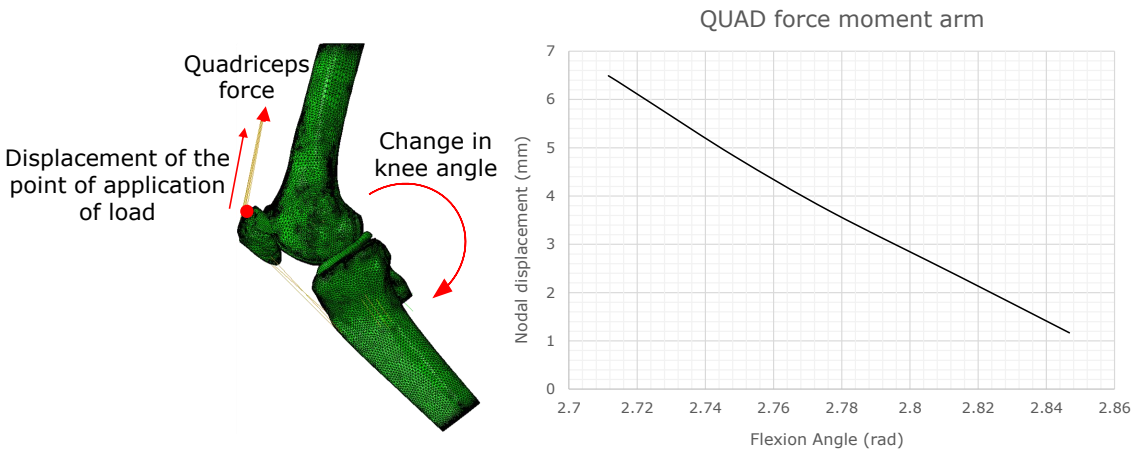

Measurement of Quad force moment arm

Figure 3.34: Measurement of moment arms by tendon excursion technique

The measured moment arm values were input in a MATLAB program developed by Bakker (2015) to obtain the appropriate muscle forces for all the participant profiles from P1 to P10 and the same for profile P1 shown in Figure 3.35.

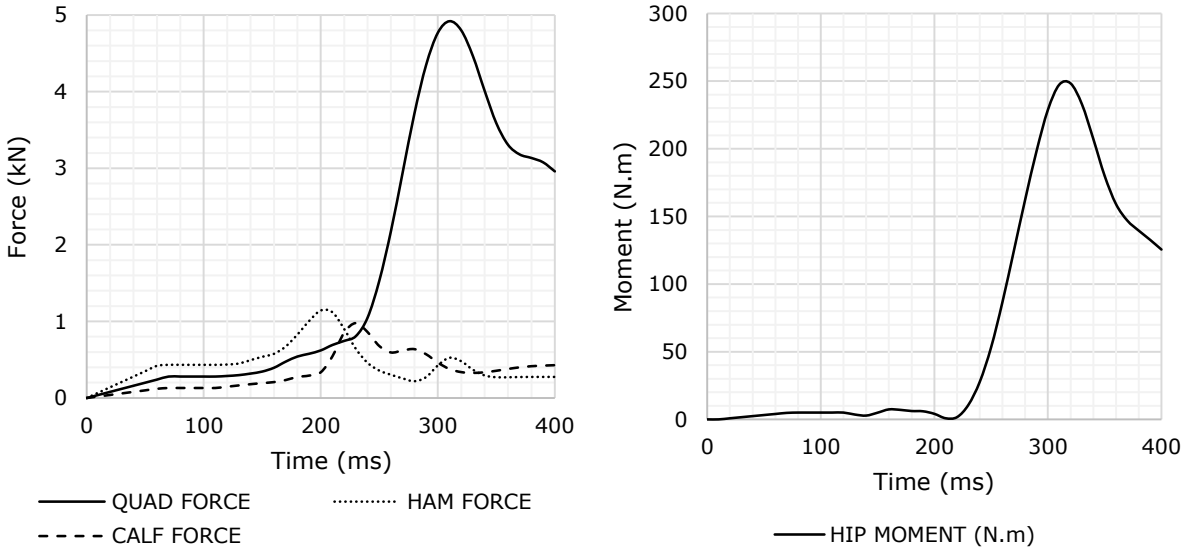

Figure 3.35: Muscle forces (left) and hip moment (right) of participant profile P1

3.2.3 Single-Leg Jump Landing Simulations

Polak (2019) conducted *in-vitro* jump landing simulations on the DKS at University of Waterloo, based on two participant profiles, P5 and P6 taken from the study by Bakker

et al. (2016). Kinetic and kinematic boundary conditions of these profiles were applied on three cadaver specimens, one of which was chosen to be developed as a subject-specific model in the current study. During the *in-vitro* simulations on the DKS, before running the jump landing simulation with the actual muscle forces, the muscle forces were halved to ensure proper working of the muscle cables other instrumentation first, since the damage to the cadaver specimen is more probable during a full muscle force jump (Polak, 2019). On the cadaver specimen chosen for the current study, only half muscle force jumps could be performed because the ACL ruptured during the full muscle force jumps. Accordingly, to compare with the available experimental ACL strain data, half muscle force single-leg jump landing of two participant profiles, P5 and P6 were simulated first.

Once the initial simulations were completed, full muscle force jump simulations of all the participant profiles, P1 through P10 were performed by inputting their respective dynamic muscle force profiles, hip moment and velocities at the hip and ankle (Figure 3.35 and Appendix A). For each participant profile jump, the limb lengths and the starting positions of the hip and ankle were varied, according to the data in Table 3.6. The experimental knee flexion angle at the start of the jump for all the participant profiles was close to extension (flexion angles between 8° and 15°). Since the cadaver specimen of the current study was scanned in extension in the cast, the flexion angle was at maintained close to 12°, and hence the initial knee flexion angle was not varied for each participant.

In participant profiles, P4, P8, P9 and P10, the muscle forces were relatively high compared to the other profiles (Appendix A). As a result, the distortion of the elements in these simulations was excessive in femoral and patellar cartilages; this necessitated the application of a stiffer material. Steel material properties were assigned to these structures as an intermediate fix (Young's modulus=200GPa and Poisson's ratio=0.3). To verify this approach did not affect the ACL strain significantly, the P5 profile, which had run to completion successfully with cartilage properties, was rerun with steel material properties (assigned only to patellar and femoral cartilages) and the ACL strain was measured in each case. Figure 3.36 shows the difference in ACL displacement when the normal (cartilage) and steel material properties were used. The difference in peak ACL strain values was 0.6 %. Therefore, in the participant profiles where the muscle forces were relatively higher, steel material properties were used for femoral and patellar cartilages only. All the simulations were run on Abaqus/Explicit solver with double precision on a 64-bit, 16 GB RAM, Intel® Core™ i7-7700 CPU.

Similar to the experimental results, ACL strain, ε was calculated using the engineering strain formula:

$$\varepsilon = \frac{\Delta L}{L_0}$$

ΔL is the displacement or change in length of the ACL bundle. L_0 is the gauge length or the initial length of ACL. Bakker (2015) reported ACL strain during the last 200 ms

of the jump landing simulation, and Polak (2019) reported the strain during the last 300 ms of the simulation. Hence L_0 was chosen as the length of ACL at the time of ground contact (200 ms) to compare with the experimental results of Bakker (2015) and at 100 ms to compare with the results of Polak (2019).

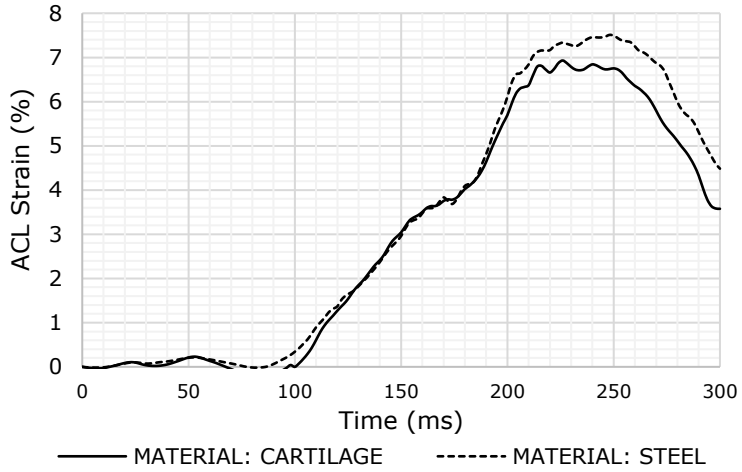

Figure 3.36: ACL strain with different material properties assigned to cartilages
Small differences in ACL strain in the simulation of single-leg jump landing when cartilage and steel material properties were assigned to femoral and patellar cartilages

Medial Meniscus Strain

In addition to the ACL strain, Polak (2019) also measured meniscal strain on the posterior region of the medial meniscus to study the effect of CTi® knee brace (Össur Canada, Richmond, BC, Canada). Experimental strain during jump landing was measured with and without a knee brace, using a DVRT. In the FE model, displacement of two nodes in the posterior region of the medial meniscus, at approximately the same location as the DVRT (Figure 3.37) was extracted, and the strain was calculated using the engineering strain formula described previously.

Comparison With *In-Vitro* Data

Generally, validation of subject-specific FE models is challenging, with often limited experimental data available for each subject. As described previously, in our lab, the biomechanics of single-leg jump landing on ACL strain has been studied extensively. In the study Bakker et al. (2016), motion capture data was obtained from single-leg jump landings of ten recreational athletes (P1-P10). Muscle forces and knee joint kinematics of the jump were then generated using an OpenSim musculoskeletal model. In addition, *in-vitro* jump landing experiments were carried out on five cadaver knee specimens (BK1,...BK5) based

on seven participant profiles (P1-P7). Due to cadaver specimen failure, profiles P8-P10 were not experimentally tested.

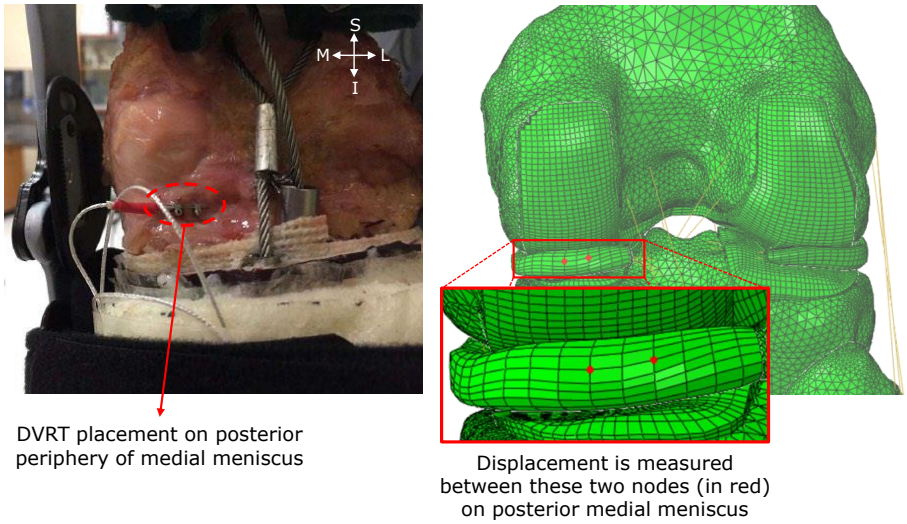

Figure 3.37: Meniscal strain measurement
DVRT placement on posterior medial meniscus (left, adapted from (Kalra et al. (2019)) and the location of meniscal displacement measurement in the FE model (right)

In the follow-up experimental study of Polak (2019), two jump landing profiles, P5 and P6, taken from Bakker (2015) were experimentally tested on three cadaver specimens (PK1, PK2, PK3). In addition, single-leg jump landing was also simulated on a 50th percentile male knee FE model from GHBMC, and the ACL strain results were compared to the experimental data. Table 3.7 provides a summary of the experimental studies.

Table 3.7: Experimental data available for comparison of computational results

Cadaveric specimen[4]	*In-vivo* participant profile tested	Muscle force condition	*In-vitro* cadaveric study	Comparison metric
PK1[5]	P5, P6	Half	Polak (2019)	Relative ACL strain; posterior medial meniscal strain
PK2		Half, Full		
PK3		Half, Full		
BK1	P1,...,P6	Full	Bakker et al. (2016)	Relative ACL strain
BK2	P1,...,P6	Full		
BK3	P1,...,P7	Full		
BK4	P1,...,P7	Full		
BK5	P1,P5	Full		

[4]PK:Polak-Knee, BK:Bakker-Knee, P:Participant
[5]PK1 cadaver specimen was developed as the subject-specific model in the current study

From the experimental work of Polak (2019), the cadaveric specimen PK1 was chosen for the development of the initial subject-specific FE model in the current work. Following the kinematic verification of the FE model, the ACL and meniscal strain results from the FE model were compared to the experimental results of PK1, under half muscle force condition. The goodness of fit between the computational and experimental strains was quantified by root mean squared error (RMSE) and Pearson correlation coefficient (r), similar to previous studies (Chen et al., 2016; Kiapour et al., 2013; Polak, 2019). RMSE is the square root of the mean value of squared differences between two data point sets, and the Pearson correlation coefficient provides the extent of the linear relationship between two data sets. RMSE close to zero indicates a very low error between the expected (experimental) and observed (computational) values. The value of r varies between -1 (negatively correlated) and $+1$ (positively correlated), with $r = 0$ suggesting no correlation.

Further, all ten jump landing profiles (P1-P10) were simulated on the FE model, under full muscle force condition. ACL strain results from the simulations of participant profiles P1-P7 were compared to the experimental results of Bakker et al. (2016). No experimental data was available to compare the results from the jump landing simulations of participant profiles P8, P9 and P10.

Chapter 4

Results

The results of each step in the generation and execution of the FE model are discussed in this Chapter. First, the mesh quality of the hexahedral mesh output was evaluated. This is followed by the results of the moment arm simulations. Lastly, the results of kinematic verification studies and the single-leg jump landing simulations are discussed in detail.

4.1 Mesh Output and Quality

For the FE mesh, tetrahedral elements were chosen for the bones, and the other soft tissues were meshed with hexahedral elements. The metrics of the hexahedral and tetrahedral meshes are reported in Table 4.1.

Table 4.1: Details of the mesh of knee tissues in the FE model

Knee tissue	Type of mesh	Number of nodes	Number of elements	Average element edge length (mm)
Femur	Tetrahedral	38442	190673	2.75
Tibia		35200	176093	2.31
Patella		3630	17096	2.20
Fibula		4804	21037	2.10
Femoral cartilage	Hexahedral	13924	9858	1.70
Lateral tibial cartilage		3880	2760	1.41
Medial tibial cartilage		3900	2772	1.34
Patellar cartilage		3596	2502	1.32
Lateral meniscus		2491	1840	1.23
Medial meniscus		1855	1360	2.07

4.1.1 Hexahedral Element Quality

Yang (2018) reported the generally accepted values of mesh quality measures of biological tissues (Jacobian > 0.6; warpage < 15°; element aspect ratio < 3 for 95 % of all elements in a structure; internal angles to be in the range 45° - 135°). All the hexahedral elements were checked for these measures in HyperMesh and found that the Jacobian of more than 97 % of all the elements was greater than 0.6; warpage of more than 99.7 % of the elements was less than 15°. More than 70.6 % of the menisci elements had an aspect ratio of less than three. In the meshes of all other structures, more than 83 % of the elements had aspect ratios of less than three. More than 88.5 % of all the elements had the internal and external angles in the range 45° - 135°, except the medial meniscus, in which only 65.2 % of the elements had angles in the preferred range. Yang (2018) also stated that it is acceptable to have a small percentage of sub-par elements in an FE model of biological tissues since the complete elimination of all elements with low-quality would require considerable time and effort. Figure 4.1 shows a summary of the element quality measures.

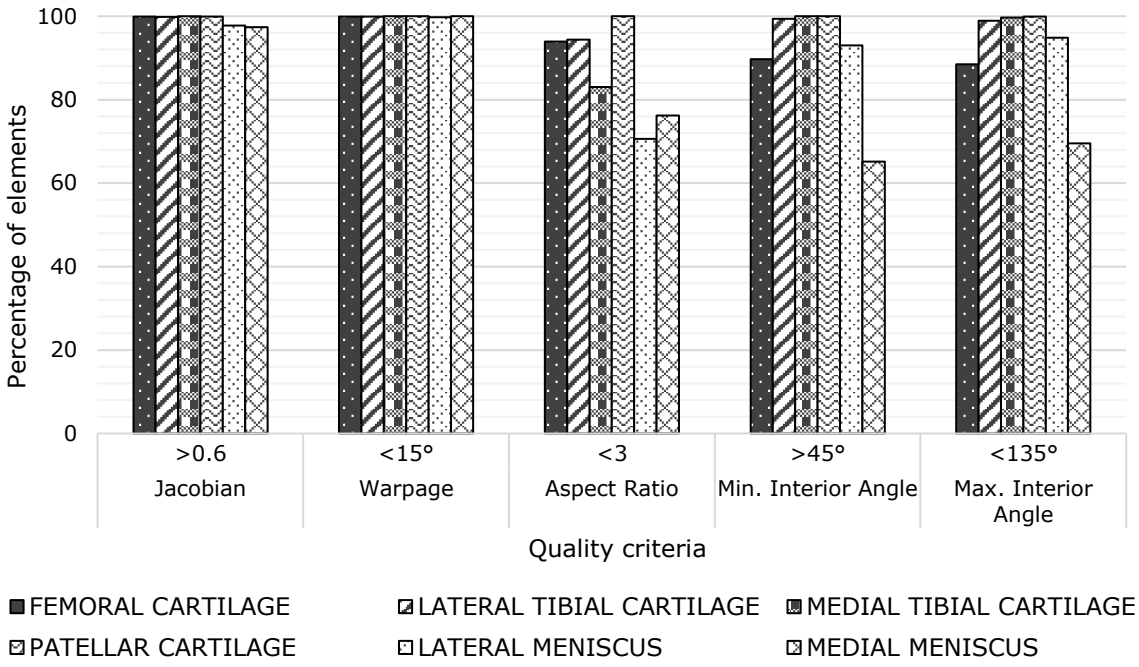

Figure 4.1: Summary of hexahedral element quality of the knee soft tissue meshes

4.2 Kinematic Verification Studies

Kinematic verification of the FE model, specifically with respect to ACL mechanics, was carried out. It included verification of coronal, axial and sagittal plane mechanics with published data. Figure 4.2 shows the strain pattern of two ACL bundles, the AM and the

PL bundles during flexion, which is compared against the *in-vivo* experimental values from Beynnon et al. (1992a).

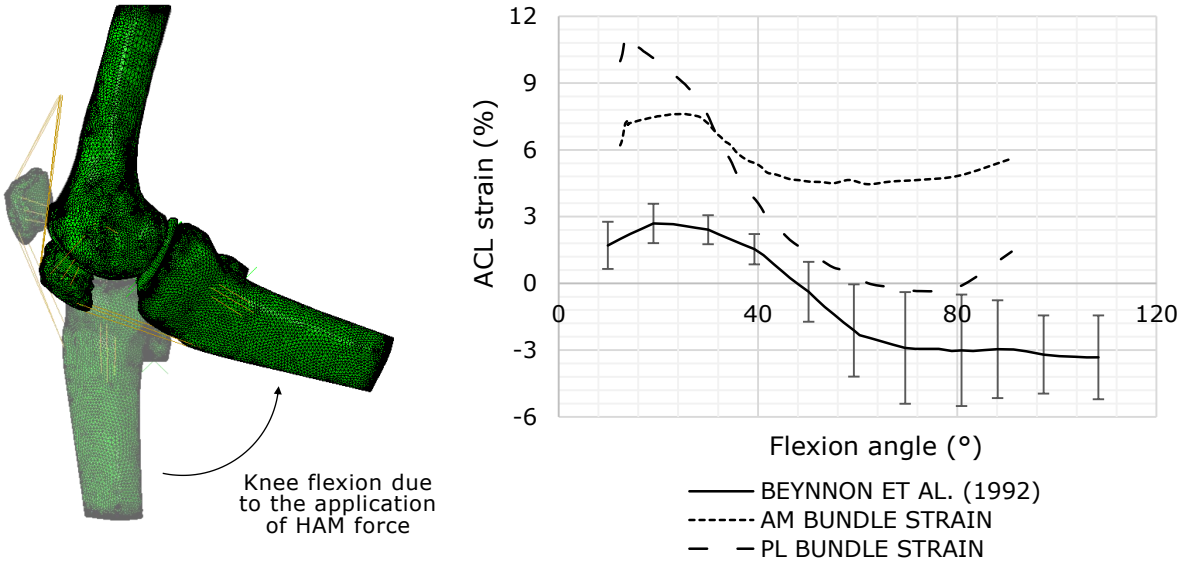

Figure 4.2: ACL strain with increasing flexion angle (active range of motion)

During flexion, the tibia undergoes an internal rotation along its axis. The internal rotation of the tibia during flexion was compared with the *in-vitro* experimental and computational study of Kiapour et al. (2013), in Figure 4.3.

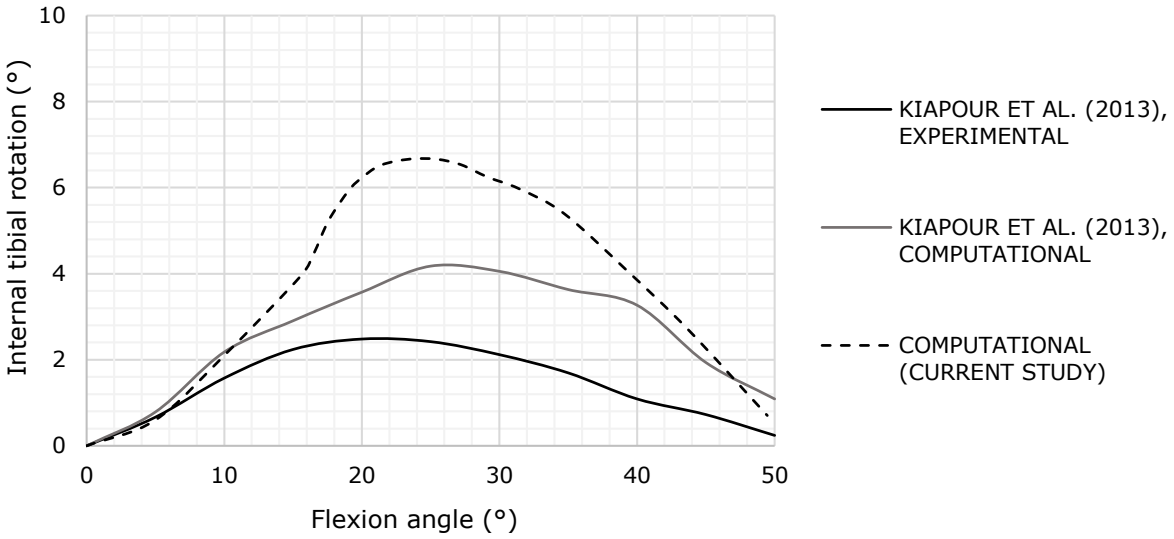

Figure 4.3: Internal tibial rotation with flexion

Lachman and anterior drawer tests verified the sagittal plane motion. ACL strain in the application of ± 200 N anterior-posterior load on the tibia was compared with the *in-vivo* data of Beynnon et al. (1992a), as shown in Figure 4.4.

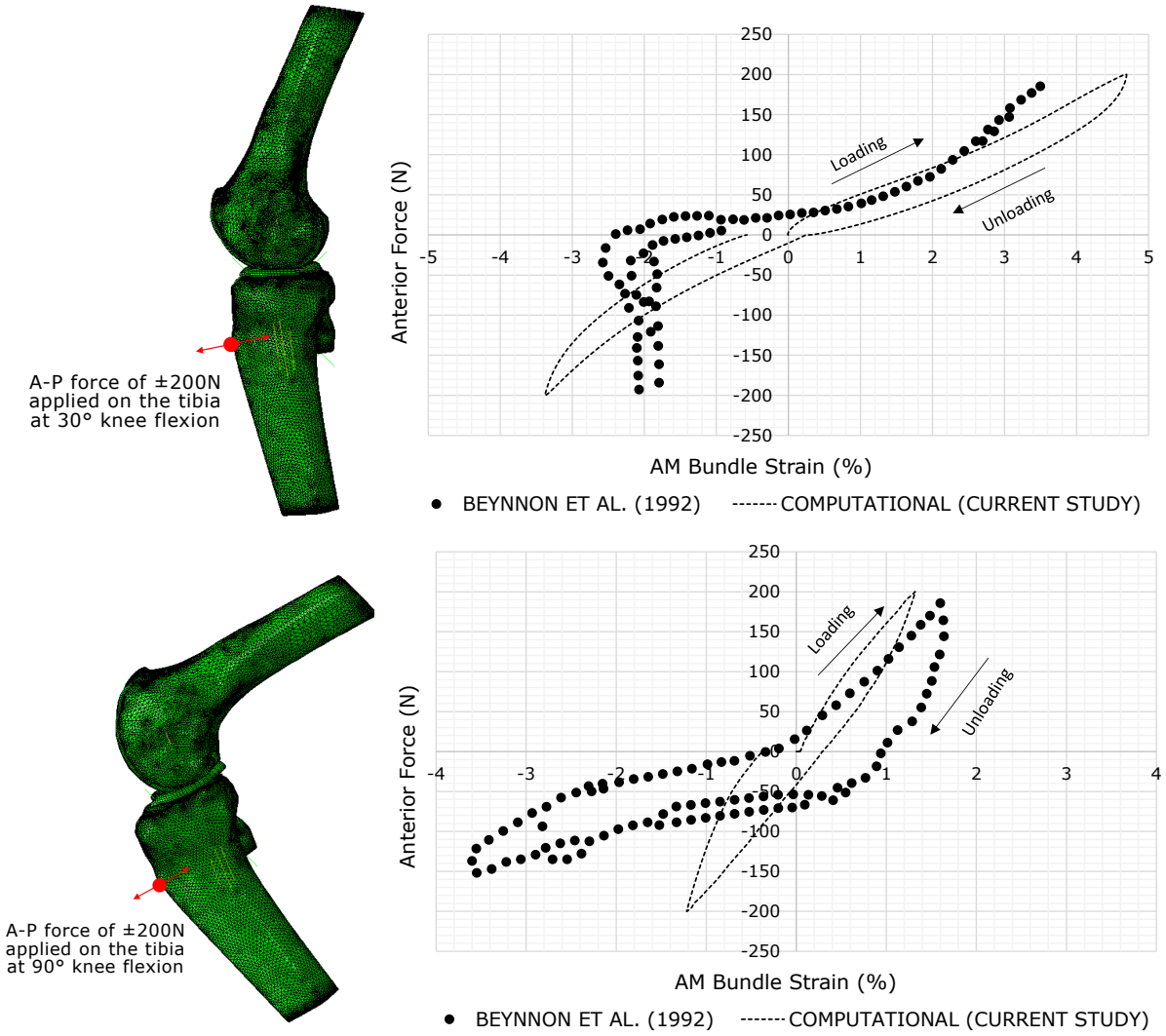

Figure 4.4: AM bundle strain during Lachman (top) and anterior drawer (bottom) simulations

The coronal plane motion was verified by simulating pure abduction motion, with 50 N·m abduction moment on the tibia. Figure 4.5 shows the comparison of the computational ACL strain with the *in-vitro* and computational results of Kiapour et al. (2013) and Figure 4.6 shows the knee valgus rotation with increasing abduction moment.

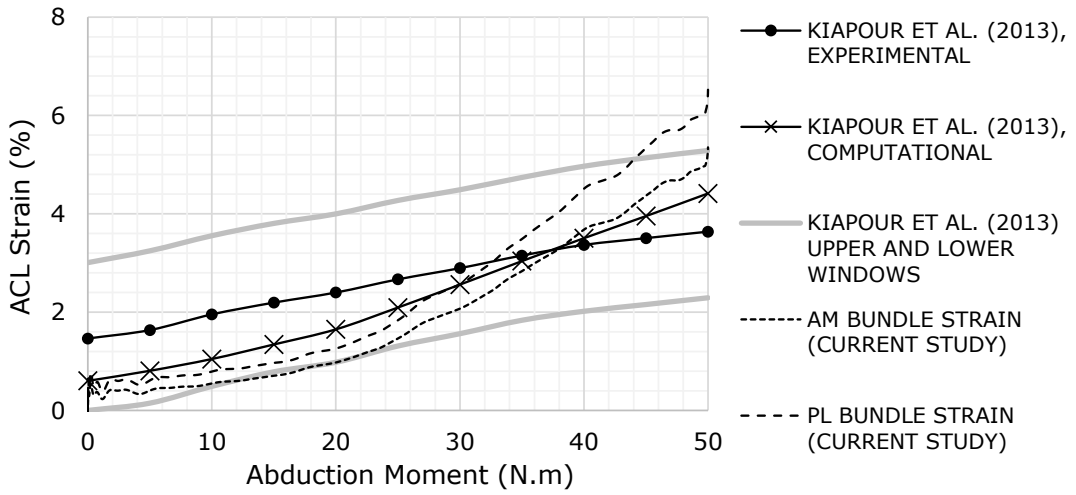

Figure 4.5: ACL strain during pure abduction

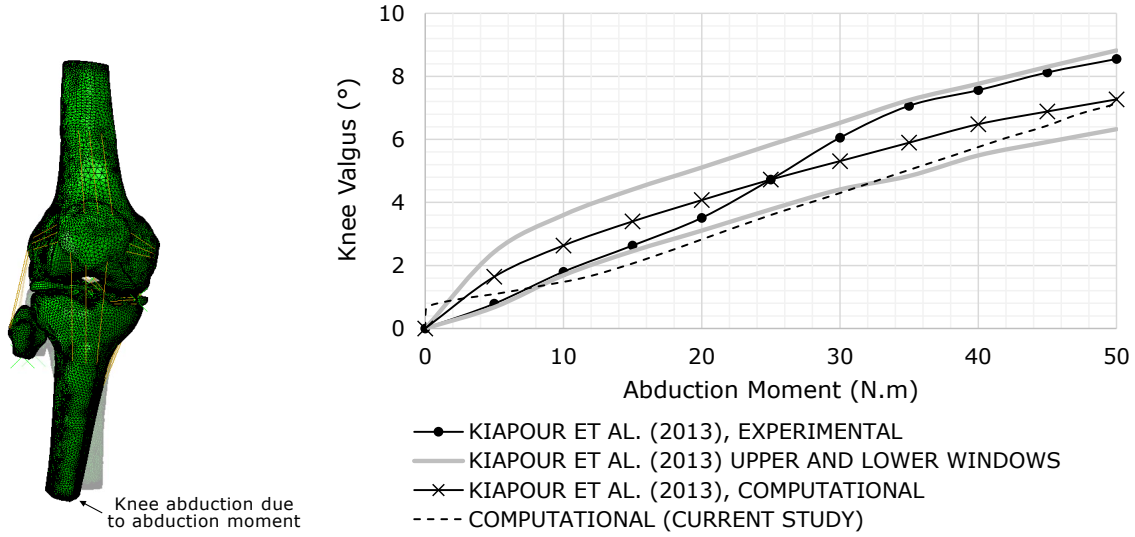

Figure 4.6: Knee valgus rotation during pure abduction

4.3 Single-Leg Jump Landing Simulations

4.3.1 Moment Arms

Moment arms of all the applied muscle forces were calculated, as described in Section 3.2.2. The moment arm values measured during the experiment and in the FE model are reported in Table 4.2.

Table 4.2: Experimental and computational muscle moment arms of the specimen

Moment arm in	Quadriceps (mm)	Hamstring (mm)	Gastrocnemius (mm)
Experiment (Polak (2019))	48	28	18
Current FE model	48	31	20

4.3.2 Verification of Model Inputs

To verify the correctness of FE model kinematics during jump landing simulation, the flexion angle versus time curve of P1 participant profile, from the FE model, was plotted against the OpenSim output of Bakker et al. (2016) study (Figure 4.7). In OpenSim, the knee joint is treated as one of the inbuilt custom joint types (such as a hinge joint) in the software, whereas in the FE model, the knee joint involves complex tibiofemoral interactions. As a result, differences could be observed in the knee flexion angle output from OpenSim and the FE model.

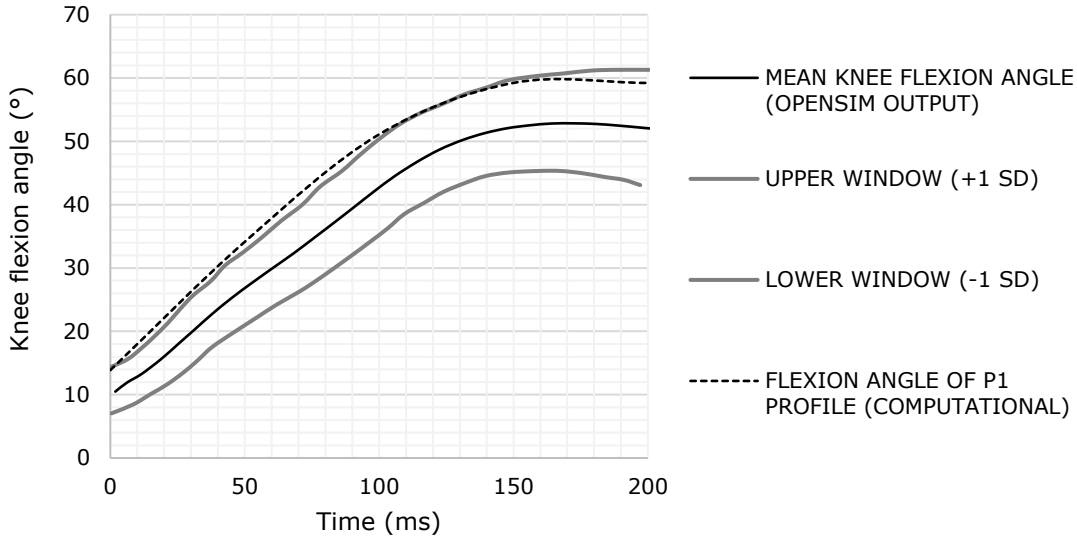

Figure 4.7: Verification of model kinematics of P1 profile with OpenSim output

Similarly, to verify the kinetics during the simulation, the muscle forces from the FE model were compared to the input muscle forces and hip moment from OpenSim (Figure 4.8). Appendix A shows similar curves for participant profiles P2 − P10.

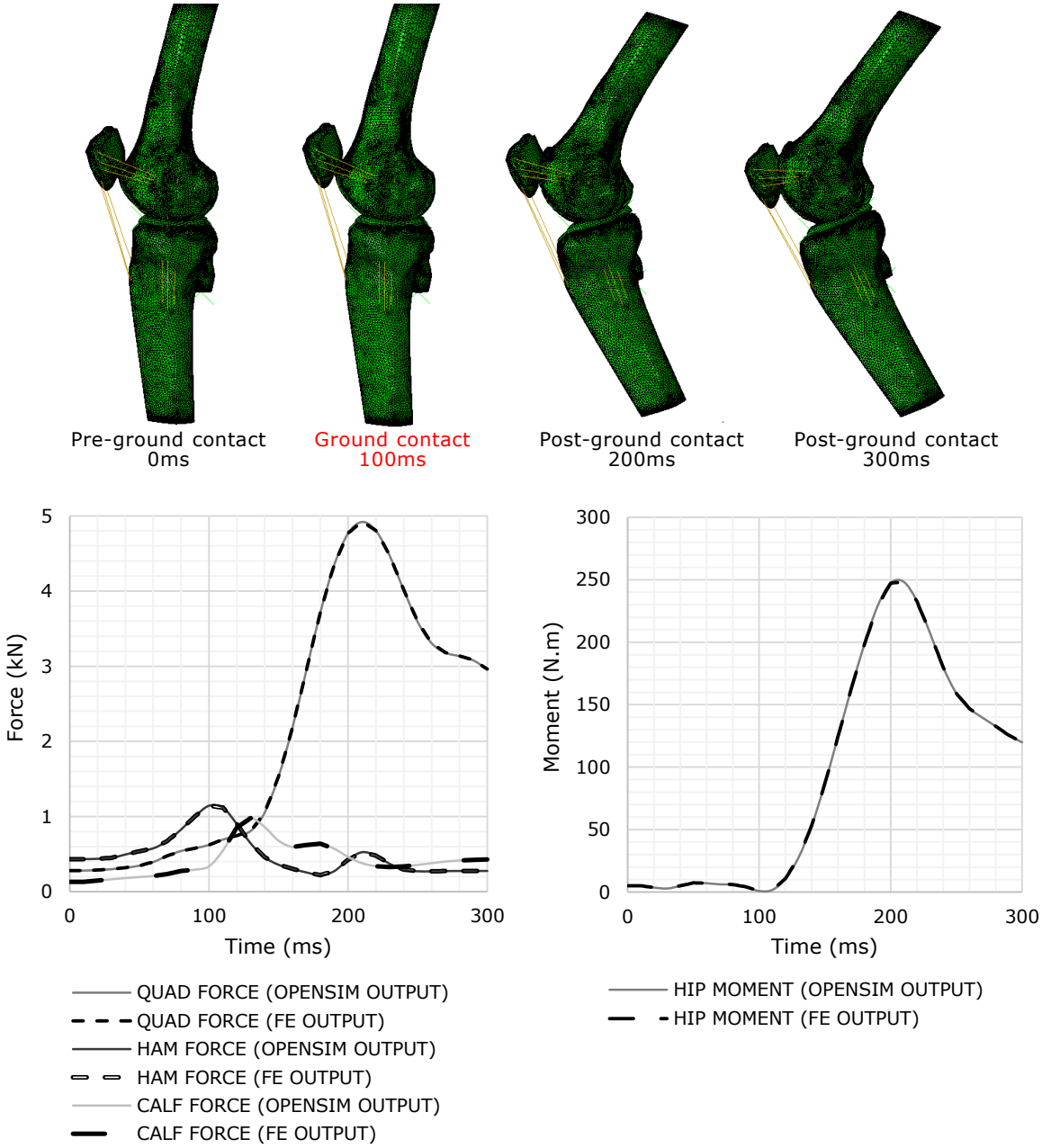

Figure 4.8: Jump landing stages (top) and verification of model kinetics (bottom)

4.3.3 Half Muscle Force Jump

ACL Strain

Half muscle force jumps of two participants, P5 and P6, from the study of Polak (2019) were simulated. The relative ACL strain during the half muscle force jump landing simulation of

both profiles is presented in Figure 4.9. The strain plot also shows the *in-vitro* half muscle force jump landing simulations of Polak (2019) of the same specimen as the subject-specific model.

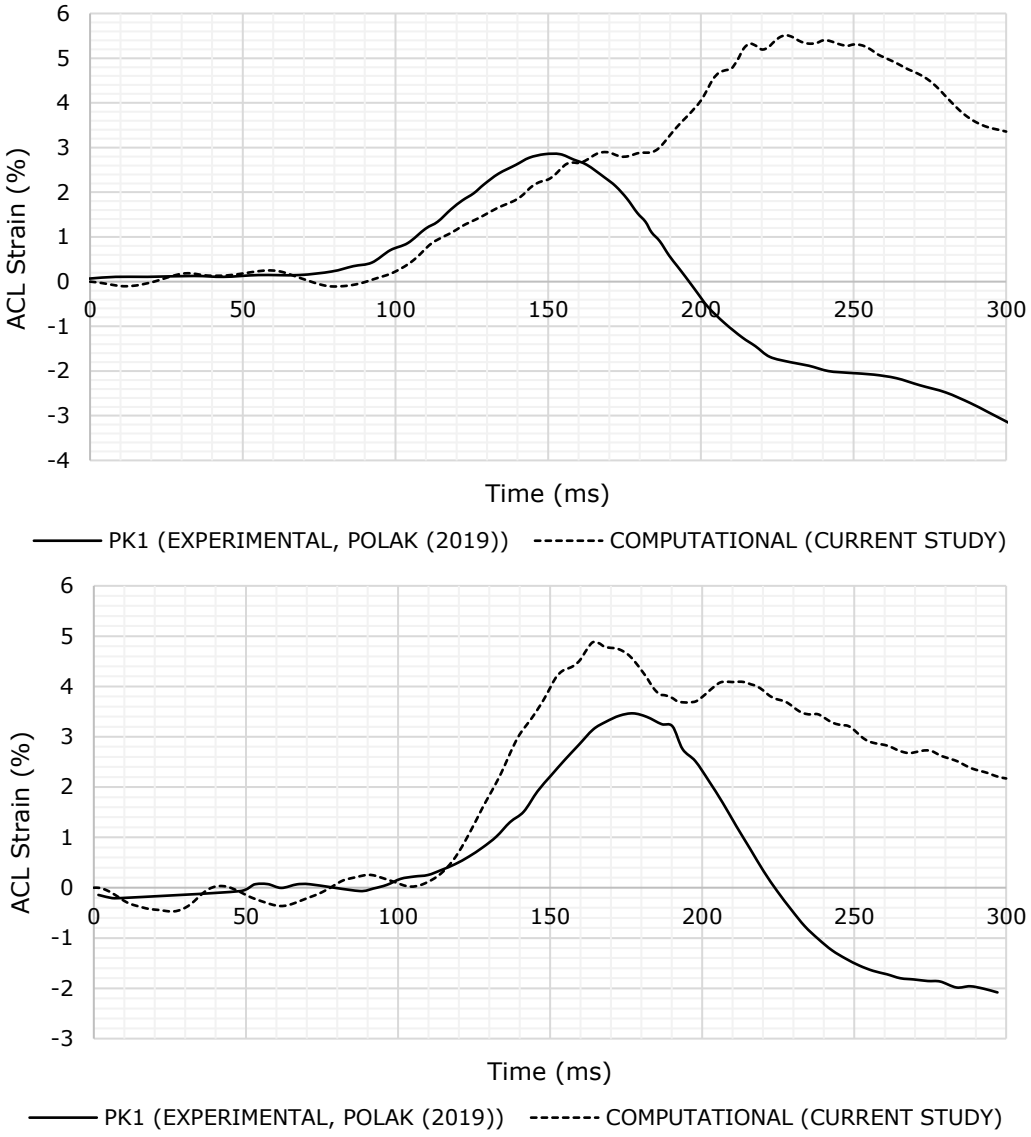

Figure 4.9: Relative ACL strains during half muscle force jump landing
Participant profiles P5 (top) and P6 (bottom)

Figure 4.10 shows the maximum relative ACL strain measured in the simulation and the time taken to reach the peak strain value during participant profiles P5 and P6 jump landings, in comparison with those from the experimental study.

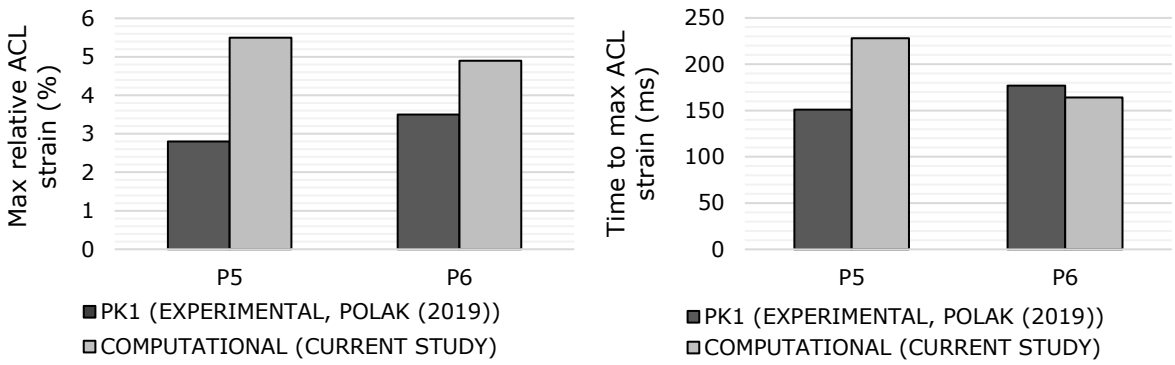

Figure 4.10: Comparison of peak and time to peak ACL strain in half muscle force jump landing

Comparison of the computational strain data of both the profiles, P5 and P6 with the experimental values (from Polak (2019)) were made using RMSE and Pearson correlation coefficient metrics. Table 4.3 shows the RMSE and Pearson correlation coefficient values during half muscle force jump.

Table 4.3: Comparison of experimental and computational ACL strains

Participant profile	RMSE	Pearson correlation coefficient (r)
P5	3.9	−0.52
P6	2.0	0.60

Medial Meniscus Strain

A comparison of the meniscal strain during the half muscle force jump landing simulations of P5 and P6 profiles is shown in Figure 4.11.

4.3.4 Full Muscle Force Jump

ACL Strain

Full muscle force jumps of the ten participants from the study of Bakker et al. (2016) were simulated. The relative ACL strain during the full muscle force jump landing simulation of participant profile P1 is presented in Figure 4.12. The strain data is compared with the *in-vitro* full muscle force jump landing results of the same participant profile, P1, from the study of Bakker (2015), where five cadaver knees were tested. The strain values are reported after the ground contact, during the last 200 ms of the jump landing.

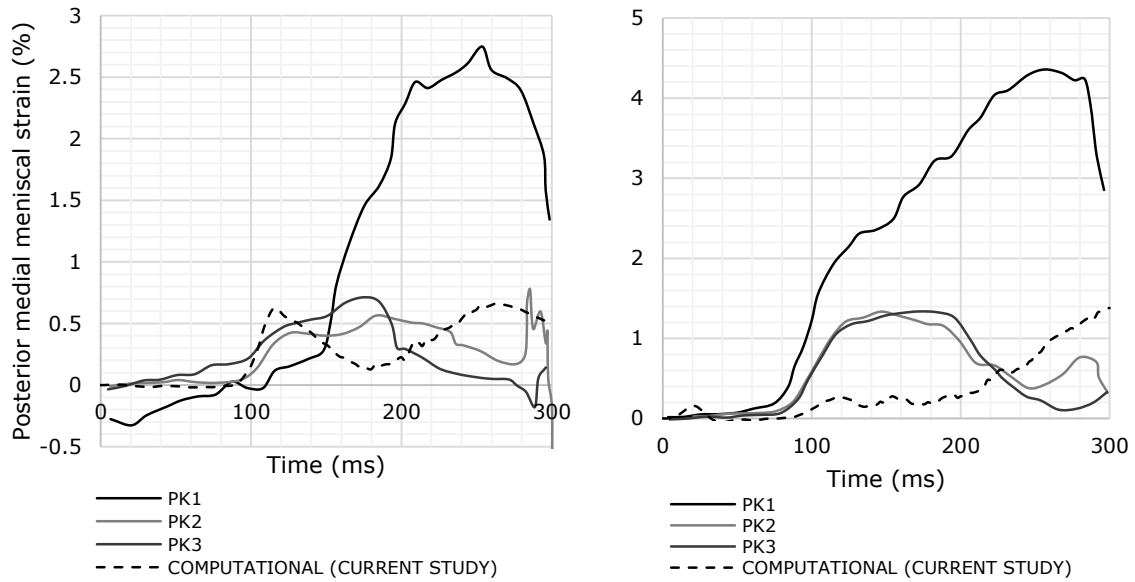

Figure 4.11: Posterior medial meniscal strains during half muscle force jump landing Participant profiles P5 (left) and P6 (right)

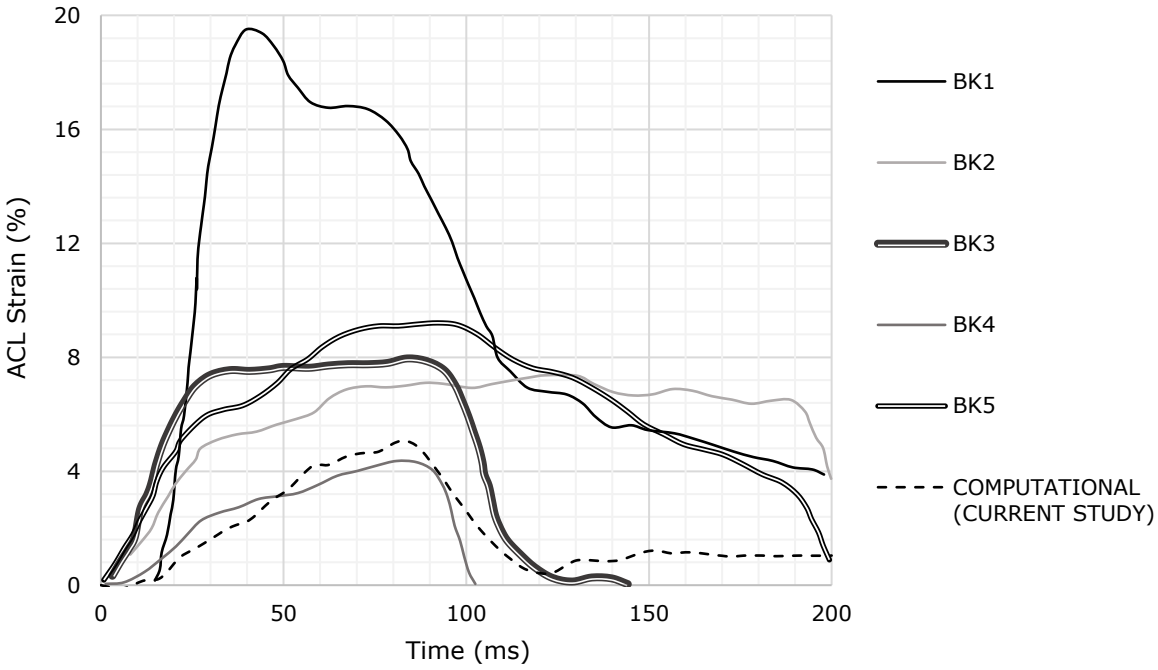

Figure 4.12: Relative ACL strains during full muscle force jump landing of P1 profile From the current study (broken line) versus *in-vitro* experimental strain of five cadaver specimens (Bakker, 2015) (solid lines)

Strain comparison plots of other participant profiles (P2 to P7) to Bakker et al. (2016)

in-vitro results can be found in Appendix A. In Figure 4.12, an interesting thing to note is the strain experienced by the specimen BK1 (19.6 %), which is several times larger than the strains in the other specimens. BK1 consistently showed larger strains in all the participant profiles (Appendix A). The large strain values of BK1 were attributed to the high posterior tibial slope of BK1 (22.1°) compared to other specimens (3.5° to 12.6°) (Bakker et al., 2016). The computational relative ACL strain trends of all the participants profile jumps, P1 to P10 are shown in Figure 4.13.

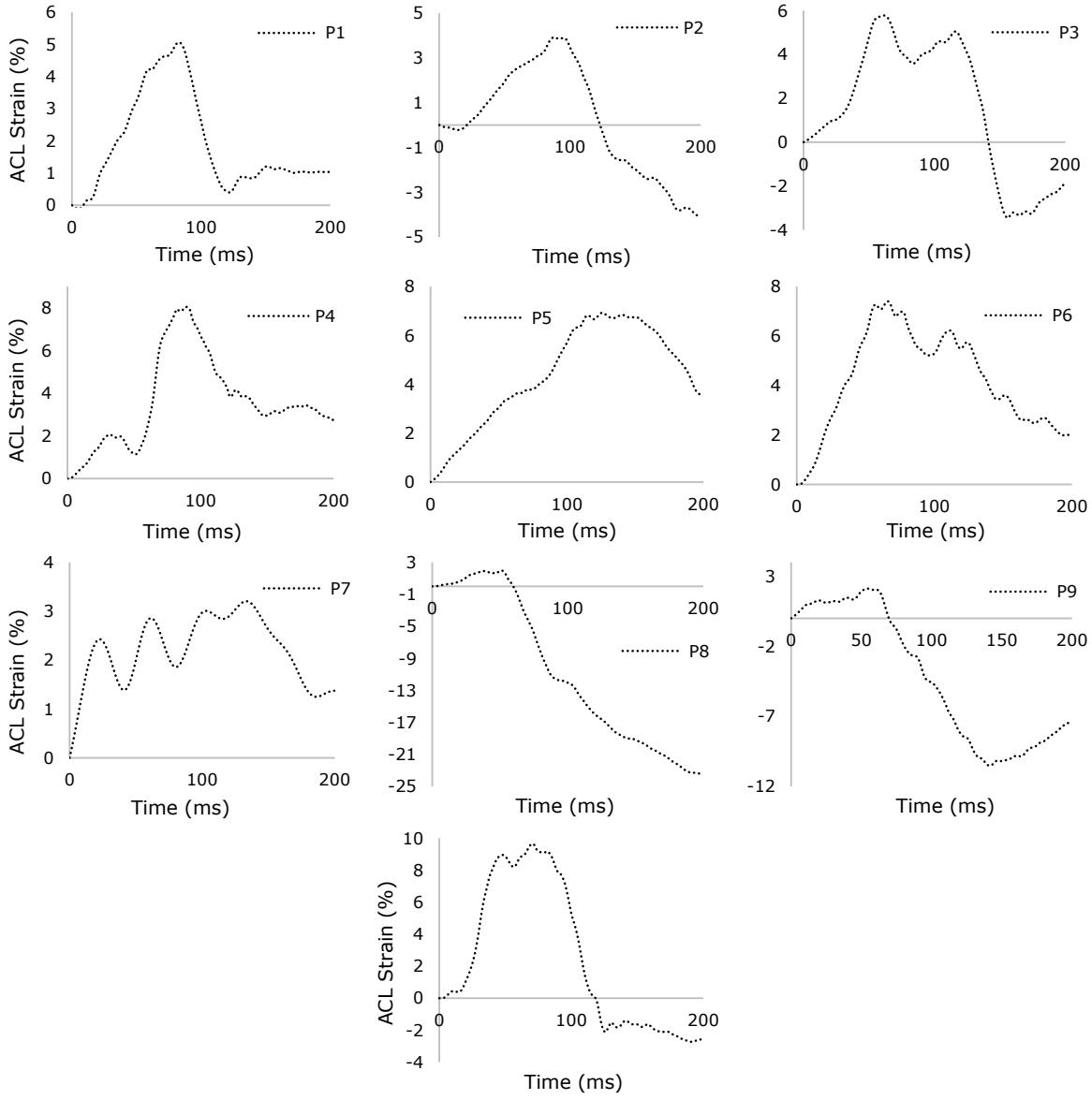

Figure 4.13: Computational ACL strains
(during full muscle force jump landings of P1 − P10 participant profiles)

Table 4.4 shows the maximum relative ACL strain measured in the simulation and the time taken to reach the peak strain value, after the ground contact.

Table 4.4: Peak and time to peak ACL strain of P1 − P10 participant profiles

	P1	P2	P3	P4	P5	P6	P7	P8	P9	P10	Average	Std. Dev.
Peak ACL strain (%)	5.1	3.9	5.8	8.0	6.9	7.4	3.2	1.9	2.1	9.6	5.4	2.6
Time to peak ACL strain (ms)	82	88	62	90	126	66	134	50	54	70	82	29

In the study of Bakker et al. (2016), jumps of only seven participant profiles (P1−P7) could be performed due to unsuccessful jump landing trials in some cadaver specimen. Figure 4.14 shows the comparison of computational ACL strains with the results from those seven participant profiles.

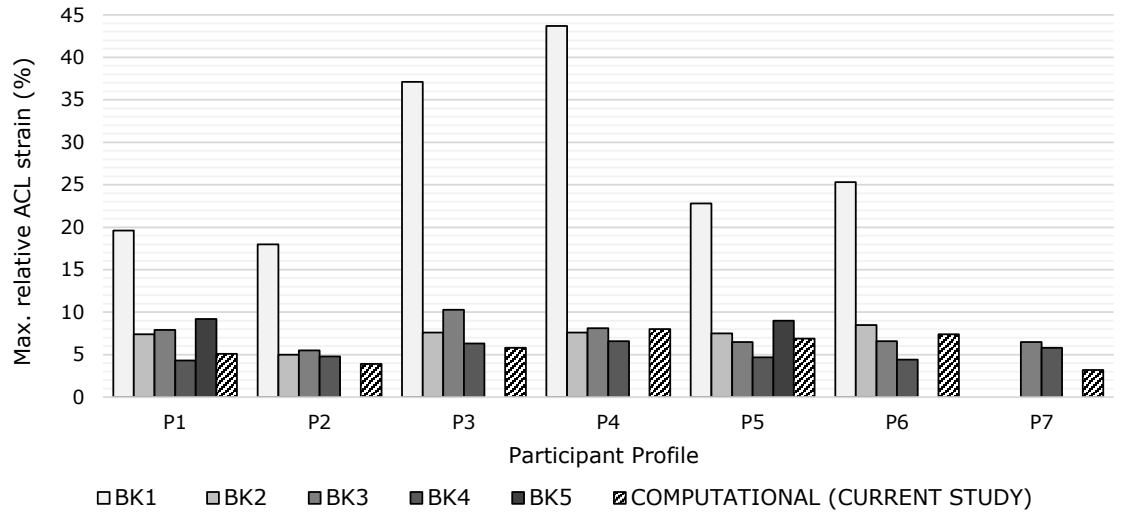

Figure 4.14: Comparison of peak ACL strains in P1 − P7 participant profiles
Peak ACL strains from the *in-vitro* study (Bakker et al., 2016) (Solid) are compared with those from the computational study (Hatched). Gaps between bars are the unreported strain values due to failure of that knee specimen during the experiments.

Medial Meniscus Strain

During the full muscle for jump simulations, the posterior medial meniscal strain was also measured as per the procedure described in Section 3.2.3. All ten meniscal strain trends are shown in Figure 4.15, and the peak meniscal strain values are listed in Table 4.5.

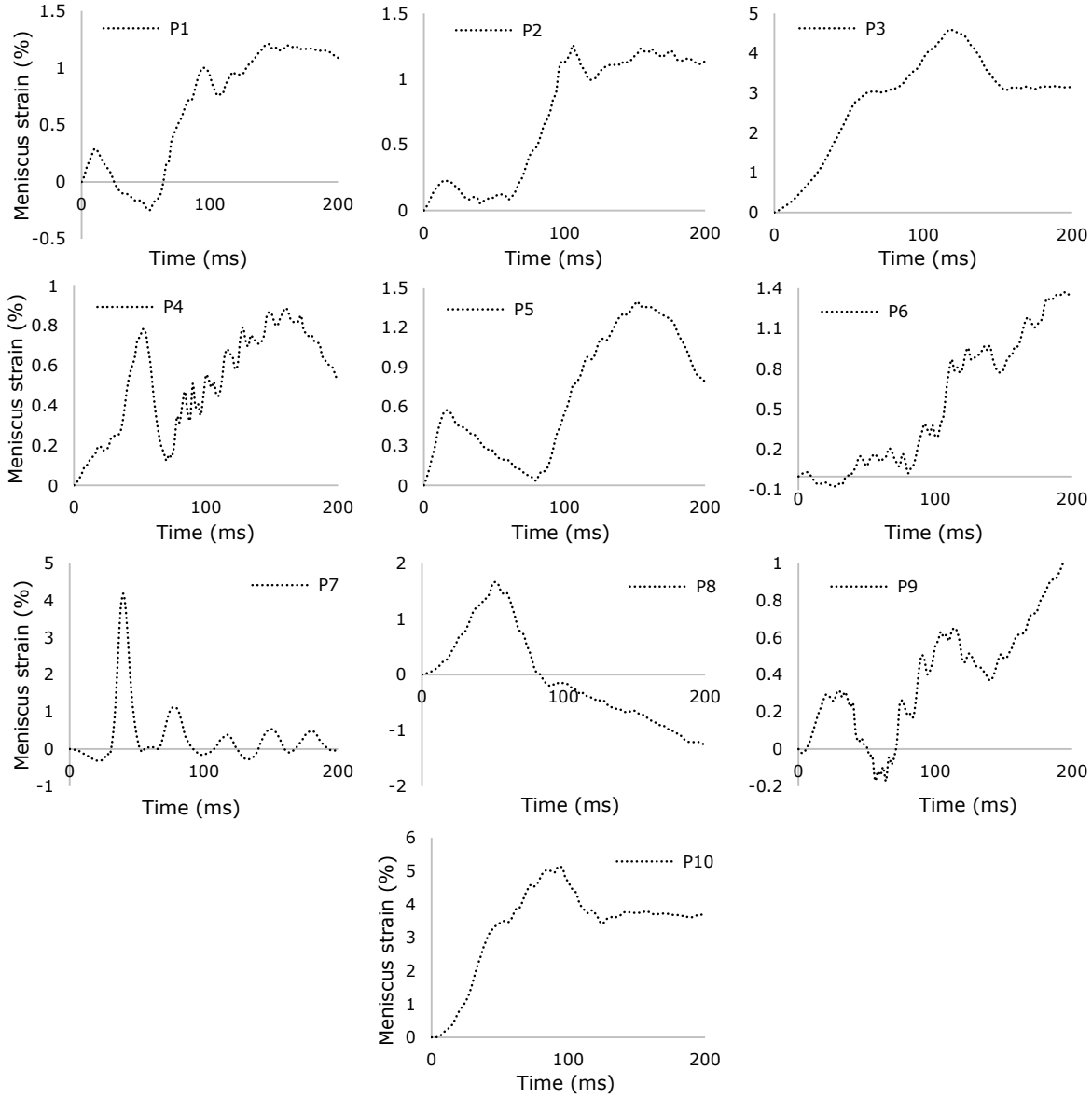

Figure 4.15: Computational posterior medial meniscal strains
(during full muscle force jump landings of P1 − P10 participant profiles)

Table 4.5: Peak posterior medial meniscal strain of P1 − P10 participant profiles

	P1	P2	P3	P4	P5	P6	P7	P8	P9	P10	Average	Std. Dev.
Peak meniscal strain (%)	1.2	1.3	4.6	0.9	1.4	1.4	4.2	1.7	1.1	5.1	2.3	1.6

4.3.5 Energy Balance

Energy balance in a finite element simulation ensures that the analysis obeys the law of conservation of energy. For the successful completion of an FE simulation, oftentimes artificial energies such as hourglass, viscous and mass scaling energies are added to the system; these should be only a small percentage of the total energy of the system to ensure that the physics of the system remain realistic (Burkhart et al., 2013).

The energy balance in the single-leg jump landing simulation of one of the participant profiles is presented in Figure 4.16. In Abaqus, the energy balance is governed by the equation,

$$E_{TOTAL} = E_I + E_{VD} + E_{FD} + E_{KE} - E_W = Constant$$

E_I is the internal energy of the model which includes elastic, inelastic and all artificial energies, E_{VD} and E_{FD} is the viscous and frictional dissipation energies, E_{KE} is the kinetic energy and E_W is the external work done during the simulation. E_{TOTAL} is the algebraic sum of the energies which is close to zero during the simulation, showing that the energy of the system is conserved.

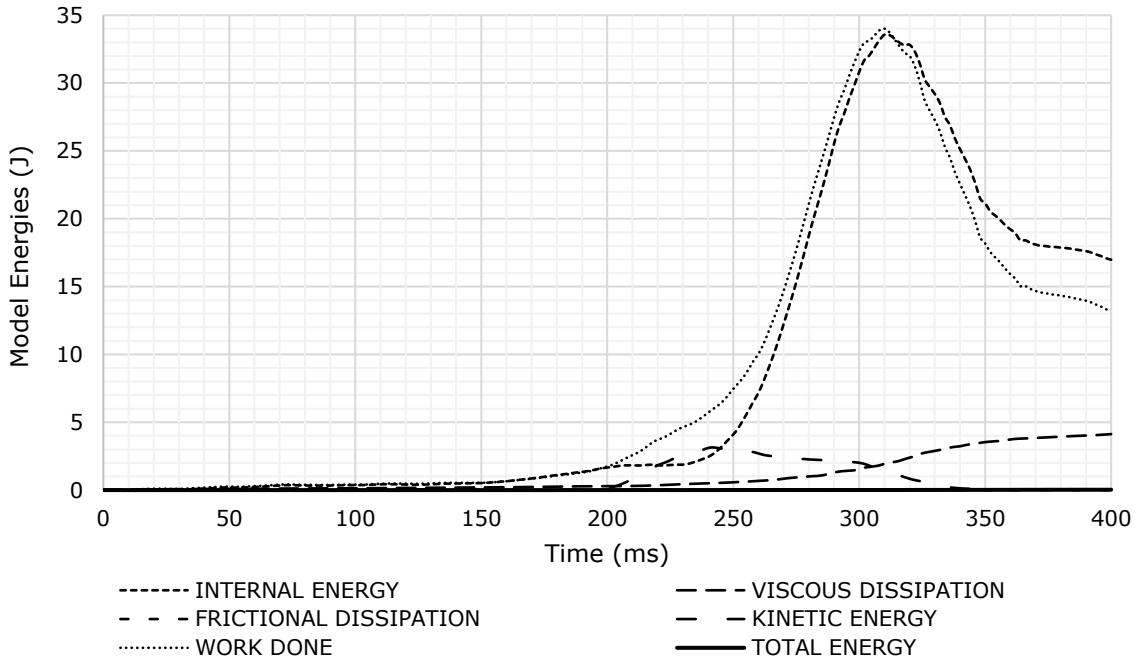

Figure 4.16: Model energies during jump landing simulation of P1 participant profile

Chapter 5

Discussion

The primary purpose of the current study was to develop a subject-specific FE model of the knee joint to simulate a dynamic loading scenario - a single-leg jump landing. This was a one of a kind study wherein high-quality meshes for soft tissues, and accurate locations of ligament insertion sites were incorporated in a subject-specific FE model to investigate jump landing motion involving dynamically varying muscle forces and hip flexion moment.

The FE model was developed by segmenting the medical images of the knee joint to generate 3D tissue geometries. The 3D models of the tissues were meshed with high-quality tetrahedral and hexahedral elements, and appropriate material properties were assigned from literature. The ligament insertion sites on the cadaver specimen were accurately modelled using digitization technique. Kinematics of the knee model was verified in the three anatomical planes with data from the literature. Dynamic muscle force profiles with hip and ankle kinematic data of ten participant profiles from the study of Bakker et al. (2016) served as the input to the model. The FE model successfully replicated the sagittal plane mechanics based on comparison to experimental data collected on the dynamic knee simulator.

5.1 Finite Element Model Development

Segmentation

Segmentation of CT and MRI scans is the standard approach to develop 3D geometry of knee anatomy. Automatic and manual segmentation methods have been used to develop 3D models of the knee joint. However, soft tissues of the knee joint have similar greyscale intensities in an MRI scan and are therefore challenging to segment using automatic segmentation methods (Aprovitola and Gallo, 2016).

In the current study, a previously segmented model of the knee joint, SPL 2015 Sep, was used as a reference for segmentation which aided the identification of soft tissue regions

and bone-cartilage interfaces. An intensity-based automatic segmentation method called thresholding was used to segment bone geometries, whereas cartilage and menisci regions were segmented manually. In this study, a single subject-specific model was developed, and hence, sophisticated algorithms were not used or developed for segmentation.

Mesh Generation

Accurate representation of tissue geometries as a meshed structure is critical for FE modelling. Different meshing strategies were employed to mesh the knee tissue geometries. Bony tissue is stiffer compared to other soft tissues in the knee joint and hence were modelled as rigid bodies and were meshed using tetrahedral elements in HyperMesh software. Similar approaches were employed in previous computational studies to represent bones in an FE model (Ali et al., 2017; Kiapour et al., 2013; Harris et al., 2016). This approach could also be a limitation of this study since the deformation of the bones due to the forces involved in the jump landing simulations were not captured.

Cartilage and menisci were meshed with hexahedral elements, as they undergo large deformations. Different meshing approaches were employed to mesh the cartilage and menisci structures, depending on the ease, quality of the mesh output and the capability of the software used. All the cartilages of the knee joint were meshed using multi-block meshing approach in IA-FEMesh software. Menisci were meshed using a custom software by Rodriguez-Vila et al. (2017), which functions similar to the multi-block meshing process. The hexahedral elements were evaluated against different mesh quality metrics and were of high quality (Figure 4.1). More than 83 % of the elements in cartilage meshes exceeded the minimum required quality criteria. Due to the inherently curved structure of the menisci, the aspect ratio and internal angle requirements were met only by 65 % of the elements. However, 97 % of the menisci elements had jacobian greater than 0.6, and all the elements had warpage less than 15°.

Material Properties

Realistically, all the knee soft tissues exhibit anisotropic, non-linear behaviour under loading. A few studies have implemented complex anisotropic hyperelastic models including poroviscoelastic features to describe cartilage and menisci behaviour previously (Dabiri and Li, 2013; Halonen et al., 2016; Orozco et al., 2018). However, in many computational models of the knee joint, where the focus of the study was on the ligament mechanics, linear isotropic properties were assigned (Beillas et al., 2007; Kiapour et al., 2013). Similarly, in the current study, isotropic, linear elastic material properties were assigned to the cartilages and menisci from published data.

In the current study, the ligaments of the knee joint were not segmented from the MRI scans. Ligaments were instead modelled as non-linear spring elements, which only required the location of their insertion on the bones. This approach enabled quicker development of

the subject-specific FE model. Several computational FE models have defined ligaments as non-linear springs. In some studies, the stiffness and pre-strain values obtained from the literature were optimized based on experimental laxity tests on the acquired cadaveric specimens (Harris et al., 2016; Beidokhti et al., 2017) whereas in others the properties from literature were directly used (Bloemker et al., 2012; Zielinska and Haut Donahue, 2006). In the current study, only the ACL material behaviour was adopted from the experimental study of Chandrashekar (2005) with the pre-strain values from the literature. For the other ligaments of the knee joint, literature data were used directly.

5.2 Kinematic Verification Studies

Before simulating the jump landing activity on the model, the kinematics of the model was verified with published literature data. During flexion, the AM bundle strain decreased slightly and plateaued while the PL bundle strain dropped significantly (Figure 4.2). Although similar trends were observed, it does not compare well with the *in-vivo* data of Beynnon et al. (1992a). However, the computational strain trends are consistent with the natural behaviour of the ACL. Under physiological conditions, the anteromedial bundle is tight in extension and stays tight with increasing flexion, while the posterolateral bundle becomes slack with the increase in flexion angles (Amis and Dawkins, 1991; Hollis et al., 1991) (Figure 5.1).

Strains during Lachman and anterior drawer tests compared well with the *in-vivo* test data by Beynnon et al. (1992a). An interesting thing to note in the strain data is that the loading and unloading curves of the ACL did not overlap, but instead exhibited hysteresis behaviour, even though viscoelastic properties were not assigned to ACL (Figure 4.4). The hysteresis behaviour was unexpected and could be attributed to the difference in the resistance experienced by the cartilage and menisci while the tibia travels anteriorly and posteriorly during the loading and unloading phases. However, the magnitude of the ACL strain compared well with the *in-vivo* experimental results.

In Figure 4.3, internal tibial rotation with flexion was compared with the computational and experimental trends of Kiapour et al. (2013). While the results of the previous work showed the maximum internal rotation angles to be less than 5°, in the current study, this value was 6.7°. The kinematics of the coronal plane are shown in Figure 4.5 and Figure 4.6. Knee valgus rotation and the ACL strain fit within the standard deviations of the experimental data, showing good agreement. However, from Figure 4.5, it is clear that the shape of the curve from the current study was different compared to the experimental study showing high ACL strains at high abduction moments. The variations in the data could be due to variability in anatomical features between the specimens. Besides, Kiapour et al. (2013) modelled the ligaments as solid elements and included additional stabilizing ligaments such as capsular ligaments which were absent in the current study, possibly resulting in different kinematics. In addition, in the current model, MCL was modelled

with superficial MCL fibres with the deep fibres absent. Also, the MCL spring elements were connected between the nodes on the femur and the tibia without simulating the wrapping of the ligament over the bones which might be responsible for the different shape of the curve in comparison with the experimental data.

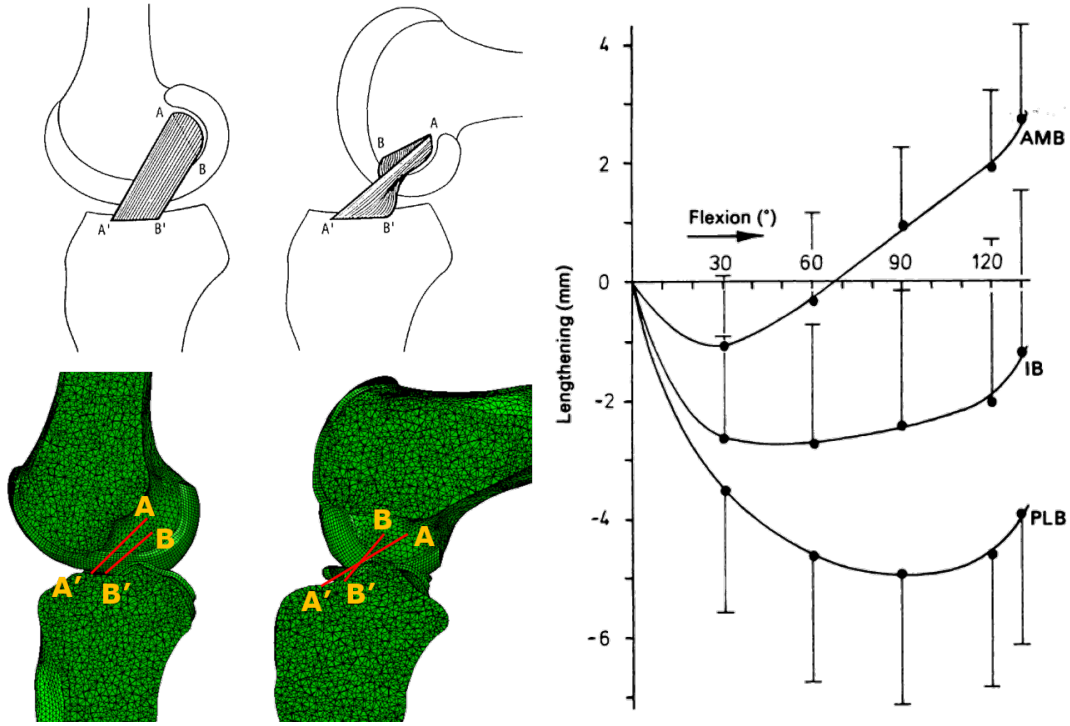

Figure 5.1: ACL lengthening during flexion
AA' and BB'represents AM and PL bundles of ACL, adapted from Girgis et al. (1975)(top left). Orientation of AM and PL bundles of ACL in the FE model of the current study (bottom left). Graph showing lengthening of different ACL bundles. AMB: anteromedial, IB: intermediate, PLB: posterolateral bundles, adapted from Amis and Dawkins (1991) (right)

5.3 Single-Leg Jump Landing

5.3.1 Half Muscle Force Jump

ACL Strain

Jump landing simulations of participant profiles P5 and P6 were simulated with half muscle forces to compare the ACL strain with the experimental data from Polak (2019). From Figure 4.9, until 150 ms, the computational ACL strains agree well the experimental data. But, beyond 150 ms, strong correlations were not found between them. While the computational peak strains occurred between 80 - 200 ms as observed in the experiments,

large variations were found in the strain trends of P5, but the strain trends of P6 matched slightly better with the experimental data (Figure 4.9). The computational relative peak ACL strain values of P5 profile were almost twice the values found experimentally, and the time to peak strain was 77ms apart (Figure 4.10). The computational relative peak ACL strain of P6 profile was 40 % higher than the experimental value; however, the peak strain occurred around the same time during the simulation (Figure 4.10).

RMSE and Pearson correlation coefficient comparing the experimental and computational strains during half muscle force jump shows the results of P6 profile jump correlated better (+ 0.6) with the experimental strain values (Table 4.3). Additionally, the RMSE was also smaller (2 %) compared to P5 profile jump (3.9 %). Moreover, P5 profile jump results indicated a negative correlation (− 0.52) with the experimental data wherein, after 150 ms into the jump, the experimental strain decreased, but the computational strain increased.

The difference in the peak strain could have arisen due to the differences in the location of measurement of strain in the experiment and in the modelling of the ligament behaviour itself. Yamamoto et al. (1998) found that the strains in the ACL closer to the insertion sites (on the femur or the tibia) are lesser than in the mid-section. In the experimental study of Polak (2019), on the cadaver specimen, the DVRT to measure ACL displacement was sutured slightly inferior, close to its tibial attachment (Figure 2.9), while the computational values are the strains of the entire ligament bundle (non-linear spring) which might have caused the difference in the strain values. Besides, the material properties of the ligament bundle in the computational model were not subject-specific, which could be another reason for mismatch in the strain data. Furthermore, the cadaver specimen did not sustain full muscle force jump landing trials, which limited data comparison.

However, the strain trends for the same profiles, P5 and P6, during the full muscle force jump landing simulations showed good agreement with the experimental data of Bakker et al. (2016). Although statistical comparisons were not made between the data, the strain trends and the location of the peak strain compare well with the experimental results of Bakker et al. (2016) (Figure 5.2). Moreover, Bakker (2015) inferred that the occurrence of peak ACL strain might coincide with the peak value of quadriceps force. In the full muscle force cadaveric experiments of Bakker et al. (2016) with P5 profile, peak ACL strain occurred at 250 ms (or at 150 ms after ground contact), which agrees well with the computational peak strain occurring at 228 ms.

Medial Meniscal Strain

In addition to ACL strain, Polak (2019) recorded posterior medial meniscal strains during jump landing experiments under half and full muscle force conditions. It is evident that the meniscal strain trends of PK1 and the FE model were different during half muscle force jump landing (Figure 4.11). However, in PK2 and PK3 specimens, the meniscal strains were 0.8 % and 0.7 % and had consistent trends, different from that of PK1. The difference

in experimental strain trend of PK1 compared to PK2 and PK3 could point to an error in the data collection due to instrumental artefacts, or the DVRT might have encountered an obstruction during the experiment involving PK1, resulting in higher strains. This notion is strengthened by the fact that PK2 and PK3 also showed lesser strains with P6 profile. The computational meniscal strain trend of P5 profile compared well with the experimental strain trends of PK2 and PK3 specimens (experimental average: 0.75 %; FE model: 0.7 %). The computational meniscal strain trend of P6 profile did not compare well with the experimental strain trends of PK2 and PK3 specimens, but the peak strain values (experimental average: 1.3 %; FE model: 1.4 %) agreed well and occurred at different times post ground contact (Figure 4.11).

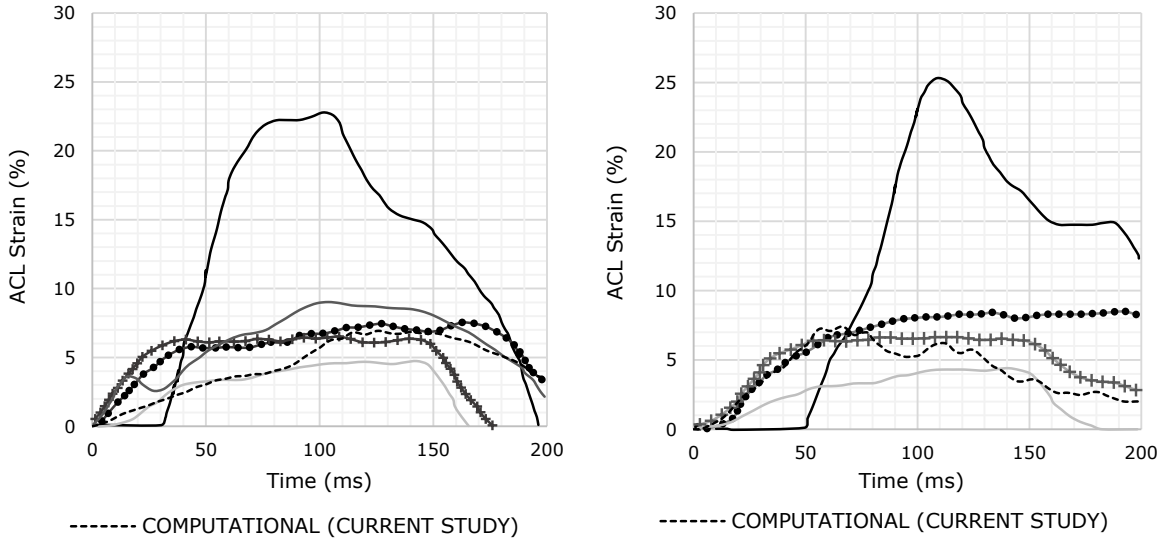

Figure 5.2: Relative ACL strains of P5 (left) and P6 (right) jump landing profiles Computational (dashed line) versus *in-vitro* experimental study (Bakker, 2015) (solid lines)

The variations in strain trends from the FE model and PK2, PK3 experimental results could be due to the definition of menisci in the FE model. Menisci in the FE model were defined as isotropic materials whereas they exhibit transversely isotropic behaviour; stiffer in the circumferential direction and exhibit similar properties in the axial and radial directions (LeRoux and Setton, 2002). Moreover, Guess and Razu (2017) simulated a passive leg motion on a computational model and showed that the deep fibres of the MCL (dMCL) and peripheral tibiomeniscal attachments influence the deformation of the medial meniscus. In the current study, the attachment of the dMCL fibres to the medial meniscus was not modelled. The menisci are firmly attached to the tibia by tibiomeniscal coronary ligaments which were also not modelled.

While the current study did not focus on meniscal injury mechanics, the results show that the current FE model outputs reasonable values of strain. Appropriate model definition could resolve the variations between the results from experiments and FE model.

5.3.2 Full Muscle Force Jump

In the *in-vitro* study of Bakker et al. (2016), different strain trends were observed when the same cadaver specimen was subjected to jumps with different participant profiles and when the same participant profile was applied on different cadaver specimen. The variation was attributed to the distinct landing strategies used by the participants involved in the motion capture. Similarly, different strain trends were observed when the subject-specific model was simulated with different landing profiles (Figure 4.13).

ACL Strain and Peak ACL Strain

Peak ACL strain and the time to reach peak strain (or strain rate) are identified as the critical factors affecting ACL injury (Bakker et al., 2016). Hence, these values from the FE simulation were compared to other experimental and computational studies of jump landing.

In addition to the half muscle force jumps, Polak (2019) also performed experimental full muscle force jumps. However, out of the three knee specimens acquired for the study, only one specimen, PK2, sustained the full muscle force jumps of P5 and P6 profiles. On PK3, only P5 jump could be performed before failure. Comparison of peak ACL strain from the current study with the experimental and computational data (from GHBMC model) of Polak (2019) is shown in Figure 5.3. In Polak (2019)'s study computational strains of 4.2 % and 13.9 % were reported with P5 and P6 profiles, which were higher than the recorded experimental values of 3.2 % and 6.2 %. The computational strains from the current subject-specific model with the same jump landing profiles also had higher strains compared to the experimental values (6.9 % and 7.4 %), but lower than the GHBMC model strains.

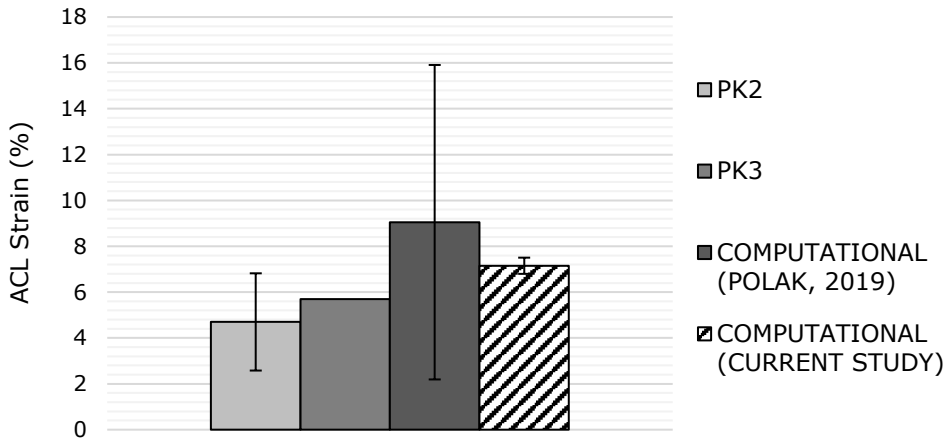

Figure 5.3: Comparison of peak relative ACL strains (Polak (2019) and current study)

Peak strains from the current study were also compared with the experimental strains from Bakker et al. (2016). Out of the five specimens tested by Bakker et al. (2016), the BK1 specimen showed much higher strains than the other specimens and was excluded from the statistical analysis of the study. Besides, due to the failure of cadaver specimens during the experimental study, all the ten jump landing profiles (P1 to P10) could not be executed (Table 3.7). Most of the specimens performed six profiles, P1 - P6, successfully and the seventh profile, P7 could be executed on two specimens only. P8, P9 and P10 profiles were not executed during the experiments. Therefore, the computational strains of the current study of P1 to P7 profiles only are compared with the experimental results of Bakker et al. (2016) (Figure 5.4). It was previously hypothesized that the strain trends from the seven participants profiles (P1 - P7) would be similar to Bakker et al. (2016) study, which was found to be true.

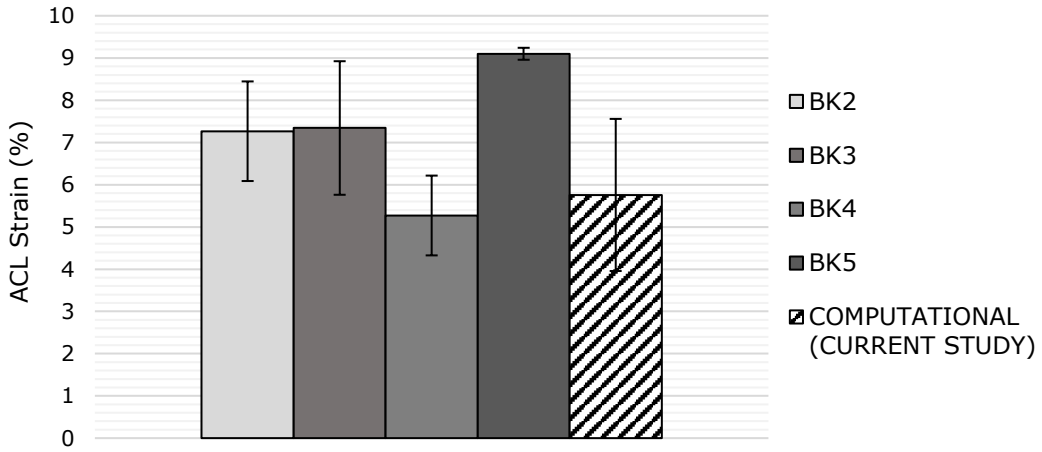

Figure 5.4: Comparison of peak relative ACL strains (Bakker et al. (2016) and current study)

While Cassidy et al. (2013) and Hangalur et al. (2016) conducted jump landing experiments on the DKS, only one cadaver specimen was tested in both studies, and the mean peak relative ACL strain was recorded as 4.3 % and 20 % respectively. The average strains from the current FE model fit well within that window. With the DKS at the University of Waterloo being an exception, no other existing knee simulators are capable of simulating jump landing with dynamic muscle force curves. Therefore, a one-to-one comparison of strains cannot be made due to different input conditions. Experimental research on jump landing by other groups was discussed in Section 2.3. The research group at the University of Michigan, simulated jump landing on eleven cadaver specimens by dropping a 150N weight on the femur (Withrow et al., 2006). A relative average peak ACL strain of 3 % was recorded during the experiments. Shin et al. (2007) successfully replicated the experimental study by Withrow et al. (2006) on a multibody dynamics model and found similar peak ACL strain (2.13 %) as the experimental values. These values are lower than the strains obtained from the experiments on the DKS. Application of dynamic muscle forces could be a reason for higher strain values from the studies conducted on the DKS (Polak,

2019). In addition, Woo et al. (1991), characterizing the structural properties of the ACL, found that the properties such as the linear stiffness, ultimate load and the absorption of energy under tensile loading decrease significantly with the age of the specimen. Most of the specimens in Withrow et al. (2006)'s study were from people aged more than 70 years, while the mean ages of cadaver specimens procured for the experiments on DKS were 47 years, which could be another reason for lower strain values.

Hashemi et al. (2007) examined the role of quadriceps forces on ACL strain during jump landing experiments conducted on the Texas Tech University simulator. They reported relative peak ACL strain values of 9 %, 10.7 % and 11.6 % under varying quadriceps pre-tensions, concluding that the increase in quadriceps force is favourable under dynamic loads. These strain values are higher than the mean values from the current study.

Taylor et al. (2011) took an interesting approach to measure ACL strain *in-vivo* during jump landing on eight participants. With the aid of medical imaging and motion capture, they observed peak ACL strains of (12 ± 7) % before ground contact, and post-ground contact strain was found 5 % lesser. In the current study, including the experiments on the DKS, ACL strains peaked only after initial ground contact. However, the post-ground contact strain at 7 % (5 % lesser than pre-ground contact strain), is comparable to the peak strain values obtained in the current study.

Kiapour et al. (2013) conducted cadaveric jump landing experiments on the Ohio State University simulator by dropping a weight on the foot equivalent to the GRF. Peak relative strains of (6.7 ± 1.8) % and 5.2 % were observed in the experimental and computational studies which agree well with the peak values of the current study, although the experiments did not include dynamic muscle forces. Figures 5.5 and 5.6 show a summary of the comparison of peak strain values from the present study with the existing experimental and computational investigations.

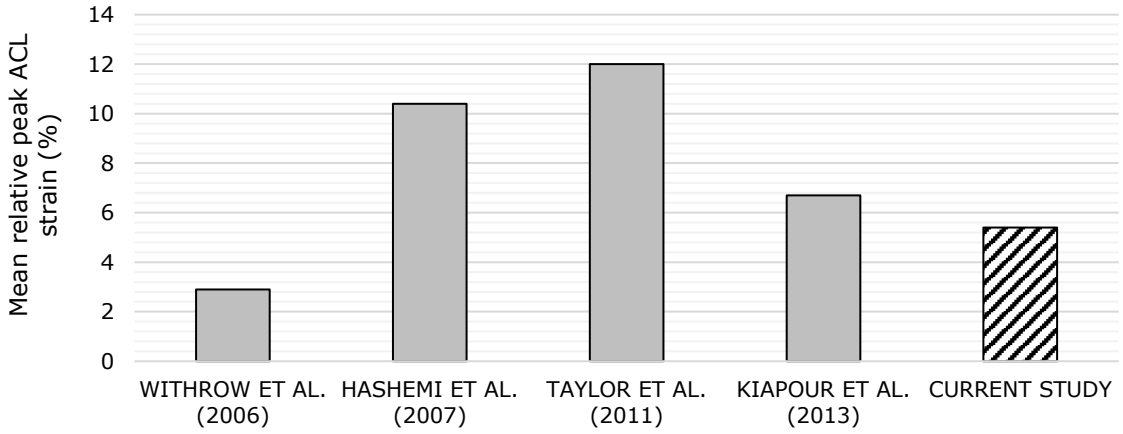

Figure 5.5: Comparison of mean peak ACL strain to other experimental studies

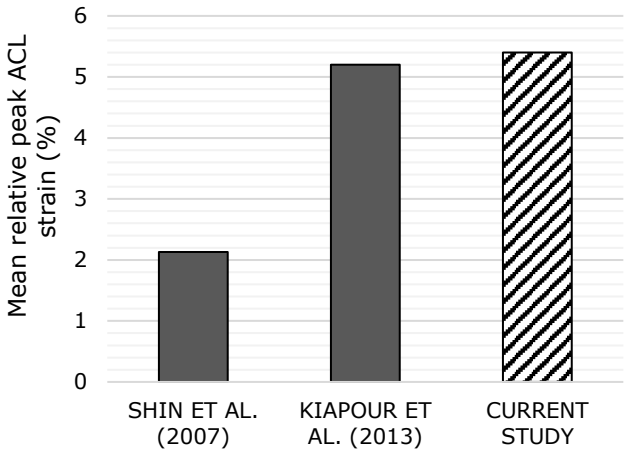

Figure 5.6: Comparison of mean peak ACL strain to other computational studies

Time to Peak ACL Strain

Considering the results of seven participant profiles in Bakker et al. (2016) study, most of the ACL strains peaked between 83 - 200 ms as reported. Two profiles, P3 and P6, showed peak strains at 62 ms and 66 ms after the ground contact. Upon observing the strain patterns of P3 and P6 profiles (Figure 5.7), it can be seen that the strain drops and increases again, and they have a second lower peak at 112 ms and 118 ms respectively, which fall within the predicted window, coinciding with the peaks of quadriceps forces (Appendix Figures A.2, A.5). Rapid development of ACL strain, which was also observed in the study of Bakker et al. (2016), was primarily attributed to the anatomic factors of the knee joint being tested. The earlier hypothesis that the peak ACL strains would be consistent with the experimental results of Bakker et al. (2016) was found to be true.

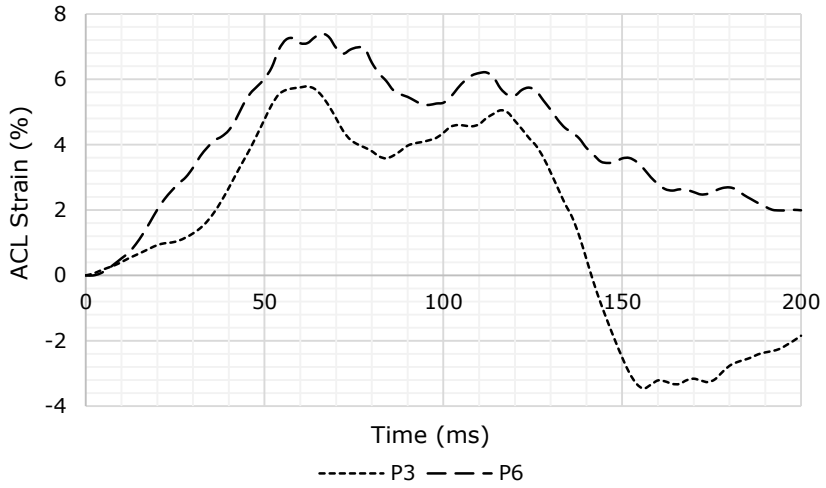

Figure 5.7: ACL strains during full muscle force jump landings of P3 and P6 participant profiles

In addition, P8, P9 and P10 participant profiles had peak strains occurring at 50 ms, 54 ms and 70 ms respectively. No experimental data were available to compare these peak occurrences from Bakker et al. (2016) study. However, it is still consistent with the studies of Hangalur et al. (2016), Hashemi et al. (2011) and Koga et al. (2010) where peak GRFs were observed earlier than 50 ms after ground contact, responsible for ACL injury.

Effect of Tibial Slope

Anatomic features of a subject play a significant role in determining ACL injury risk (Bakker et al., 2016). Posterior tibial slopes measured in the sagittal plane have been shown to increase ACL strain during jump landing (McLean et al., 2011) and also during activities involving large joint compression forces (Marouane et al., 2015). In the current study, medial and lateral tibial slopes were found to be 8.5° and 9° respectively. Hashemi et al. (2008) analysed the MRI scans of a cohort of 22 male subjects and reported mean tibial slopes of $(3.7 \pm 3.1)^\circ$ in the medial side and $(5.4 \pm 2.8)^\circ$ on the lateral side. In comparison, the medial and lateral slopes in the current study were found to be higher. However, these values were well within the range identified in McLean et al. (2011) $(7.6 \pm 2.1)^\circ$ and Giffin et al. (2004) $(8.8 \pm 1.8)^\circ$. Nevertheless, no quantitative relationship between posterior tibial slopes and ACL strain during dynamic activities has been established in the reviewed literature.

Chapter 6

Conclusions

6.1 Summary

The objective of the current study was to develop a subject-specific knee FE model to study the behaviour of the ACL during single-leg jump landing. With this objective, CT and MRI scans of a cadaver specimen were segmented to generate 3D models of bones and soft tissues in the knee joint. The segmented models were meshed with high-quality hexahedral elements, appropriate material properties were assigned, and finally, an FE model was set up in the commercial FE package, Abaqus CAE. Digitization technique was employed to accurately model the ligament insertion sites on the cadaver specimen. The kinematic responses of the model were verified by simulating basic knee motions in the three anatomical planes such as flexion, Lachman and anterior drawer tests, and pure abduction and the results were verified with published experimental data.

The necessary boundary conditions to simulate a jump landing were obtained from the work of Bakker et al. (2016). Initially, half muscle force jumps were simulated, and ACL strains and meniscal strains were compared to the experimental data from Polak (2019). Relative peak ACL strains were 5.2 % and 4.9 %, for participant profiles P5 and P6 during the simulation. While the computational ACL strain trend of P5 profile did not agree well with that of experimental data, the strain trend of P6 profile had a positive correlation, including the time to peak ACL strain. Posterior medial meniscal strains were also compared to the experimental data of Polak (2019). The computational meniscal strains from the half muscle force jumps did not compare well with the experimental results; however, the meniscal strain trends of two different cadaver knees tested in the study agreed well with the computational results. The cadaver specimen based on which the subject-specific model was developed, failed during the full muscle force jump landing experiment and hence no data was available for comparison of computational results.

However, based on the *in-vivo* motion capture data of Bakker et al. (2016), ten different participant profile jumps were simulated, and ACL strain was computed. The mean peak

relative ACL strain was (5.8 ± 1.8) % occurring at (82 ± 29) ms agreed with the average strain and the strain trends of the experimental studies of Bakker et al. (2016). In addition, the meniscal strains during the full muscle force jump landing simulation had a mean peak value of (2.3 ± 1.6) %.

To summarize, the avenue of developing a valid subject-specific computational model to simulate dynamic conditions of a single-leg jump landing event was explored in the current study. Reasonable predictions were obtained from the computational model that agreed well with the experimental results. The current study shows that, in the future, subject-specific FE models can be used to predict the risk of injury in dynamic loading scenarios, accounting for anatomic variabilities.

6.2 Limitations

There are recognized limitations associated with the current study, including:

1. The ligament attachment sites were accurately modelled using digitisation technique; however, the ligament slack-taut transitions and pre-strain values of the ligaments in the FE model were based on published population average values. A subject-specific model would be more accurate if the appropriate ligament properties from the subject were assigned. Nevertheless, the kinematic responses, including the ACL and meniscal strain results, were reasonable.

2. In the modelling of ligaments, except ACL, the kinematic responses of other ligaments in the knee joint were not verified. The response of the PCL also contributes to the sagittal plane mechanics, which was not verified with published experimental data in the current study. Only the superficial MCL was modelled, and its interaction with the medial meniscus was absent in the current FE model. Inclusion of the deep fibres of MCL could alter the strain experienced by the medial meniscus. In addition, wrapping of the superficial MCL fibres with the tibia was not modelled, which might affect the coronal plane kinematics of the model.

3. Anisotropic behaviour of the other soft tissues such as cartilage and menisci were not captured but were defined as isotropic, linearly elastic materials. As a result, the values of tibiofemoral and patellofemoral contact forces and cartilage stresses may not be accurate and would need further investigation.

4. The results of the current study (i.e., relative ACL strains and meniscal strains) were compared to only two half muscle force jump landing *in-vitro* experiments due to the failure of the cadaver specimen in the full muscle force experiments. The limitation of the experimental data posed a major restriction for model validation.

6.3 Future Directions

Several steps could be taken to overcome the limitations listed in the previous section to obtain improved FE model response. Possible improvements in each stage of the study are included below.

1. Evaluation of ligament laxity has to be considered in the experimental approach to provide useful data in modelling the ligaments computationally. Then, accurate ligament behaviour could be modelled using laxity data. Ligaments can also be modelled using continuum (solid) elements. Solid elements enable the application of anisotropic hyperelastic models to describe ligament behaviour more accurately.

2. The quality of the hexahedral elements in the current study was more than satisfactory. However, randomly assigning the element dimensions can increase the stable time increment of an explicit finite element simulation and can add to the computational cost. Mesh convergence studies are a way to optimize the time increment in an explicit finite element simulation and should be included in further studies.

3. In Polak (2019) study, two other cadaver knees were also tested with ACL and meniscal strains recorded during jump landing where one of the specimens survived all the half and full muscle force jumps. A similar approach to the current study could be employed to develop other subject-specific models.

4. Only sagittal plane mechanics were simulated in the current study, which replicated the input conditions of the DKS. Examining ACL mechanics in a single plane was one of the limitations of Bakker (2015) study, and it is inevitably a limitation in the current study as well. The OpenSim results from Bakker (2015) contained other kinetic conditions (such as ankle torques, valgus and internal tibial rotations) which could not be included in the DKS setup, but can very well be inputted in the current FE model. Inclusion of such injury-prone manoeuvres in the FE model can lead to a better understanding of ACL injury mechanics.

5. The development of the subject-specific model took considerable effort in all stages (i.e., segmentation, mesh generation, and setting up the FE model). The timeline for the development of the subject-specific model was approximately 3-4 months. Alternate model generation strategies such as atlas-based methods for segmentation and morphing of existing meshes for mesh generation could be considered to accelerate the development of future models.

References

Abdel-Rahman, E. and Hefzy, M. S. (1993). A two-dimensional dynamic anatomical model of the human knee joint. *Journal of Biomechanical Engineering*, 115(4):357–365.

Abdel-Rahman, E. M. and Hefzy, M. S. (1998). Three-dimensional dynamic behaviour of the human knee joint under impact loading. *Medical Engineering & Physics*, 20(4):276–290.

Ahn, C., Bui, T. D., Lee, Y. W., Shin, J., and Park, H. (2016). Fully automated, level set-based segmentation for knee mris using an adaptive force function and template: data from the osteoarthritis initiative. *Biomedical engineering online*, 15(1):99.

Akizuki, S., Mow, V. C., Müller, F., Pita, J. C., Howell, D. S., and Manicourt, D. H. (1986). Tensile properties of human knee joint cartilage: I. influence of ionic conditions, weight bearing, and fibrillation on the tensile modulus. *Journal of Orthopaedic Research*, 4(4):379–392.

Ali, A. A., Harris, M. D., Shalhoub, S., Maletsky, L. P., Rullkoetter, P. J., and Shelburne, K. B. (2017). Combined measurement and modeling of specimen-specific knee mechanics for healthy and ACL-deficient conditions. *Journal of Biomechanics*, 57:117–124.

Amiri, S. and Wilson, D. R. (2012). A computational modeling approach for investigating soft tissue balancing in bicruciate retaining knee arthroplasty. *Computational and Mathematical Methods in Medicine*, 2012.

Amis, A. A. and Dawkins, G. P. C. (1991). Functional anatomy of the anterior cruciate ligament. Fibre bundle actions related to ligament replacements and injuries. *Journal of Bone and Joint Surgery - Series B*, 73(2):260–267.

Aprovitola, A. and Gallo, L. (2016). Knee bone segmentation from MRI: A classification and literature review. *Biocybernetics and Biomedical Engineering*, 36(2):437–449.

Asano, T., Akagi, M., and Nakamura, T. (2005). The functional flexion-extension axis of the knee corresponds to the surgical epicondylar axis: In vivo analysis using a biplanar image-matching technique. *Journal of Arthroplasty*, 20(8):1060–1067.

Atkinson, P., Atkinson, T., Huang, C., and Doane, R. (2000). A comparison of the mechanical and dimensional properties of the human medial and lateral patellofemoral ligaments. *46th Annual Meeting, Orthopaedic Research Society*, page 0776.

Bakker, R. (2015). *The Effect of Sagittal Plane Mechanics on Anterior Cruciate Ligament Strain During Jump Landing* (MASc Thesis, University of Waterloo, Waterloo, Canada).

Bakker, R., Tomescu, S., Brenneman, E., Hangalur, G., Laing, A., and Chandrashekar, N. (2016). Effect of sagittal plane mechanics on ACL strain during jump landing. *Journal of Orthopaedic Research*, 34(9):1636–1644.

Baldwin, M. A., Clary, C. W., Fitzpatrick, C. K., Deacy, J. S., Maletsky, L. P., and Rullkoetter, P. J. (2012). Dynamic finite element knee simulation for evaluation of knee replacement mechanics. *Journal of Biomechanics*, 45(3):474–483.

Baldwin, M. A., Langenderfer, J. E., Rullkoetter, P. J., and Laz, P. J. (2010). Development of subject-specific and statistical shape models of the knee using an efficient segmentation and mesh-morphing approach. *Computer Methods and Programs in Biomedicine*, 97(3):232–240.

Bates, N. A., Nesbitt, R. J., Shearn, J. T., Myer, G. D., and Hewett, T. E. (2015). Relative Strain in the Anterior Cruciate Ligament and Medial Collateral Ligament During Simulated Jump Landing and Sidestep Cutting Tasks. *The American Journal of Sports Medicine*, 43(9):2259–2269.

Beidokhti, H. N., Janssen, D., van de Groes, S., Hazrati, J., Van den Boogaard, T., and Verdonschot, N. (2017). The influence of ligament modelling strategies on the predictive capability of finite element models of the human knee joint. *Journal of biomechanics*, 65:1–11.

Beillas, P., Lee, S. W., Tashman, S., and Yang, K. H. (2007). Sensitivity of the tibio-femoral response to finite element modeling parameters. *Computer Methods in Biomechanics and Biomedical Engineering*, 10(3):209–221.

Beillas, P., Papaioannou, G., Tashman, S., and Yang, K. H. (2004). A new method to investigate in vivo knee behavior using a finite element model of the lower limb. *Journal of Biomechanics*, 37(7):1019–1030.

Belytschko, T., Ong, J. S.-J., Liu, W. K., and Kennedy, J. M. (1984). Hourglass control in linear and nonlinear problems. *Computer Methods in Applied Mechanics and Engineering*, 43(3):251–276.

Beynnon, B., Howe, J. G., Pope, M. H., Johnson, R. J., and Fleming, B. C. (1992a). The measurement of anterior cruciate ligament strain in-vivo. *International Orthopaedics (SICOT)*, 16.

Beynnon, B., Pope, M., Wertheimer, C., Johnson, R., Fleming, B., and Howe, C. (1992b). The effect of functional knee braces on anterior cruciate ligament strain, in-vivo. *The Journal of Bone and Joint Surgery, Incorporated*, 74:1298–1312.

Beynnon, B. D., Johnson, R. J., Fleming, B. C., Stankewich, C. J., Renstrom, P. A., and Nichols, C. E. (1997). The strain behavior of the anterior cruciate ligament during squatting and active flexion-extension. A comparison of an open and a closed kinetic chain exercise. *American Journal of Sports Medicine*, 25(6):823–829.

Blankevoort, L. and Huiskes, R. (1996). Validation of a Three-Dimensional Model of the Knee. 29(7):955–961.

Blankevoort, L., Kuiper, J. H., Huiskes, R., and Grootenboer, H. J. (1991). Articular contact in a three-dimensional model of the knee. *Journal of Biomechanics*, 24(11):1019–1031.

Bloemker, K. H., Guess, T. M., Maletsky, L., and Dodd, K. (2012). Computational knee ligament modeling using experimentally determined zero-load lengths. *The open biomedical engineering journal*, 6:33.

Boden, B. P., Sheehan, F. T., Torg, J. S., and Hewett, T. E. (2010). Noncontact anterior cruciate ligament injuries: Mechanisms and risk factors. *Journal of the American Academy of Orthopaedic Surgeons*, 18(9):520–527.

Burkhart, T. A., Andrews, D. M., and Dunning, C. E. (2013). Finite element modeling mesh quality, energy balance and validation methods: A review with recommendations associated with the modeling of bone tissue. *Journal of Biomechanics*, 46(9):1477–1488.

Butler, D., Kay, M., and Stouffer, D. (1986). Fascicle-Bone Units From Human Patellar Tendon and Knee Ligaments. *Journal of Biomechanics*, 19(6):425–432.

Cassidy, K., Hangalur, G., Sabharwal, P., and Chandrashekar, N. (2013). Combined in vivo/in vitro method to study anteriomedial bundle strain in the anterior cruciate ligament using a dynamic knee simulator. *Journal of biomechanical engineering*, 135(3):035001.

Chandrashekar, N. (2005). *Sex-based difference in the morphology, tensile properties and ultrastructure of the human anterior cruciate ligament and patellar tendon* (PhD Thesis, Texas Tech University, Lubbock, TX, USA).

Chandrashekar, N., Mansouri, H., Slauterbeck, J., and Hashemi, J. (2006). Sex-based differences in the tensile properties of the human anterior cruciate ligament. *Journal of biomechanics*, 39(16):2943–2950.

Chandrashekar, N., Slauterbeck, J., and Hashemi, J. (2005). Sex-based differences in the anthropometric characteristics of the anterior cruciate ligament and its relation to intercondylar notch geometry: A cadaveric study. *American Journal of Sports Medicine*, 33(10):1492–1498.

Chen, Z., Zhang, Z., Wang, L., Li, D., Zhang, Y., and Jin, Z. (2016). Evaluation of a subject-specific musculoskeletal modelling framework for load prediction in total knee arthroplasty. *Medical engineering & physics*, 38(8):708–716.

Dabiri, Y. and Li, L. (2013). Altered knee joint mechanics in simple compression associated with early cartilage degeneration. *Computational and mathematical methods in medicine*, 2013.

Dam, E. B., Lillholm, M., Marques, J., and Nielsen, M. (2015). Automatic segmentation of high- and low-field knee MRIs using knee image quantification with data from the osteoarthritis initiative. *SPIE Journal of Medical Imaging*, 2(2):024001.

De Vita, R. (2005). *Structural Constitutive Models for Knee Ligaments* (PhD Thesis, University of Pittsburgh, Pittsburgh, PA, USA).

Delp, S. L., Ringwelski, D. A., and Carroll, N. C. (1994). Transfer of the rectus femoris: Effects of transfer site on moment arms about the knee and hip. *Journal of Biomechanics*, 27(10):1201–1211.

Domire, Z. J., Boros, R. L., and Hashemi, J. (2011). An examination of possible quadriceps force at the time of anterior cruciate ligament injury during landing: a simulation study. *Journal of biomechanics*, 44(8):1630–1632.

Duthon, V., Barea, C., Abrassart, S., Fasel, H., Fritschy, D., and Me´ne´trey, J. (2006). Anatomy of the anterior cruciate ligament. *Knee Surgery, Sports Traumatology, Arthroscopy*, 14(1):204–213.

Fedorov, A., Beichel, R., Kalpathy-Cramer, J., Finet, J., Fillion-Robin, J.-C., Pujol, S., Bauer, C., Jennings, D., Fennessy, F., Sonka, M., et al. (2012). 3d slicer as an image computing platform for the quantitative imaging network. *Magnetic resonance imaging*, 30(9):1323–1341.

Fox, A. J., Bedi, A., and Rodeo, S. A. (2009). The basic science of articular cartilage: Structure, composition, and function. *Sports Health*, 1(6):461–468.

Fox, A. J., Bedi, A., and Rodeo, S. A. (2012). The Basic Science of Human Knee Menisci: Structure, Composition, and Function. *Sports Health*, 4(4):340–351.

Fripp, J., Crozier, S., Warfield, S. K., and Ourselin, S. (2007). Automatic segmentation of the bone and extraction of the bone-cartilage interface from magnetic resonance images of the knee. *Physics in Medicine and Biology*, 52(6):1617–1631.

Galbusera, F., Freutel, M., DÃ¼rselen, L., Dâ€™Aiuto, M., Croce, D., Villa, T., Sansone, V., and Innocenti, B. (2014). Material Models and Properties in the Finite Element Analysis of Knee Ligaments: A Literature Review. *Frontiers in Bioengineering and Biotechnology*, 2(November):1–11.

Garg, A. and Walker, P. S. (1990). Prediction of total knee motion using a three-dimensional computer-graphics model. *Journal of Biomechanics*, 23(1).

Gayzik, F., Moreno, D., Geer, C., Wuertzer, S., Martin, R., and Stitzel, J. (2011). Development of a full body cad dataset for computational modeling: a multi-modality approach. *Annals of biomedical engineering*, 39(10):2568.

Giffin, J. R., Vogrin, T. M., Zantop, T., Woo, S. L. Y., and Harner, C. D. (2004). Effects of Increasing Tibial Slope on the Biomechanics of the Knee. *American Journal of Sports Medicine*, 32(2):376–382.

Girgis, F. G., Marshall, J. L., and Monajem, A. (1975). The cruciate ligaments of the knee joint. anatomical, functional and experimental analysis. *Clinical orthopaedics and related research*, (106):216–231.

Griffin, L. Y., Albohm, M. J., Arendt, E. A., Bahr, R., Beynnon, B. D., DeMaio, M., Dick, R. W., Engebretsen, L., Garrett, W. E., Hannafin, J. A., Hewett, T. E., Huston, L. J., Ireland, M. L., Johnson, R. J., Lephart, S., Mandelbaum, B. R., Mann, B. J., Marks, P. H., Marshall, S. W., Myklebust, G., Noyes, F. R., Powers, C., Shields, C., Shultz, S. J., Silvers, H., Slauterbeck, J., Taylor, D. C., Teitz, C. C., Wojtys, E. M., and Yu, B. (2006). Understanding and preventing noncontact anterior cruciate ligament injuries: A review of the Hunt Valley II Meeting, January 2005. *American Journal of Sports Medicine*, 34(9):1512–1532.

Grosland, N. M., Shivanna, K. H., Magnotta, V. A., Kallemeyn, N. A., DeVries, N. A., Tadepalli, S. C., and Lisle, C. (2009). IA-FEMesh: An open-source, interactive, multi-block approach to anatomic finite element model development. *Computer Methods and Programs in Biomedicine*, 94(1):96–107.

Guess, T. M. (2012). Forward dynamics simulation using a natural knee with menisci in the multibody framework. *Multibody System Dynamics*, 28(1-2):37–53.

Guess, T. M. and Razu, S. (2017). Loading of the medial meniscus in the ACL deficient knee: A multibody computational study. *Medical Engineering and Physics*, 41:26–34.

Hadagali, P., Peters, J. R., and Balasubramanian, S. (2018). Morphing the feature-based multi-blocks of normative/healthy vertebral geometries to scoliosis vertebral geometries: development of personalized finite element models.

Halonen, K. S., Mononen, M. E., Töyräs, J., Kröger, H., Joukainen, A., and Korhonen, R. K. (2016). Optimal graft stiffness and pre-strain restore normal joint motion and cartilage responses in ACL reconstructed knee. *Journal of Biomechanics*, 49(13):2566–2576.

Hangalur, G., Brenneman, E., Nicholls, M., Bakker, R., Laing, A., and Chandrashekar, N. (2016). Can a knee brace reduce the strain in the anterior cruciate ligament? A study using combined in vivo/in vitro method. *Prosthetics and Orthotics International*, 40(3):394–399.

Hao, L. (2006). *Registration-Based Segmentation of Medical Images* (Graduate Research Paper, National University of Singapore, Singapore).

Harris, M. D., Cyr, A. J., Ali, A. A., Fitzpatrick, C. K., Rullkoetter, P. J., Maletsky, L. P., and Shelburne, K. B. (2016). A Combined Experimental and Computational Approach to Subject-Specific Analysis of Knee Joint Laxity. *Journal of Biomechanical Engineering*, 138(8):1–8.

Hashemi, J., Breighner, R., Chandrashekar, N., Hardy, D. M., Chaudhari, A. M., Shultz, S. J., Slauterbeck, J. R., and Beynnon, B. D. (2011). Hip extension, knee flexion paradox: A new mechanism for non-contact ACL injury. *Journal of Biomechanics*, 44(4):577–585.

Hashemi, J., Chandrashekar, N., Gill, B., Beynnon, B. D., Slauterbeck, J. R., Schutt, R. C., Mansouri, H., and Dabezies, E. (2008). The geometry of the tibial plateau and its influence on the biomechanics of the tibiofemoral joint. *Journal of Bone and Joint Surgery - Series A*, 90(12):2724–2734.

Hashemi, J., Chandrashekar, N., Jang, T., Karpat, F., Oseto, M., and Ekwaro-Osire, S. (2007). An alternative mechanism of non-contact anterior cruciate ligament injury during jump-landing: In-vitro simulation. *Experimental Mechanics*, 47(3):347–354.

Hauch, K. N., Villegas, D. F., and Haut Donahue, T. L. (2010). Geometry, time-dependent and failure properties of human meniscal attachments. *Journal of Biomechanics*, 43(3):463–468.

Haut Donahue, T. L., Hull, M. L., Rashid, M. M., and Jacobs, C. R. (2002). A Finite Element Model of the Human Knee Joint for the Study of Tibio-Femoral Contact. *Journal of Biomechanical Engineering*, 124(3):273.

Henninger, H. B., Reese, S. P., Anderson, A. E., and Weiss, J. A. (2010). Validation of computational models in biomechanics. *Proceedings of the Institution of Mechanical Engineers, Part H: Journal of Engineering in Medicine*, 224(7):801–812.

Hewett, T. E., Myer, G. D., Ford, K. R., Heidt, R. S., Colosimo, A. J., McLean, S. G., Van Den Bogert, A. J., Paterno, M. V., and Succop, P. (2005). Biomechanical measures of

neuromuscular control and valgus loading of the knee predict anterior cruciate ligament injury risk in female athletes: A prospective study. *American Journal of Sports Medicine*, 33(4):492–501.

Hollis, J. M., Takai, S., Adams, D. J., Horibe, S., and Woo, S. L.-Y. (1991). The Effects of Knee Motion and External Loading on the Length of the Anterior Cruciate Ligament (ACL): A Kinematic Study. *Journal of Biomechanical Engineering*, 113(2):208–214.

Inman, V., Ralston, H., and Todd, F. (1981). *Human Walking*. Williams & Wilkins.

Ireland, M. L., Ballantyne, B. T., Little, K., and McClay, I. S. (2001). A radiographic analysis of the relationship between the size and shape of the intercondylar notch and anterior cruciate ligament injury. *Knee Surgery, Sports Traumatology, Arthroscopy*, 9(4):200–205.

Kalra, M., Bakker, R., Tomescu, S. S., Polak, A. M., Nicholls, M., and Chandrashekar, N. (2019). The effect of unloader knee braces on medial meniscal strain. *Prosthetics and Orthotics International*, 43(2):132–139.

Kapur, T., Beardsley, P., Gibson, S., Grimson, W., and Wells, W. (1998). Model-based segmentation of clinical knee mri. In *Proc. IEEE Int'l Workshop on Model-Based 3D Image Analysis*, pages 97–106.

Kia, M., Schafer, K., Lipman, J., Cross, M., Mayman, D., Pearle, A., Wickiewicz, T., and Imhauser, C. (2016). A Multibody Knee Model Corroborates Subject-Specific Experimental Measurements of Low Ligament Forces and Kinematic Coupling During Passive Flexion. *Journal of Biomechanical Engineering*, 138(5):051010.

Kiapour, A. (2013). *Non-Contact ACL Injuries during Landing: Risk Factors and Mechanisms* (PhD Thesis, University of Toledo, Toledo, OH, USA).

Kiapour, A., Kiapour, A. M., Kaul, V., Quatman, C. E., Wordeman, S. C., Hewett, T. E., Demetropoulos, C. K., and Goel, V. K. (2013). Finite Element Model of the Knee for Investigation of Injury Mechanisms: Development and Validation. *Journal of Biomechanical Engineering*, 136(1):011002.

Kiapour, A. and Murray, M. M. (2014). Basic science of anterior cruciate ligament injury and repair. *Bone and Joint Research*, 3(2):20–31.

Koga, H., Nakamae, A., Shima, Y., Iwasa, J., Myklebust, G., Engebretsen, L., Bahr, R., and Krosshaug, T. (2010). Mechanisms for noncontact anterior cruciate ligament injuries: Knee joint kinematics in 10 injury situations from female team handball and basketball. *American Journal of Sports Medicine*, 38(11):2218–2225.

LeRoux, M. A. and Setton, L. A. (2002). Experimental and biphasic FEM determinations of the material properties and hydraulic permeability of the meniscus in tension. *Journal of Biomechanical Engineering*, 124(3):315–321.

Liukkonen, M. K., Mononen, M. E., Tanska, P., Saarakkala, S., Nieminen, M. T., and Korhonen, R. K. (2017). Application of a semi-automatic cartilage segmentation method for biomechanical modeling of the knee joint. *Computer methods in biomechanics and biomedical engineering*, 20(13):1453–1463.

Mall, N. A., Chalmers, P. N., Moric, M., Tanaka, M. J., Cole, B. J., Bach, B. R., and Paletta, G. A. (2014). Incidence and trends of anterior cruciate ligament reconstruction in the United States. *American Journal of Sports Medicine*, 42(10):2363–2370.

Mao, H., Gao, H., Cao, L., Genthikatti, V. V., and Yang, K. H. (2013). Development of high-quality hexahedral human brain meshes using feature-based multi-block approach. *Computer methods in biomechanics and biomedical engineering*, 16(3):271–279.

Marouane, H., Shirazi-Adl, A., and Hashemi, J. (2015). Quantification of the role of tibial posterior slope in knee joint mechanics and ACL force in simulated gait. *Journal of Biomechanics*, 48(10):1899–1905.

Marra, M. A., Vanheule, V., Fluit, R., Koopman, B. H., Rasmussen, J., Verdonschot, N., and Andersen, M. S. (2015). A subject-specific musculoskeletal modeling framework to predict in vivo mechanics of total knee arthroplasty. *Journal of biomechanical engineering*, 137(2):020904.

Mather, R. C., Koenig, L., Kocher, M. S., Dall, T. M., Gallo, P., Scott, D. J., Bach, B. R., and Spindler, K. P. (2013). Societal and economic impact of anterior cruciate ligament tears. *Journal of Bone and Joint Surgery - Series A*, 95(19):1751–1759.

McLean, S. G., Oh, Y. K., Palmer, M. L., Lucey, S. M., Lucarelli, D. G., Ashton-Miller, J. A., and Wojtys, E. M. (2011). The relationship between anterior tibial acceleration, tibial slope, and ACL strain during a simulated jump landing task. *Journal of Bone and Joint Surgery - Series A*, 93(14):1310–1317.

Moore, K. L. and Dalley, A. F. (2013). *Clinically Oriented Anatomy*. Lippincott Williams & Wilkins.

Mootanah, R., Imhauser, C. W., Reisse, F., Carpanen, D., Walker, R. W., Koff, M. F., Lenhoff, M. W., Rozbruch, S. R., Fragomen, A. T., Dewan, Z., et al. (2014). Development and validation of a computational model of the knee joint for the evaluation of surgical treatments for osteoarthritis. *Computer methods in biomechanics and biomedical engineering*, 17(13):1502–1517.

Myers, C. A., Torry, M. R., Shelburne, K. B., Giphart, J. E., LaPrade, R. F., Woo, S. L., and Steadman, J. R. (2012). In vivo tibiofemoral kinematics during 4 functional tasks of increasing demand using biplane fluoroscopy. *The American journal of sports medicine*, 40(1):170–178.

Noyes, F. and Grood, E. (1976). The strength of the anterior cruciate ligament in humans and rhesus monkeys. *The Journal of bone and joint surgery*, 58:1074–1082.

Oh, Y. K., Kreinbrink, J. L., Wojtys, E. M., and Ashton-Miller, J. A. (2012). Effect of axial tibial torque direction on ACL relative strain and strain rate in an in vitro simulated pivot landing. *Journal of Orthopaedic Research*, 30(4):528–534.

Orozco, G. A., Tanska, P., Mononen, M. E., Halonen, K. S., and Korhonen, R. K. (2018). The effect of constitutive representations and structural constituents of ligaments on knee joint mechanics. *Scientific Reports*, 8(1):1–15.

Pena, E., Calvo, B., Martinez, M., Palanca, D., and Doblaré, M. (2005). Finite element analysis of the effect of meniscal tears and meniscectomies on human knee biomechanics. *Clinical Biomechanics*, 20(5):498–507.

Petersen, W. and Zantop, T. (2007). Anatomy of the anterior cruciate ligament with regard to its two bundles. *Clinical Orthopaedics and Related Research®*, 454:35–47.

Podraza, J. T. and White, S. C. (2010). Effect of knee flexion angle on ground reaction forces, knee moments and muscle co-contraction during an impact-like deceleration landing: Implications for the non-contact mechanism of ACL injury. *Knee*, 17(4):291–295.

Polak, A. M. (2019). *ACL Strain During Single-Leg Jump Landing: An Experimental and Computational Investigation* (MASc Thesis, University of Waterloo, Waterloo, Canada).

Potter, H. G., Jain, S. K., Ma, Y., Black, B. R., Fung, S., and Lyman, S. (2012). Cartilage injury after acute, isolated anterior cruciate ligament tear: Immediate and longitudinal effect with clinical/MRI follow-up. *American Journal of Sports Medicine*, 40(2):276–285.

Renstrom, P., Ljungqvist, A., Arendt, E., Beynnon, B., Fukubayashi, T., Garrett, W., Georgoulis, T., Hewett, T. E., Johnson, R., Krosshaug, T., Mandelbaum, B., Micheli, L., Myklebust, G., Roos, E., Roos, H., Schamasch, P., Shultz, S., Werner, S., Wojtys, E., Engebretsen, L., and Khan, K. (2008). Non-contact ACL injuries in female athletes: An International Olympic Committee current concepts statement. *British Journal of Sports Medicine*, 42(4):394–412.

Rhee, S. J., Pavlou, G., Oakley, J., Barlow, D., and Haddad, F. (2012). Modern management of patellar instability. *International Orthopaedics*, 36(12):2447–2456.

Rodriguez-Vila, B., Sánchez-González, P., Oropesa, I., Gomez, E., and Pierce, D. M. (2017). Automated hexahedral meshing of knee cartilage structures–application to data from the osteoarthritis initiative. *Computer methods in biomechanics and biomedical engineering*, 20(14):1543–1553.

Sakane, M., Fox, R. J., Woo, S. L., Livesay, G. A., Li, G., and Fu, F. H. (1997). In situ forces in the anterior cruciate ligament and its bundles in response to anterior tibial loads. *Journal of Orthopaedic Research*, 15(2):285–293.

Salem, H. S., Shi, W. J., Tucker, B. S., Dodson, C. C., Ciccotti, M. G., Freedman, K. B., and Cohen, S. B. (2018). Contact Versus Noncontact Anterior Cruciate Ligament Injuries: Is Mechanism of Injury Predictive of Concomitant Knee Pathology? *Arthroscopy - Journal of Arthroscopic and Related Surgery*, 34(1):200–204.

Schatzmann, L., Brunner, P., and Stäubli, H. (1998). Effect of cyclic preconditioning on the tensile properties of human quadriceps tendons and patellar ligaments. *Knee Surgery, Sports Traumatology, Arthroscopy*, 6(1):S56–S61.

Schonning, A., Oommen, B., Ionescu, I., and Conway, T. (2009). Hexahedral mesh development of free-formed geometry: The human femur exemplified. *CAD Computer Aided Design*, 41(8):566–572.

Schwartz, D., Guleyupoglu, B., Koya, B., Stitzel, J. D., and Gayzik, F. S. (2015). Development of a Computationally Efficient Full Human Body Finite Element Model. *Traffic Injury Prevention*, 16:49–56.

Serpell, B. G., Scarvell, J. M., Ball, N. B., and Smith, P. N. (2012). Mechanisms and risk factors for noncontact acl injury in age mature athletes who engage in field or court sports: a summary of the literature since 1980. *The Journal of Strength & Conditioning Research*, 26(11):3160–3176.

Shimokochi, Y., Ambegaonkar, J. P., Meyer, E. G., Lee, S. Y., and Shultz, S. J. (2013). Changing sagittal plane body position during single-leg landings influences the risk of non-contact anterior cruciate ligament injury. *Knee Surgery, Sports Traumatology, Arthroscopy*, 21(4):888–897.

Shimokochi, Y., Lee, S. Y., Shultz, S. J., and Schmitz, R. J. (2009). The relationships among sagittal-plane lower extremity moments: Implications for landing strategy in anterior cruciate ligament injury prevention. *Journal of Athletic Training*, 44(1):33–38.

Shin, C. S., Chaudhari, A. M., and Andriacchi, T. P. (2007). The influence of deceleration forces on ACL strain during single-leg landing: A simulation study. *Journal of Biomechanics*, 40(5):1145–1152.

Shivanna, K. H., Tadepalli, S. C., and Grosland, N. M. (2010). Feature-based multiblock finite element mesh generation. *CAD Computer Aided Design*, 42(12):1108–1116.

Shultz, S. J., Schmitz, R. J., Benjaminse, A., Chaudhari, A. M., Collins, M., and Padua, D. A. (2012). ACL Research Retreat VI: An update on ACL injury risk and prevention. *Journal of Athletic Training*, 47(5):591–603.

Smith, J. P. and Barrett, G. R. (2001). Medial and lateral meniscal tear patterns in anterior cruciate ligament-deficient knees. A prospective analysis of 575 tears. *American Journal of Sports Medicine*, 29(4):415–419.

Song, Y., Debski, R. E., Musahl, V., Thomas, M., and Woo, S. L. (2004). A three-dimensional finite element model of the human anterior cruciate ligament: A computational analysis with experimental validation. *Journal of Biomechanics*, 37(3):383–390.

Subburaj, K., Ravi, B., and Agarwal, M. (2009). Automated identification of anatomical landmarks on 3D bone models reconstructed from CT scan images. *Computerized Medical Imaging and Graphics*, 33(5):359–368.

Sun, Y., Teo, E., and Zhang, Q. (2006). Discussions of knee joint segmentation. In *2006 International Conference on Biomedical and Pharmaceutical Engineering*. IEEE.

Swanson, M. S., Prescott, J. W., Best, T. M., Powell, K., Jackson, R. D., Haq, F., and Gurcan, M. N. (2010). Semi-automated segmentation to assess the lateral meniscus in normal and osteoarthritic knees. *Osteoarthritis and Cartilage*.

Taylor, K. A., Terry, M. E., Utturkar, G. M., Spritzer, C. E., Queen, R. M., Irribarra, L. A., Garrett, W. E., and DeFrate, L. E. (2011). Measurement of in vivo anterior cruciate ligament strain during dynamic jump landing. *Journal of Biomechanics*, 44(3):365–371.

Trad, Z., Barkaoui, A., Chafra, M., and Tavares, J. M. R. S. (2018). *FEM Analysis of the Human Knee Joint A Review*.

Trent, P., Walker, P. S., and Wolf, B. (1976). Ligament length patterns, strength, and rotational axes of the knee joint. *Clinical Orthopaedics and Related Research*, 117:263–270.

Wang, Z., Rao, A., and Rueckert, D. (2013). Patch-based Segmentation without Registration : Application to Knee MRI. *MICCAI Challenge Workshop on Segmentation: Algorithms, Theory and Applications (SATA)*.

Westermann, R. W., Wolf, B. R., and Elkins, J. M. (2013). Effect of ACL reconstruction graft size on simulated Lachman testing: a finite element analysis. *The Iowa Otrhopaedic Journal*, pages 70–77.

Wismans, J., Veldpaus, F., and Janssen, J. (1980). A three dimensional mathematical model of the knee joint*. *Journal of Biomechanics*, 13(8):677–685.

Withrow, T. J., Huston, L. J., Wojtys, E. M., and Ashton-Miller, J. A. (2006). The relationship between quadriceps muscle force, knee flexion, and anterior cruciate ligament strain in an in vitro simulated jump landing. *American Journal of Sports Medicine*, 34(2):269–274.

Woo, S. L.-Y., Hollis, J. M., Adams, D. J., Lyon, R. M., and Takai, S. (1991). Tensile properties of the human femur-anterior cruciate ligament-tibia complex: the effects of specimen age and orientation. *The American journal of sports medicine*, 19(3):217–225.

Yamamoto, K., Hirokawa, S., and Kawada, T. (1998). Strain distribution in the ligament using photoelasticity. a direct application to the human acl. *Medical engineering & physics*, 20(3):161–168.

Yang, K. H. (2018). *Basic finite element method as applied to injury biomechanics*. Academic Press, London, England.

Zantop, T., Petersen, W., Sekiya, J. K., Musahl, V., and Fu, F. H. (2006). Anterior cruciate ligament anatomy and function relating to anatomical reconstruction. *Knee Surgery, Sports Traumatology, Arthroscopy*, 14(10):982–992.

Zielinska, B. and Haut Donahue, T. L. (2006). 3D Finite Element Model of Meniscectomy: Changes in Joint Contact Behavior. *Journal of Biomechanical Engineering*, 128(1):115.

APPENDICES

Appendix A

Boundary Conditions and Results of P2 – P10 Participant Profiles

A.1 BCs and Results from Single-Leg Jump Landings of P2 – P10 Profiles

The kinematic and kinetic boundary conditions (hip and ankle displacements, muscle forces and hip moment) of participant profile P1 were presented in Section 3.2.2. The same is presented for the rest of the profiles, P2 – P10, in this section. In addition, verification of model kinematics (flexion angle versus time) during the jump is also presented. Further, ACL strain output from the model is compared to the *in-vitro* experimental results from Bakker (2015)'s study. Finally, the energy balance during the simulations of P2 – P10 profiles is presented.

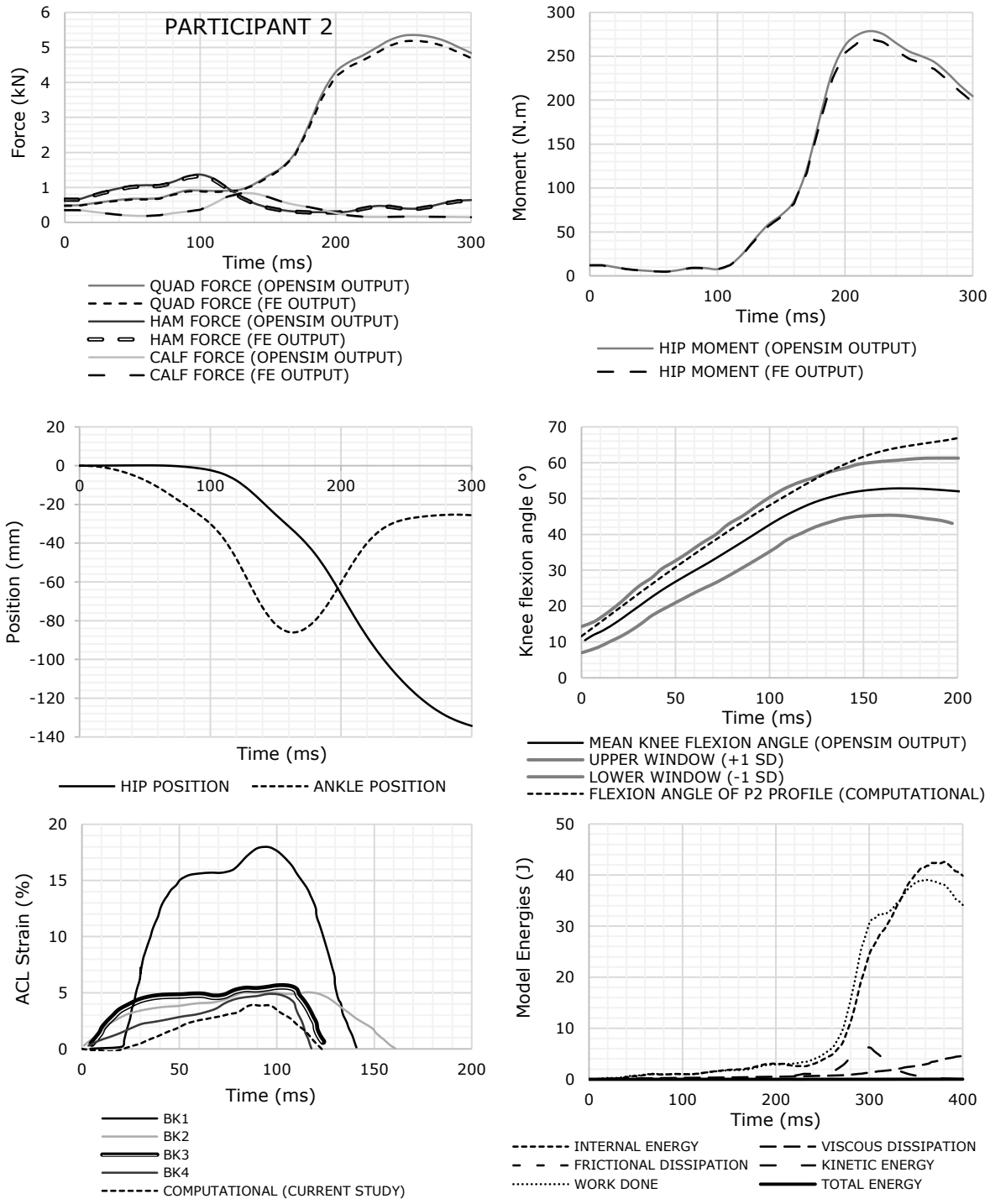

Figure A.1: P2 participant profile results
Kinetic input (top row), Kinematic input (centre, left) for jump landing. Verification of model kinematic output (centre, right), ACL strain results (bottom left) and model energy (bottom right) during the FE simulation

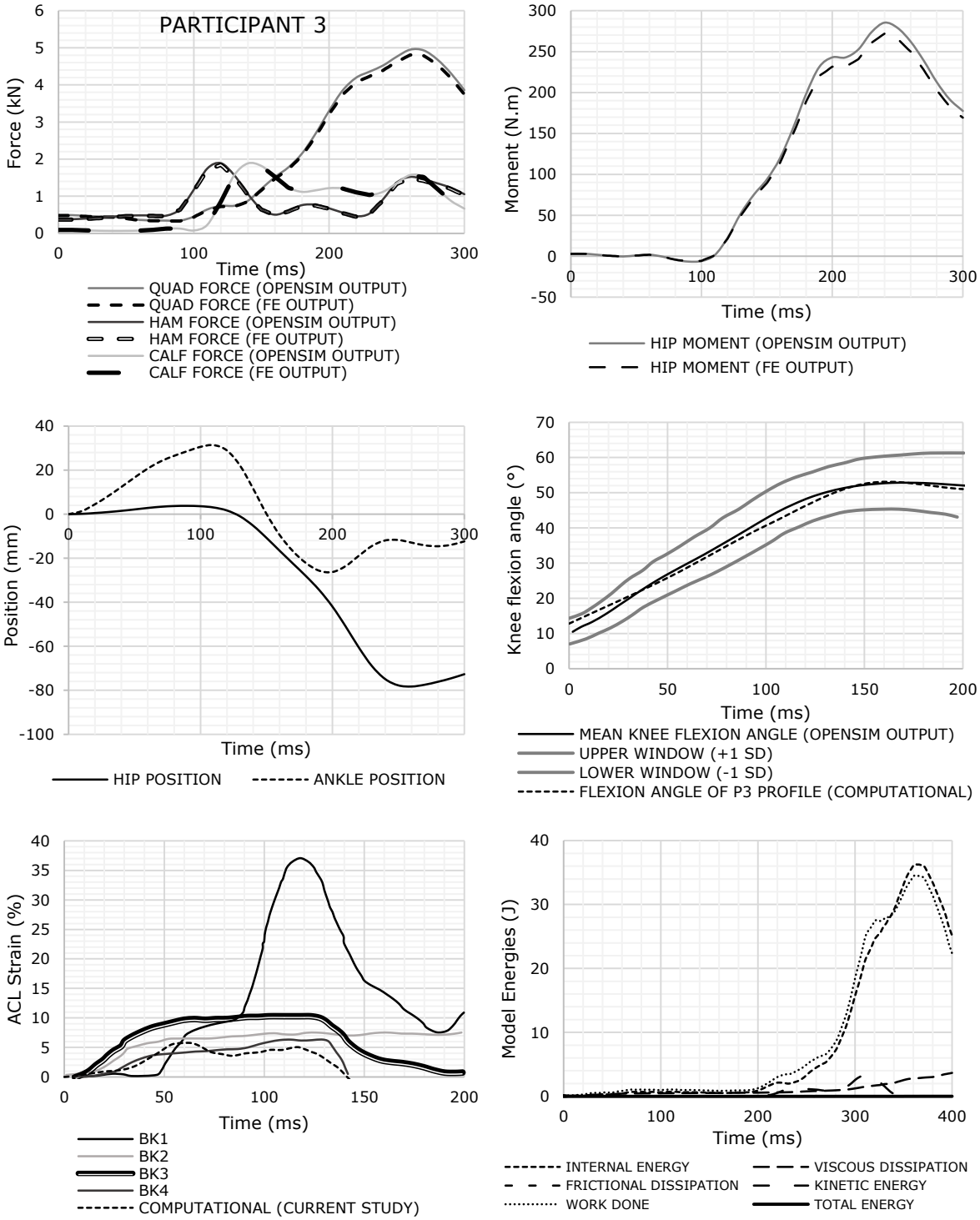

Figure A.2: P3 participant profile results
Kinetic input (top row), Kinematic input (centre, left) for jump landing. Verification of model kinematic output (centre, right), ACL strain results (bottom left) and model energy (bottom right) during the FE simulation

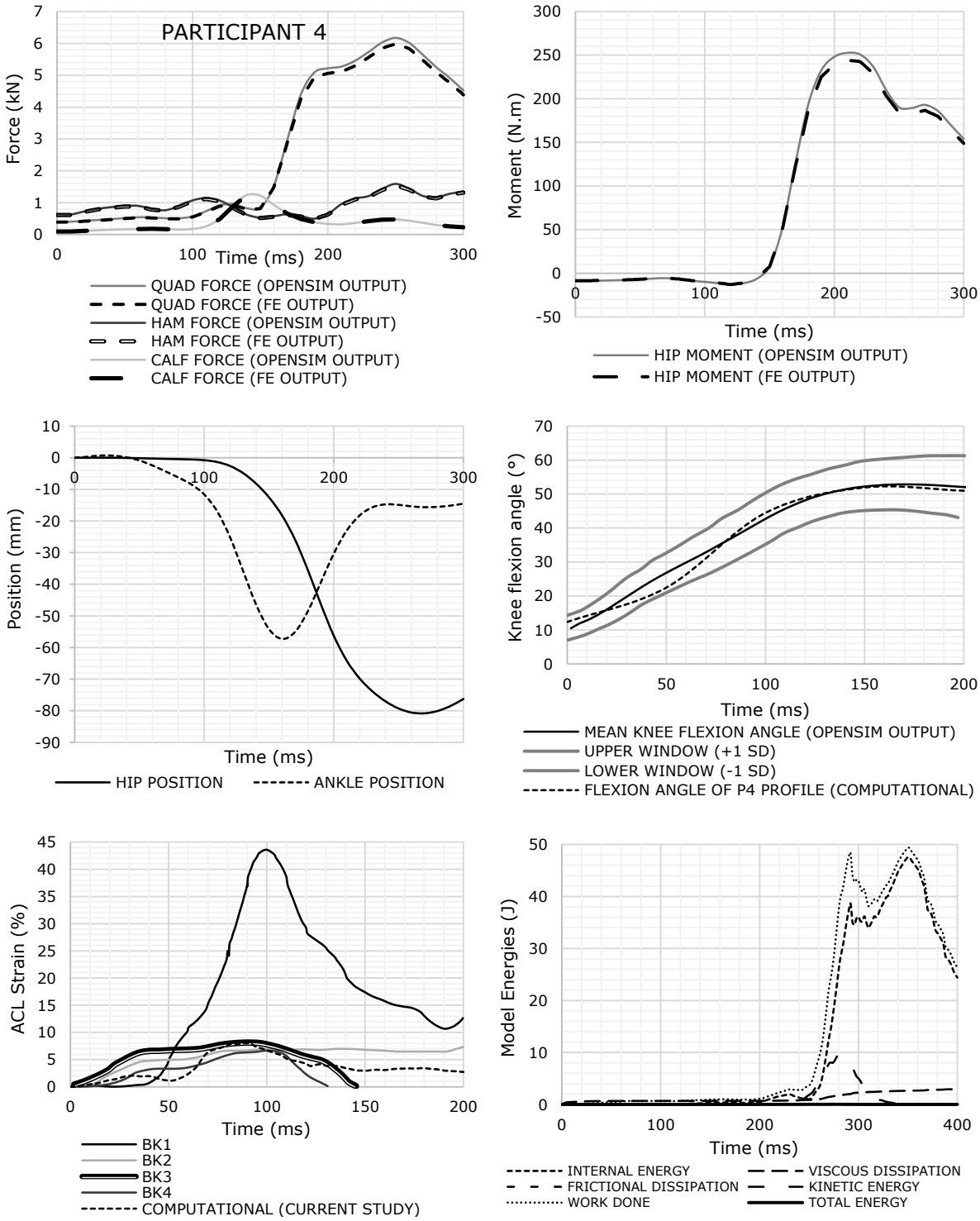

Figure A.3: P4 participant profile results
Kinetic input (top row), Kinematic input (centre, left) for jump landing. Verification of model kinematic output (centre, right), ACL strain results (bottom left) and model energy (bottom right) during the FE simulation

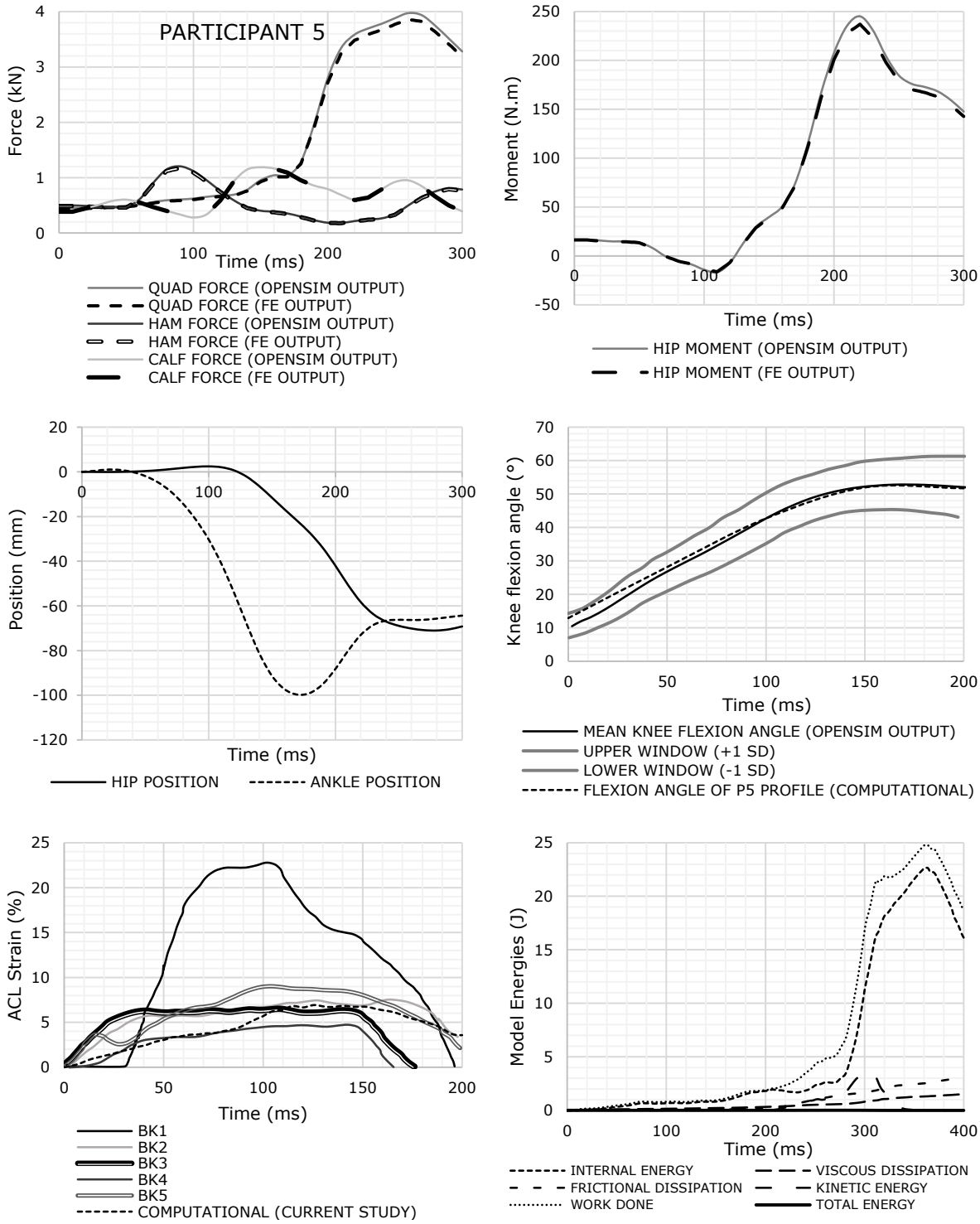

Figure A.4: P5 participant profile results
Kinetic input (top row), Kinematic input (centre, left) for jump landing. Verification of model kinematic output (centre, right), ACL strain results (bottom left) and model energy (bottom right) during the FE simulation

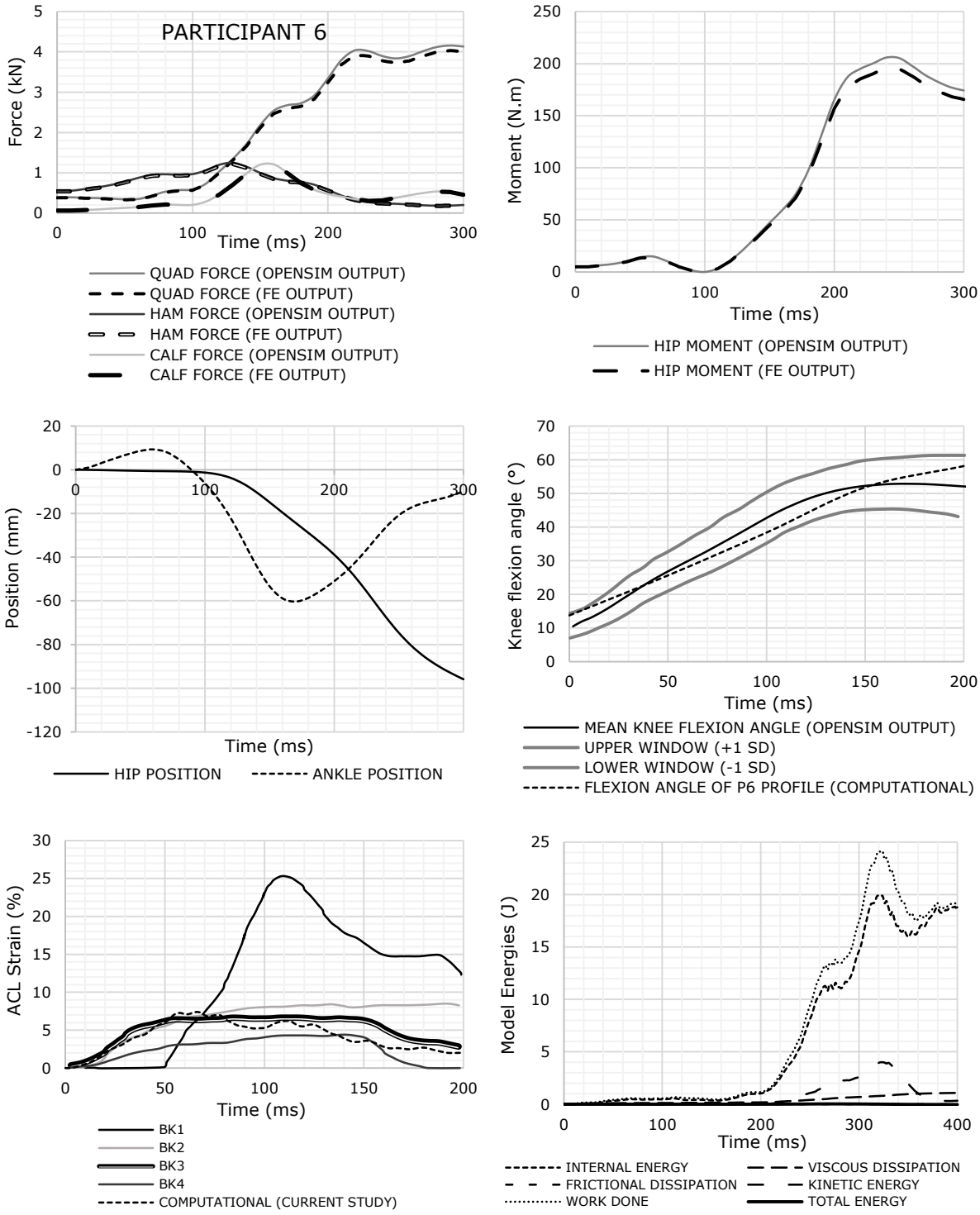

Figure A.5: P6 participant profile results
Kinetic input (top row), Kinematic input (centre, left) for jump landing. Verification of model kinematic output (centre, right), ACL strain results (bottom left) and model energy (bottom right) during the FE simulation

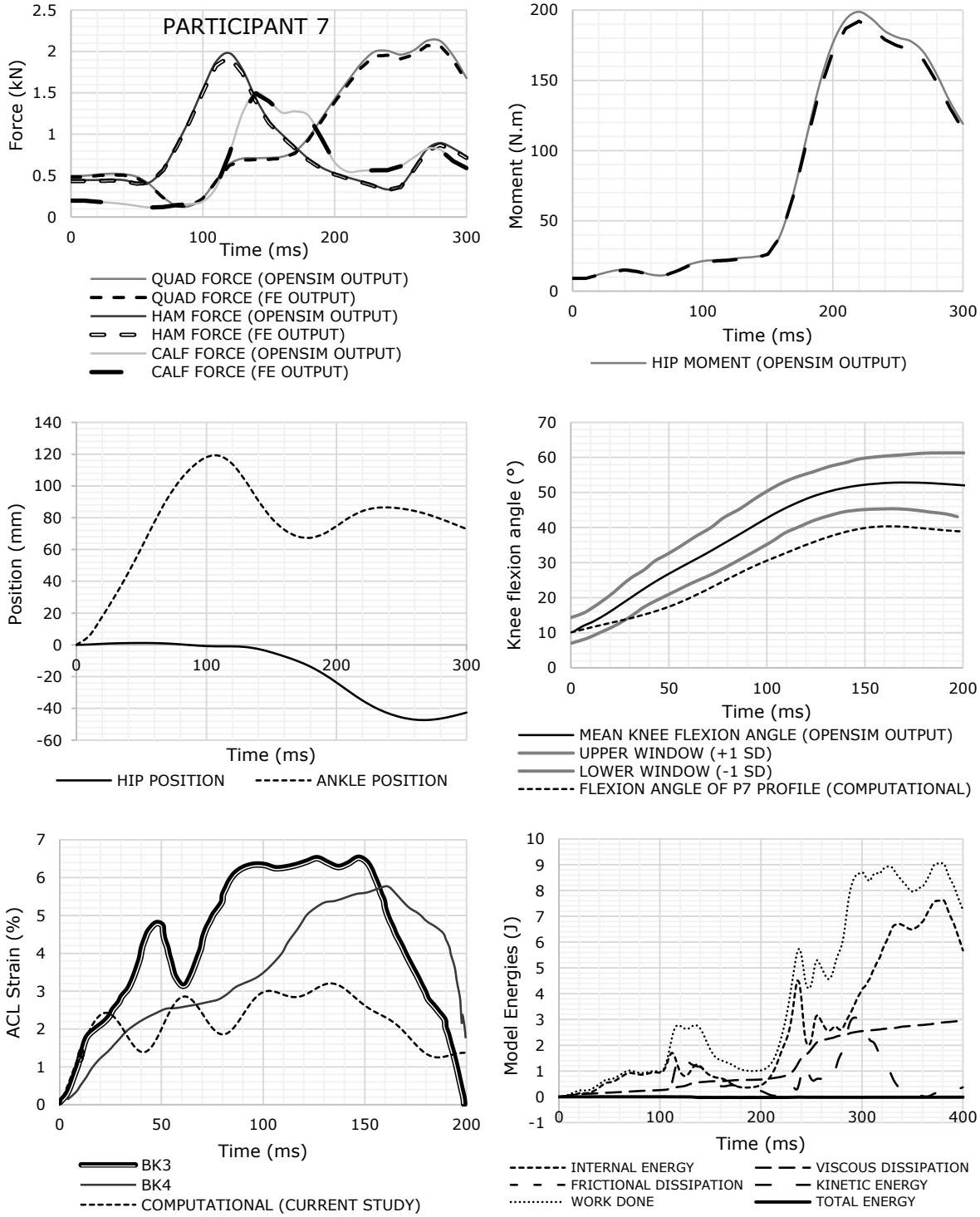

Figure A.6: P7 participant profile results
Kinetic input (top row), Kinematic input (centre, left) for jump landing. Verification of model kinematic output (centre, right), ACL strain results (bottom left) and model energy (bottom right) during the FE simulation

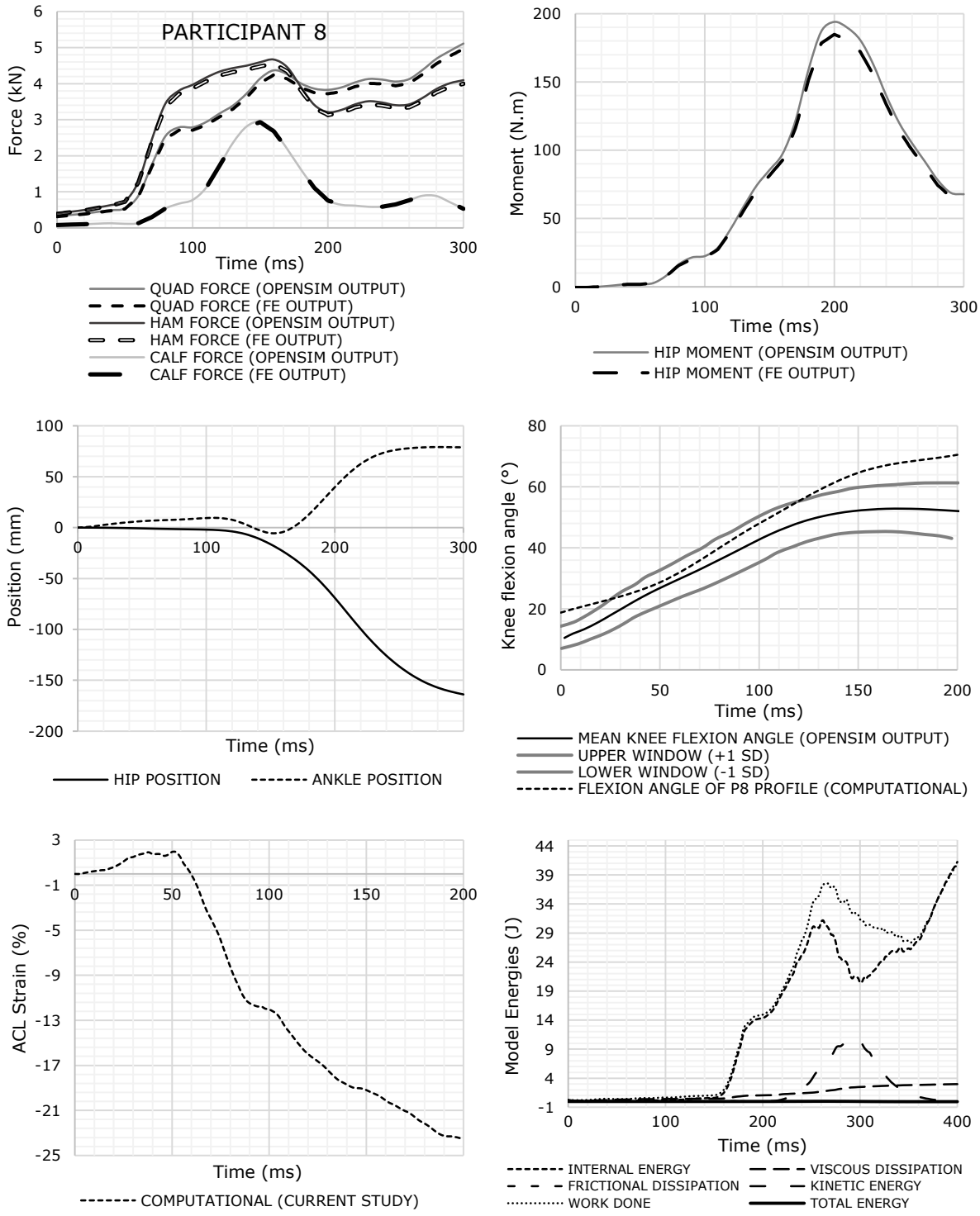

Figure A.7: P8 participant profile results
Kinetic input (top row), Kinematic input (centre, left) for jump landing. Verification of model kinematic output (centre, right), ACL strain results (bottom left) and model energy (bottom right) during the FE simulation

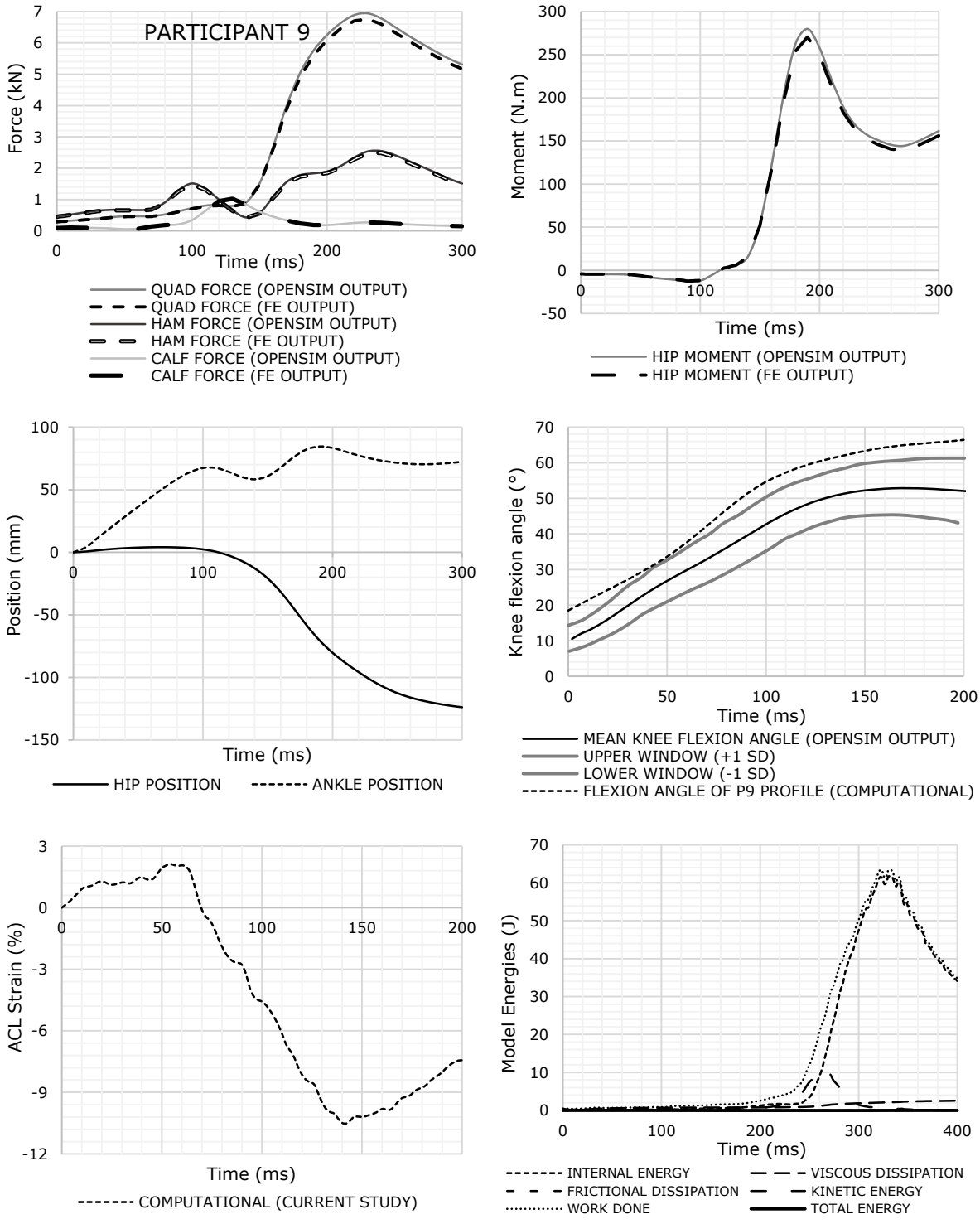

Figure A.8: P9 participant profile results
Kinetic input (top row), Kinematic input (centre, left) for jump landing. Verification of model kinematic output (centre, right), ACL strain results (bottom left) and model energy (bottom right) during the FE simulation

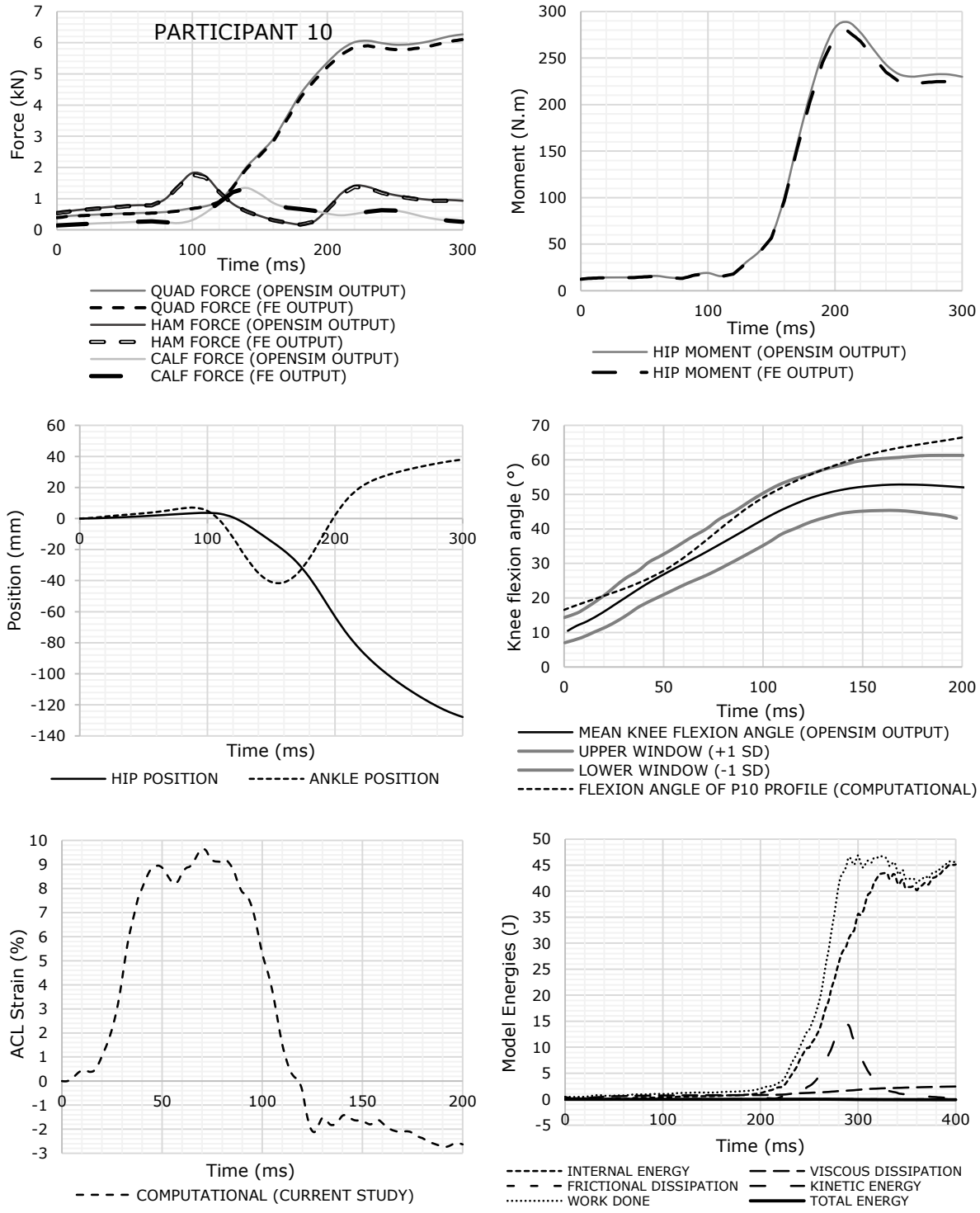

Figure A.9: P10 participant profile results
Kinetic input (top row), Kinematic input (centre, left) for jump landing. Verification of model kinematic output (centre, right), ACL strain results (bottom left) and model energy (bottom right) during the FE simulation